BULLETIN OF THE POLISH ACADEMY OF SCIENCES
TECHNICAL SCIENCES, Vol. 60, No. 3, 2012
DOI: 10.2478/v10175-012-0050-5

Analysis of complex-valued functional magnetic resonance imaging data: are we just going through a "phase"?

V.D. CALHOUN[1,2*] and T. ADALI[3]

[1] The Mind Research Network, Albuquerque, New Mexico 87106, USA
[2] Department of ECE, University of New Mexico, Albuquerque, New Mexico 87131, USA
[3] Department of CSEE, University of Maryland Baltimore County, Baltimore, MD 21250, USA

Abstract. Functional magnetic resonance imaging (fMRI) data are acquired as a natively complex data set, however for various reasons the phase data is typically discarded. Over the past few years, interest in incorporating the phase information into the analyses has been growing and new methods for modeling and processing the data have been developed. In this paper, we provide an overview of approaches to understand the complex nature of fMRI data and to work with the utilizing the full information, both the magnitude and the phase. We discuss the challenges inherent in trying to utilize the phase data, and provide a selective review with emphasis on work in our group for developing biophysical models, preprocessing methods, and statistical analysis of the fully-complex data. Of special emphasis are the use of data-driven approaches, which are particularly useful as they enable us to identify interesting patterns in the complex-valued data without making strong assumptions about how these changes evolve over time, something which is challenging for magnitude data and even more so for the complex data. Finally, we provide our view of the current state of the art in this area and make suggestions for what is needed to make efficient use of the fully-complex fMRI data.

Key words: fMRI, independent component analysis, ICA, phase, complex-valued, brain.

1. Introduction

Functional magnetic resonance imaging (fMRI) is a noninvasive, powerful tool that has been utilized in both research and clinical arenas since the early 1990s [1] and has provided valuable insights to the understanding of the human brain function. FMRI has enabled researchers to directly study the temporal and spatial changes in the brain as a function of various stimuli. Because it relies on the detection of small intensity changes over time, fMRI poses significant challenges for data analysis techniques. FMRI data is natively complex, and thus there is both magnitude and phase information available. To date, most fMRI analysis techniques to date have discarded the phase of the fMRI data. However, the phase information may be quite valuable for the analysis of the natively complex fMRI data. A number of direct benefits have been noted in the use of phase fMRI data as (i). In assessing functional connectivity, phase is more informative than magnitude data [2]; (ii) phase enables better detection of artifacts in both the magnitude and phase data which can then be effectively excluded from further analysis [3, 4]; (iii) the sensitivity and specificity of estimations increase as we have shown with a number of examples as part of our NSF-funded work [5–10]. That is our goal in this paper, to provide a review of various approaches for using the phase information along with the magnitude in fMRI data and to demonstrate the advantages. We first present some preliminaries on the fMRI signal and statistical properties. Next we discuss approaches to understand the underlying biophysics of the phase signal as well as approaches to preprocess and de-noise the data. The remainder of this article is devoted to model-based and data-driven analysis approaches to analyze the complex-valued fMRI data. Traditional model-based analysis approaches – such as linear regression – are robust, yet often too rigid to capture the richness of the human brain activation, in addition their limitation is more evident for incorporating phase into the analyses as still little is known about the nature of fMRI phase data. Independent component analysis (ICA), on the other hand, is a data-driven approach that provides a more flexible framework for the analysis of fMRI data. ICA facilitates the analysis of fMRI data in its complex form by eliminating the need to explicitly model the phase behavior. In addition, ICA is able to separate artifacts from signal more readily as well as capture signal from the phase which may be less predictable that that of the magnitude data. There are also a number of issues that require special consideration in the preprocessing and visualization of the complex fMRI data and we address those issues as well before discussing the two main analysis approaches.

1.1. FMRI data acquisition and the complex nature of FMRI data.

Most fMRI studies involve a neurobehavioral paradigm in which a participant is exposed to sensory stimuli and asked to perform a set of mental and/or motor tasks. A given volume is then collected through slices within a given repetition time, which is usually on the order of a few seconds. The acquired data set includes a brain volume movie with a temporal resolution specified by the time of repetition. The MRI signal is acquired as a quadrature signal using two

*e-mail: vcalhoun@unm.edu

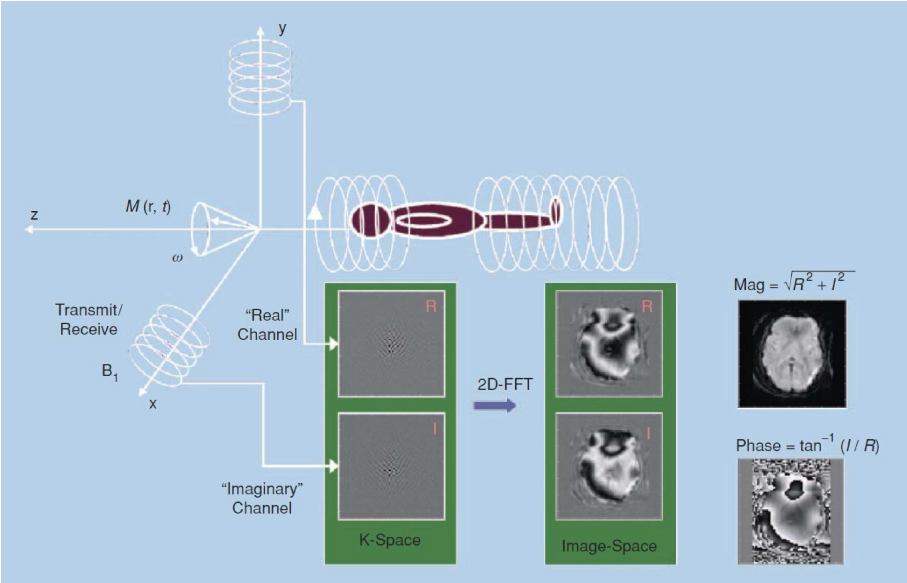

Fig. 1. Diagram of MRI acquisition where M(r, t) represents the magnetization at spatial position r and time t, and ω represents the net phase

or more orthogonal detectors as shown in Fig. 1. The signal that is acquired in the complex frequency space (k-space) is inverse Fourier transformed into the complex image space. This complex-valued fMRI signal change has been shown to contain physiologic in formation [11]. In spite of the presence of useful information in phase, it is usually discarded. Previous studies have reported task-related phase changes [11–14]. Several approaches for modeling the phase have been proposed [15–17]. Processing complex-valued fMRI data using independent component analysis was also proposed in [8]. Previous work has focused on filtering voxels with large phase changes [13, 18–20] based upon models that show that phase changes arise only from large non-randomly-oriented blood vessels. More recent studies from our group and others provide evidence that the randomly oriented microvasculature can also produce a non-zero BOLD-related phase change [20, 21] and we and others have also showed empirical evidence of changes in the phase which correspond to regions expected to be involved in the task [6]. These and much other work providing compelling evidence that the phase information contains useful physiologic information.

2. Preliminaries

Besides medical domain such as magnetic resonance imaging, complex-valued data are an integral part of many science and engineering problems, including those in communications, radar, geophysics, oceanography, electromagnetics, and optics, among others. The complex domain provides both a convenient representation for these signals and a natural way to capture the physical characteristics of these signals. Hence, working completely in the complex domain leads to the most efficient processing of these signals. The complex domain, however, also presents a number of challenges in derivation and analysis of the methods, and as a result, traditionally, the vast majority of algorithms developed for their processing have taken "engineering" shortcuts, thus failing to fully exploit the potential of complex-domain processing. The most common one among those shortcuts has been assuming the circularity of the signal, an assumption that discards the information conveyed by the relationship of real and imaginary parts of the signal, or equivalently by the phase, which is, one of the main reasons one would want to work in the complex domain, $i.e.$, take into account such information in a compact and effective way while using the power of complex calculus.

There have been important advances in this area within the last decade that clearly demonstrate that noncircularity is an intrinsic characteristic of many signals of practical interest, and when taken into account, the methods developed for their processing may provide significant performance gains [22–26]. The two key fundamental advances in this context have first been the development of methods that allow the use of complete statistical information without assuming circularity. What has greatly helped in this development is the development of a complete framework for optimization [22, 27] that is based on Wirtinger calculus [28].

2.1. Statistics. In almost all methods developed prior to 2000 for the complex domain, the circularity assumption has been invoked either explicitly, or implicitly, by simply using only partial statistical information in the development. For example when using second-order statistics, only the correlation information, $E\{\boldsymbol{x}\boldsymbol{x}^H\}$, is used ignoring the pseudo (complementary) correlation given by $E\{\boldsymbol{x}\boldsymbol{x}^T\}$, written for a random vector $\boldsymbol{x}$. A second-order circular (or improper) random vector is one for which $E\{\boldsymbol{x}\boldsymbol{x}^T\} = \mathbf{0}$. When taking full statistical information into account, circularity is defined in terms of the probability density function (pdf) such that a random variable x is circular if x and $xe^{j\theta}$ have the same pdf, $i.e.$, the

pdf is rotation invariant [29]. In this case, the phase is non-informative and the pdf is a function of only the magnitude, $p(x) = g(|x|)$ where $g : R \mapsto R$. Data in many applications such as biomedical data analysis, array processing, and communications are however noncircular in nature, see e.g., [22, 26, 30, 31], hence taking their potential noncircularity into account is important for achieving the best performance.

In Fig. 2(a), we show the scatter plot of a motor component estimated using ICA of functional MRI data [3]. The paradigm used in the collection of the data is a simple motor task with a box-car type time-course, $i.e.$, the stimulus has periodic on and off periods. As can be observed in the figure, the distribution of the given fMRI motor component has a highly noncircular distribution. In Fig. 2(b) and (c), we show the spatial map for the same component using a Mahalanobis Z-score threshold, which we define in Section 0. This distribution is typical as most often the signal power is optimized to be mainly in one channel [32, 33] but as we noted, the signal component of the BOLD measurement appears in both the real and imaginary channels resulting in complex-valued fMRI data.

Hence, in the processing and analysis of fMRI data in its native complex form, it is important to account for noncircularity of the distribution. Wirtinger calculus, which we explain next allows derivation of algorithms that can fully take this property into account by making optimization much easier so that the common simplifying assumptions of circularity does not need to be invoked.

2.2. Optimization. The most important step in the derivation of algorithms, one has to compute gradient and Hessians of cost functions, such as a quadratic form or a likelihood function. Since cost functions are real valued, i.e., are scalar quantities in the complex vector space, they are not analytic, and hence not differentiable in a given open set. To overcome this basic limitation, a number of approaches have been traditionally adopted in the signal processing literature the most common of which is the evaluation of separate derivatives with respect to the real and complex parts of a given function.

The framework based on Wirtinger calculus [22, 28] – also called the CR calculus [27] – provides a simple and straightforward approach to performing derivatives in the complex plane, in particular for the important case we mention above, for non-analytic functions. More importantly, it allows one to perform all the derivations and the analyses in the complex domain without having to consider the real and imaginary parts separately. Hence, all computations can be carried out in a manner very similar to the real-valued case, and hence the derivations that use Wirtinger calculus can be directly adapted to the real case.

The main idea behind Wirtinger calculus is based on the definition of a more relaxed condition of differentiability for the complex domain as opposed to the classical definition whose main objective is to make sure that the derivative calculations parallel those in the real domain. Wirtinger calculus [28] relaxes the traditional definition of differentiability and only requires that $f(z)$ be differentiable when expressed as a function $f : R^2 \to R^2$. Such a function is called *real-differentiable*. Hence, if $u(z_r, z_i)$ and $v(z_r, z_i)$ have continuous partial derivatives with respect z_r to and z_i, f is real-differentiable. For such a function, we can write

$$\frac{\partial f}{\partial z} = \frac{1}{2}\left(\frac{\partial f}{\partial z_r} - j\frac{\partial f}{\partial z_i}\right) \quad \text{and} \quad \frac{\partial f}{\partial z^*} = \frac{1}{2}\left(\frac{\partial f}{\partial z_r} + j\frac{\partial f}{\partial z_i}\right) \tag{1}$$

which can be formally implemented by regarding f as a bivariate function $f(z, z^*)$ and treating z and z^* as *independent variables*. That is, when applying $\partial f/\partial z$, we take the derivative with respect to z, while formally treating z^* as a constant. Similarly, $\partial f/\partial z^*$ yields the derivative with respect to z^*, formally regarding z as a constant. Thus, there is no need to develop new differentiation rules. This was shown in [34] in 1983 without a specific reference to Wirtinger's earlier work [28]. If f is analytic, then the usual complex derivative $\partial f/\partial z$ and in (2) coincide. Hence, Wirtinger calculus contains standard complex calculus as a special case.

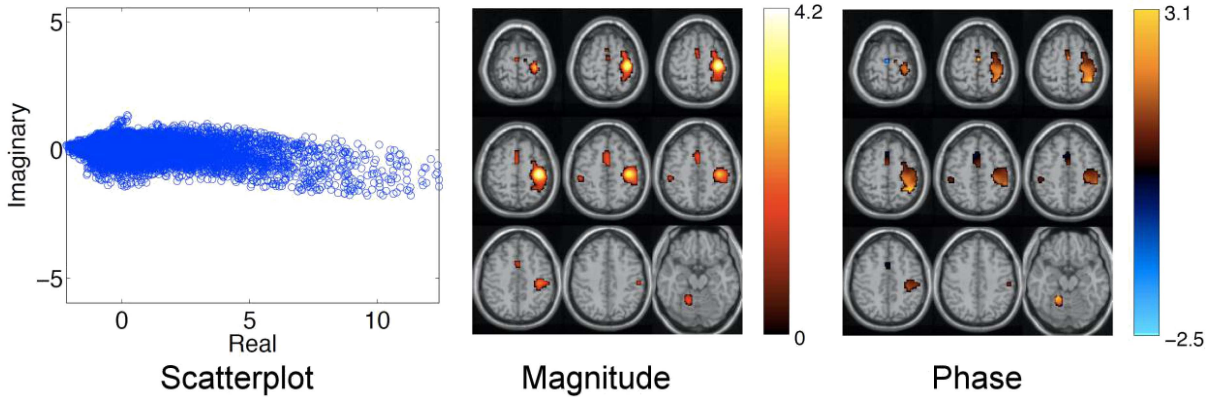

Fig. 2. a) Scatter plot of the average voxel values of the motor component estimated using ICA from 16 subjects. (b) Magnitude and (c) phase spatial maps using Mahalanobis Z-score thresholding; only voxels with are shown

The same approach, i.e., treating the variable and its complex conjugate as independent variables, can be used when taking derivatives of functions of matrix variables as well so that expressions given for real-valued matrix derivatives can be directly used. A good reference for real-valued matrix derivatives is [35] and a number of complex-valued matrix derivatives are discussed in detail in [11]. In [22, 27, 36], the complete framework for vector and matrix optimization using Wirtinger calculus is presented by using the gradient and Hessian relationships given in [37] but by keeping the whole development in the complex plane and in the original problem dimension C^N rather than doubling the dimension as in [37].

Hence, using Wirtinger calculus, all calculations can be carried out in a manner similar to real-valued calculus while keeping all the computations in the complex domain. It is also shown that the simplifying and unrealistic assumption of noncircularity can be avoided in both the algorithm development and in the analyses of the algorithms when one uses Wirtinger calculus, see e.g., [5, 36, 38–44].

3. Biophysical models

One powerful approach for understanding the underlying fMRI signal is to use biophysical modeling. To highlight the scope of what is possible, we present two models for calculating the complex BOLD signal. The first is a microscopic model that calculates the BOLD signal based on the detailed geometry of the micro-vessels, spatial distribution of susceptibility, and diffusion. The second is a macroscopic model that is defined at a resolution of the fMRI experiment and can be used in the inverse problem of combining magnitude/phase BOLD data to improve activation localization and detection.

3.1. Microscopic model. The microscopic model, we present now, follows the description presented in works [45–47]. A two-compartment model, consisting of the extravascular and the intravascular contribution to the BOLD signal is typically considered. Briefly it consists of a) defining a spatial susceptibility distribution $\chi(r) = \chi_m(r)V(r)$, as a product of the assumed network geometry $V(r)$ and the macroscopically varying susceptibility $\chi_m(r)$, b) calculating the magnetic field distribution $B_z(r)$ from $\chi(r)$ using a 3D fast Fourier transform (3DFFT) method, and c) calculating the BOLD signal from $B_z(r)$ by appropriate averaging over the voxel and taking into account diffusion. $B_z(k) = B_0(1/3 - k_z^2/k^2)\chi(k)$ is the 3DFFT of the magnetic field.

Figure 3a shows the geometry which consists of a random distribution of microvessels (infinite cylinders) with a radius = 2.5 um with blood volume fraction = 0.04. Figure 3b is a slice from the corresponding $\Delta B_0(r)$ calculated from the algorithm proposed in [48]) for a Hct = 0.4, Y = 0.5, $\Delta\chi_{do} = 0.27$ ppm $x4\pi$ (units in milliTesla). Assuming a diffusion coefficient $= 1 \times 10^{-9}$ m^2/s we compute the signal attenuation profile shown in Fig. 3c.

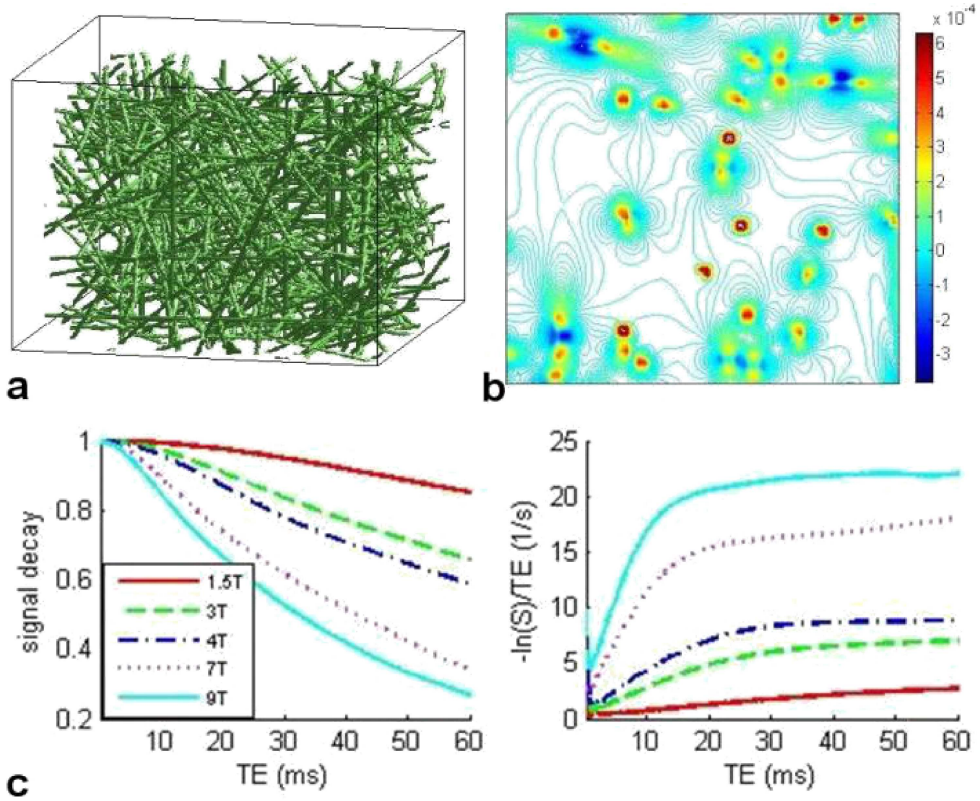

Fig. 3. Example simulation including diffusion: (a) geometry, (b) slice through simulation showing field changes, (c/d) signal decay at different field strengths

3.2. Macroscopic model. We can also use a macroscopic model which summarizes the results of the microscopic model at the level of fMRI voxel resolution. It reflects the experimentally observed patterns of magnitude and phase BOLD signals. We follow the methods developed by Yablonskiy and Haacke [49] and Marques and Bowtell [46], and a model for predicting phase change previously discussed by us [21].

Macroscopic models can be defined for a) random distribution of microvessels (capillaries), b) Oriented distribution of larger vessels (venules), and c) a single large vessel. As discussed before, the extravascular and the intravascular signal can be considered as separate compartments. Although both magnitude and phase effects depend on the underlying vascular geometry and the susceptibility change, they primarily depend on different magnetic field characteristics. To first order, the magnitude attenuation depends on the intra-voxel magnetic field inhomogeneity and the phase depends on the mean magnetic field at the voxel. The magnitude and phase changes have different models as described below.

Extravascular signal. $S_E = S_0 e^{-R^*_{2,E} T_E} e^{-i\phi}$, where $R^*_{2,E} = R_{2,GM} + aV^b \chi^c_m$. V is the voxel volume and $\chi_m(r)$ is the macroscopic susceptibility distribution. The parameters a, b, c are parameters obtained from numerical simulations with the microscopic model for different vessel dimensions, blood volume fraction, and vessel radius. The simulation work of Marques and Bowtell [46] has shown that a realistic model and the infinite cylinder model give similar values for a, b, c. The values for the realistic model were $a = 2.73$, $b = 1.13$, and $c = 1.29$. The phase $\phi = \gamma B_m T_E$ is calculated from macroscopic magnetic field B_m, where B_m is calculated from the macroscopic susceptibility distribution $\chi_m(r)$ by the 3DFFT method described earlier. This method was described earlier in Feng [21] and Fig. 4 shows an example.

Intravascular signal (case 1). Randomly distributed cylinders with blood volume fraction $= f_1$. $S_I = S_1 I(t) e^{-R^*_{2,I} T_E}$, where $R^*_{2,I} = a_1 V^{b_1} {\chi_m}^{c_1} + a_2 V^{b_2} {\chi_m}^{c_2}$, $I(t) = (1/2) \int_0^\pi \sin\theta e^{ik(2\cos^2\theta - 1)t} d\theta$, and $k = (2/3)\pi\gamma B_)\chi$. Marques and Bowtell [46] estimate $a_1 = 3.5$, $b_1 = 1.0$, $c_1 = 1.2$, $a_2 = 40.0$, $b_2 = -0.4$, and $c_2 = 1.2$.

Intravascular signal (case 2). A single cylinder with blood volume fraction $= f_2$. The field inside the cylinder is orientation dependent but is spatially constant. $S_L = S_0 e^{-R_{2,B} T_E} e^{-i\phi_L}$, where $\phi_L = \gamma B_0 (\chi/6)(3\cos^2\theta - 1) T_E$. The total signal is given by $S_T = (1 - f_1 - f_2) S_E + f_1 S_I + f_2 S_L$. The magnitude signal in each compartment has the form $S = S_0 e^{-R^*_2 T_E}$, and for small changes in R^*_2, $\Delta S/S = -T_E \Delta R^*_2$. ΔR^*_2 can be related to changes in χ_m by models presented earlier. The magnitude of the blood/tissue susceptibility difference is modeled by $\chi = Hct(1-Y)\chi_{dHb}$, where $Hct = 0.4$, $\chi_{dHb} = 2.2$ ppm (MKS units). This gives $\chi = 0.36$ ppm in the resting state with an oxygenation fraction $Y = 0.6$ and $\chi = 0.18$ ppm in the active state with $Y = 0.8$. These numbers imply that the change in χ between the resting state and the activated state is estimated to be $\Delta\chi = 0.18$ ppm.

3.3. Intravascular effect. Here we estimate the maximum phase change expected in a single large vessel to the phase change calculated in a capillary bed under some reasonable parameter assumptions. If the cylinder is parallel to the main field $\phi_L = \gamma B_0 \chi T_E/3 = 15.4\pi T_E$, for $B_0 = 3T$ and $\chi = 0.18$ ppm. The phase in the total signal will depend of the blood volume fraction f, but as can be seen it can become as large as π. Menon et al. have suggested that large phase changes can be used to detect and exclude large vessel artifacts [13]. When an analysis is done in combination with a physical model we can use the phase information to either enhance an activated region or suppress a false activation.

3.4. Phase changes also occur in parenchymal regions containing only small vessels. We assume that the macroscopic susceptibility change is 3D Gaussian.

$$\Delta\chi_m(r) = C_k \exp\left(-\frac{1}{2}\left[\frac{x^2}{\sigma_x^2} + \frac{y^2}{\sigma_y^2} + \frac{z^2}{\sigma_z^2}\right]\right), \qquad (2)$$

where C_k is a scaling constant. We choose the value of C_k based on parameter values from the literature. We define $\Delta\chi'$ as the susceptibility difference between completely deoxygenated and completely oxygenated red blood cells ($0.264 \times 4\pi$ ppm in MKS units [50] with a hematocrit level of 0.4 [51], and oxygenation level Y is the fractional oxygenation in the red cells with $\Delta Y_{cap} = 0.08$ [11, 12]. Then for a blood volume fraction f of 0.05 and ignoring the cerebral blood volume change, $C_k = -f \cdot \Delta Y_{cap} \cdot 4\pi \cdot \Delta\chi' \cdot Hct$, C_k is approximately $-5.3e^{-9}$.

Figure 4 shows the simulation results of magnetic field/phase change corresponding to 3D Gaussian volume-averaged susceptibility/magnetization change for the cases of $\sigma_x : \sigma_y : \sigma_z = 1 : 1 : 1$, 1:1:2, 2:2:1 and 2:2:1, Eq. (1), rotated counter-clockwise around the x-axis by $\pi/3$, respectively. For the value of C_k selected above, the resulting maximum simulated phase change for all of these configurations is in the order of 1°. Depending on the spatial distribution of the susceptibility changes and the angle of the cut plane of the magnetic field change, the resulting phase shows patterns of dominantly positive, dominantly negative, or combinations of positive and negative phase changes due to the volume-averaged magnetization and demagnetization effects.

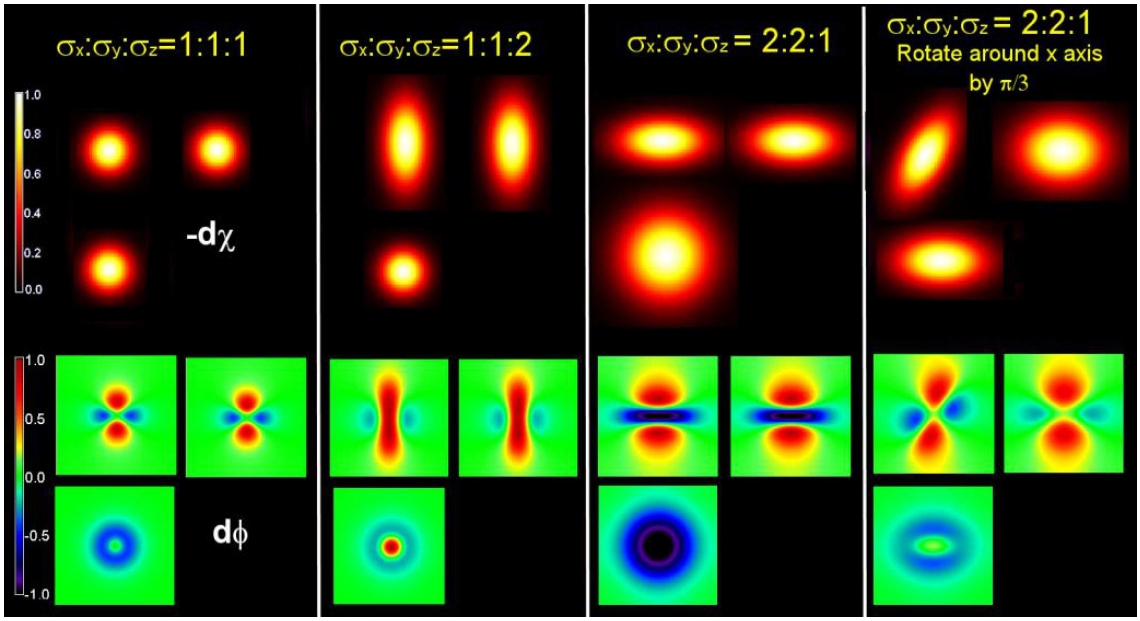

Fig. 4. Simulation of phase change corresponding to 3D Gaussian volume-averaged susceptibility change for the cases of $\sigma x : \sigma y : \sigma z = 1 : 1 : 1$, 1:1:2, 2:2:1 and 2:2:1 rotated counter-clockwise around the x-axis by $\pi/3$

3.5. Robustness to noise by using phase. A second simulated example is shown on how to fit the magnitude signal change or determine how much to smooth. The problem can be approached by finding an optimal smoothing of the magnitude response constrained by phase. The optimization cannot be performed without the phase information. Given a magnitude change we can calculate a signal proportional to phase change. Let $f_m(r)$ and $f_\phi(r)$ be the magnitude and phase change images. The error functions for magnitude and phase are written as $E1 = ||\chi(r) - f_m(r)||^2$, and $E2 = S^2||\alpha F(\chi(r) - f_\phi(r)||^2$. We now seek a function $\chi(r)$ and α, such that $E1$is approximately equal to $E2$ while $E1 + E2$ is a minimum. The additional phase information enables us to find a smooth solution for $\chi(r)$. The results of the proposed fitting are shown in Fig. 5 where we transform a noisy image magnitude/phase image pair (middle) to a pair which has error relative to the ground truth (left) reduced by a factor of 20 (right). The joint constraint allows us to determine the optimal smoothing and fit the magnitude data without ground truth knowledge.

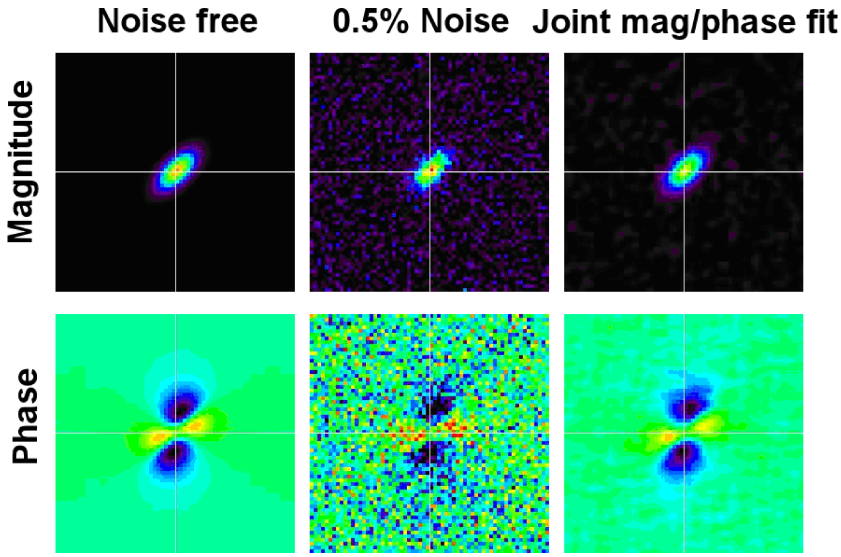

Fig. 5. Joint magnitude/phase fit to reduce noise

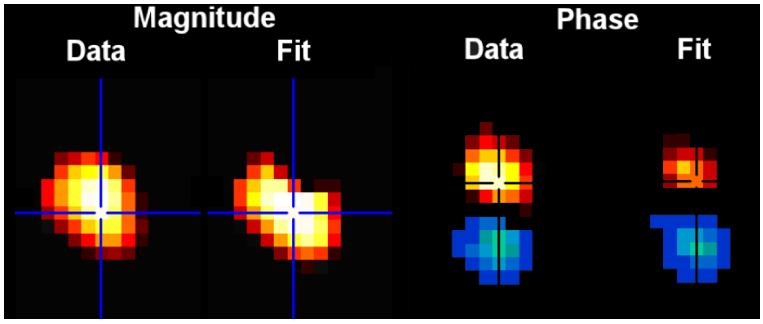

Fig. 6. Simultaneous fit for one subject

3.6. Fitting the model to real fMRI data. The macroscopic model suggests that both magnitude and phase of the BOLD signal depend on the macroscopic susceptibility distribution $\chi_m(r)$. The magnitude change depends $\chi_m(r)$ on through models for R_2^* and the phase through the 3DFFT model or the separate case of large vessels. We propose to estimate $\chi_m(r)$ by minimizing the goodness-of-fit function χ^2 used for fitting the magnitude and phase change models as defined by:

$$\chi^2 = \int_r \left(\left(\frac{\Delta S(r)}{S(r)} - \frac{\Delta \widehat{S}(r)}{\widehat{S}(r)} \right) / \sigma_{ds}(r) \right)^2 dr + \int_r \left(\frac{\Delta\phi(r) - \Delta\widehat{\phi}(r)}{\sigma_{d\phi}(r)} \right)^2 dr,$$

where $\Delta\widehat{S}(r)/\widehat{S}(r)$, $\Delta\widehat{\phi}(r)$ are theoretical scaled magnitude change and phase change, respectively, and $\Delta S(r)/S(r)$, $\Delta\phi(r)$ are the observed magnitude change data and phase change data; $\sigma_{ds}(r)$ and $\sigma_{d\phi}(r)$ are the standard deviation of magnitude and phase change at each voxel. The integration is over the volume of activation (VOA). Figure 6 shows the simultaneous fitting results for one subject showing data as well as the fits for magnitude and phase.

Experiments were performed on a 3T Siemens TRIO TIM system using a standard Siemens gradient-echo EPI sequence. We used a Field-of-View (FOV) = 240 mm, Slice thickness = 3.5 mm, Slice Gap = 1 mm, 32 slices, Matrix size = 64×64, TE = 29 ms, and TR = 2 s. The fMRI experiment used a block design with alternating 30s finger tapping. The total experiment time was 5.5 minutes.

Data were preprocessed using the SPM software (http://www.fil.ion.ucl.ac.uk/spm/software/spm/5/). Complex images were corrected by dividing each time point by the first time point, and then recalculating the phase images. Further phase unwrapping was not required. Data were motion corrected [51], spatially smoothed with a 10 mm^3 full width at half-maximum Gaussian kernel, and spatially normalized into the Montreal Neurological Institute space. Activation maps were computed using the multiple regression framework within SPM5 in which regressors are created from the stimulus onset times and convolved with a standard hemodynamic response function. A contrast was created for each individual subject for finger tapping versus rest. A group analysis was performed using the activation maps from each individual subjects and entering them into voxelwise one-sample t-tests.

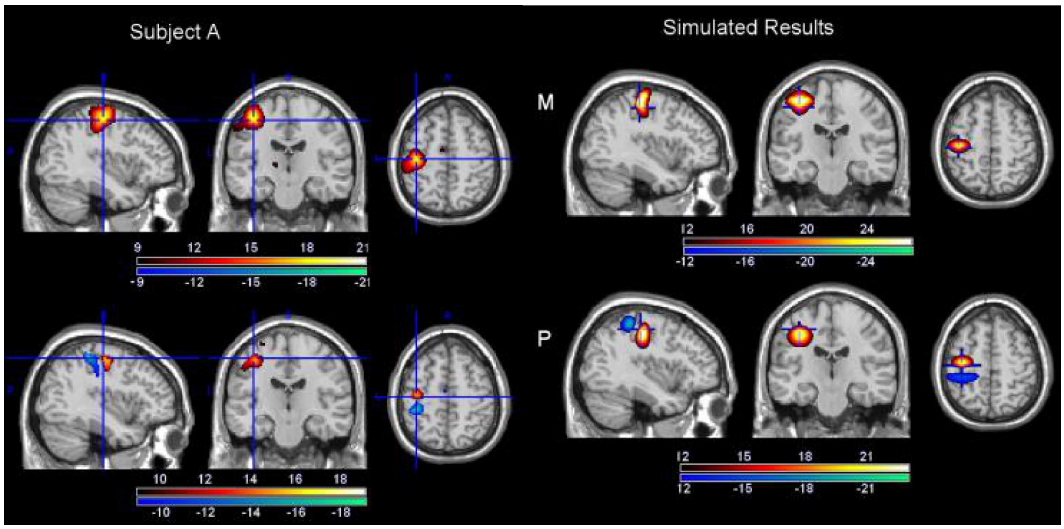

Fig. 7. Magnitude (M) and phase (P) changes (t-values) for representative subject (left) and simulated results (right). The color bars for the subjects show the t-value ranges. The colorbar for the simulated results indicate the relative strength of susceptibility and phase change

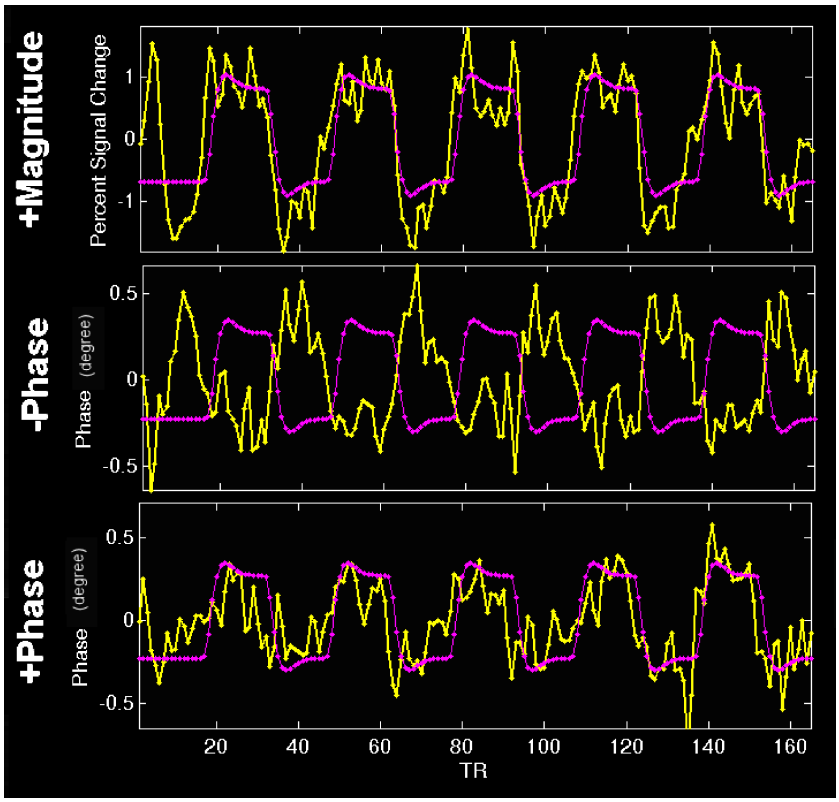

Fig. 8. Phase and magnitude change time courses

In Fig. 7, the left panel show the magnitude and phase change of the results (thresholded at $t = 8$ ($p < 1 \times 10^{-13}$)) for subject A (for a complete reporting of results see [21]. The panel on the right shows the susceptibility change and phase change of simulated results. Here, we assume the magnitude change is approximately linear to the volume-averaged susceptibility change. The highest magnitude change was observed in the motor cortex. Further observation of Fig. 7 indicates the peak of the magnitude change is not located where the phase change peaks; instead, it is closer to the sign change of the phase change (the minimum absolute phase value). The simulations to match the observed fMRI phase/magnitude changes began by approximating the observed phase change pattern to that obtained by Gaussian distributions, and calculating the susceptibility distribution by an inverse calculation [53]. Then a matched phase distribution was calculated by a forward model calculation. The results show that our model can closely match patterns observed experimentally.

Figure 8 shows the phase and magnitude change time courses from a single voxel (the one showing maximal phase change) for a representative subject. The time evolutions of the phase and magnitude change are similar to each other, suggesting that both changes originate from the same source, the deoxyhemoglobin-induced susceptibility change. The measured voxel phase change (unsmoothed) is around 1°, on the same order of the simulation results as shown in Fig. 4. They are both on the same order of a measured voxel phase change (no large vessel present) 0.028 radians or 1.6° in [13].

4. Preprocessing and visualization

4.1. Motion correction. Existing methods for motion correction and spatial normalization can be modified to work for an analysis including the phase. A straightforward approach is to simply use the magnitude image to compute the parameters for both motion correction and for spatial normalization and then to apply the computed transformation to the phase images. This appears to work quite well although a potential down side is it does not consider the possibility that the phase data may contain useful information about movement or structure in general. As a simple extension one can try to incorporate a cost function which uses both the magnitude and the phase. A typical least-squares cost function for motion correction is given below, $\text{CF} = \sum_{i=2:N}[M_i - M_1]^2$ where M_i is the i-th time point image. It is possible to implement a complex motion correction approach by realigning the images using the information present in the complex image (obtained by combining the magnitude and phase data). A proposed cost function for the complex algorithm is given below,

$$\text{Cost} = \sum_{(} i = 2 : N) \left[\frac{(R_i - R_1)^2}{1/(\text{Norm}(R_1))} + \frac{(I_i - I_1)^2}{1/(\text{Norm}(I_1))} \right],$$

where is the real part of the time point and is the imaginary part of the time point. We applied this approach to fMRI data from several subjects performing a motor tapping task. The results using the magnitude only cost function and the complex-valued cost function are similar but not identical. The resulting T-maps for both magnitude and phase show less activity at the

edges of the brain (40% smaller T-values on average) when performing motion correction using the complex-valued data suggesting that the complex motion correction algorithm does a better job in handling the motion. Overall the patterns observed pre and post motion correction are highly similar with pre/post motion corrected maps spatially correlated at 0.97 for phase and 0.98 for magnitude. The significance is slightly higher for the unified approach compared to an approach in which we used only the magnitude data and applied the parameter estimates to the phase data. The phase for the unified approach shows increases from T = 18.8 to T = 18.9 and magnitude changed from T = 21.3 to T = 21.4. The T-value improvements are encouraging, but relatively modest.

4.2. Spatial normalization. Just as in motion correction we can use two approaches, one using the magnitude information and pulling the phase information along, and the other using both magnitude and phase to computed the normalization parameters. For the latter the images can be spatially normalized to the Montreal Neurological Institute (MNI) template and we use the cost function in [2] to derive the nonlinear parameter estimates. A study specific template (including both real and imaginary images) was created using an initial registration based upon the magnitude data and then applying the parameters to the real and imaginary data and averaging across subjects to create a template that has real and imaginary images. The data can then be renormalized to this group template using the cost function in [2] to provide a more accurate estimate. We tested this approach on a group of 17 subjects. We converted the data to magnitude and phase and a statistical analysis was performed on the magnitude and phase data independently. Results were overall quite similar to the magnitude-only approach, but again the T-maps were slightly higher for the unified approach. Results are thus encouraging, but more work is needed.

4.3. Preprocessing and visualization.

Spatial smoothing. Data are typically spatially smoothed with e.g., a Gaussian kernel to improve the contrast-to-noise ratio [6, 8]. Smoothing is useful for group data as it both reduces the amount of high-frequency spatial noise as well as desensitizes the images to variability of functional activation and anatomy among subjects. We analyze both unsmoothed and smoothed data with different kernels to evaluate the impact of smoothing upon the analysis. There is likely room for improvement in smoothing schemes to move beyond Gaussian, e.g. wavelet smoothing [54]. In the complex-domain there is also the possibility of performing natively complex smoothing, for example one could use a modified complex anisotropic diffusion filtering [55]. However, this is an application area which has not yet been fully evaluated.

Phase denoising. A physiologically motivated denoising method is given in [4] and uses the phase to identify noisy voxels and eliminates them or introduces a weighting scheme depending on their noise level. The quality map phase denoising (QMPD) uses gradient information to determine the noisy voxels and eliminates them from further analysis [4]. It is shown that the voxels identified as noisy are in areas that are known to suffer from susceptibility artifacts, such as the area from the orbitofrontal cortex due to air in the sinuses. The final component of this method includes an important smoothing step that if done before eliminating noisy voxels can spread their detrimental effects to their surroundings. It is also noted that the ICA results obtained with the QMPD method provides higher Z-scores (11.87 versus 10.83) and a larger number of active voxels (1589 versus 1238) as compared to those obtained with the MTEE method [4].

Phase correction for ICA group studies. We note the importance of phase correction for the analysis results for groups of subjects as a simple rotation of the estimated distribution of the activation map can have serious detrimental effects in the group results when we compute averages. There have been two approaches proposed to address this problem. If information on the distribution of the original fMRI data is available, then this prior information can be used for selecting the appropriate nonlinearity in the ICA algorithm as shown in Fig. 9 (right) [38, 40, 43]. As shown in [38], a number of trigonometric functions and their hyperbolic counterparts can be effectively used for achieving ICA, and for the fMRI data we use where the signal is maximized in the real part, the function shown in Fig. 9 (right) provides a perfect match and eliminates the phase rotation in the estimated components as we show in [56].

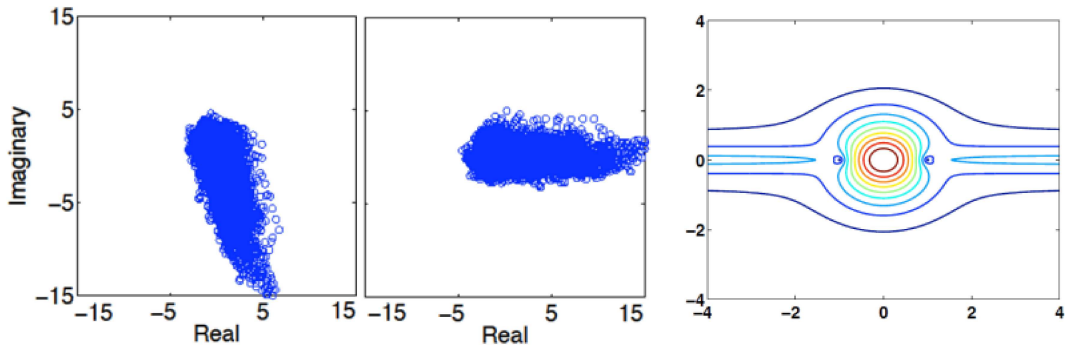

Fig. 9. Complex scatter plot of an estimated motor task related source before (left) and after (middle) applying the PCA-based phase correction scheme. (right) form of pdf implied by the score function

A second approach uses direct manipulation of the data to correct for phase rotation in the estimated fMRI components: 1) Find rotation angle θ that maximizes: $\text{argmaz}_\theta E[(\mathbf{M}\widehat{\mathbf{s}})^2]$, 2) Resolve 180° phase ambiguity: $\text{argmax}_\theta E[(\mathbf{M}\widehat{\mathbf{s}})^3]$ where and $\mathbf{M} = [\cos\theta \ \sin\theta; \ -\in\theta \ \cos\theta]$ and $\widehat{\mathbf{s}}_k = [\widehat{s}_{k.re}, \widehat{s}_{k,im}]^T$. Figure 9 shows the scatter plot of the real and imaginary data of an estimated source before and after the PCA based phase correction. In Fig. 13, we show group ICA results for 20 subjects performing a motor tapping task.

5. Model-based analysis of complex fMRI data

5.1. fMRI data analysis. We now discuss statistical analysis using a model-based approach. Typically, the acquired fMRI data are first preprocessed, for example by the 1) correction of slices for the slight time shift within each volume, 2) registration to correct for subject motion during the scan, and 3) spatial normalization to enable comparisons among subjects and neuro-anatomical labeling, and 4) smoothing. Following the preprocessing step, the data are analyzed to determine the voxels with significant temporal signal change, which are then super-thresholded and overlaid on an anatomical image. The volume data is then organized into a matrix X such that each row is formed by concatenation of the slices at a given time instant resulting in the $T \times V$ matrix shown in Fig. 10.

5.2. General linear model. The most widely used method for the analysis of fMRI data is linear regression using the general linear model (GLM) [83]. As shown in Fig. 10 along with an example time course (regressor) for a simple on-off paradigm, X is the matrix of input data, R is a design matrix, and M is the matrix of activation maps. The time course is correlated with the fMRI data to determine the voxels that show activity related to the chosen time course. The goal is find the matrix M, i.e., compute the regression coefficients (entries of matrix M) that are deemed to be active. An important limitation of this method is that the regressors rk that form the matrix R need to be specified a priori.

Several methods for approaching the analysis of the phase information within the GLM framework were proposed by Rowe et al. [14–17, 57]. The general complex fMRI model proposed by Rowe is given in [15]:

$$
\begin{aligned}
y_t &= (\rho_t \cos\theta_t + \eta_{Rt}) + i(\rho_t \sin\theta_t + \eta_{It}),\\
\rho_t &= x_t'\beta = \beta_0 + \beta_1 x_{1t} + \cdots + \beta_{q1} x_{q1t},\\
\theta_t &= u'\gamma = \gamma_0 + \gamma_1 u_{1t} + \cdots + \gamma_{q2t} u_{q2t},\\
t &= 1, \ldots, n
\end{aligned}
$$

where $(\eta_{Rt}, \eta_{It})' \sim N(0, \sigma^2 I)$, x_t' is the t-th row of an $n \times (q_1 + 1)$ design matrix X for the magnitude, u_t' is the t-th row of an $n \times (q_1 + 1)$ design matrix U for the phase, while β and γ are the regression coefficients for the magnitude and phase.

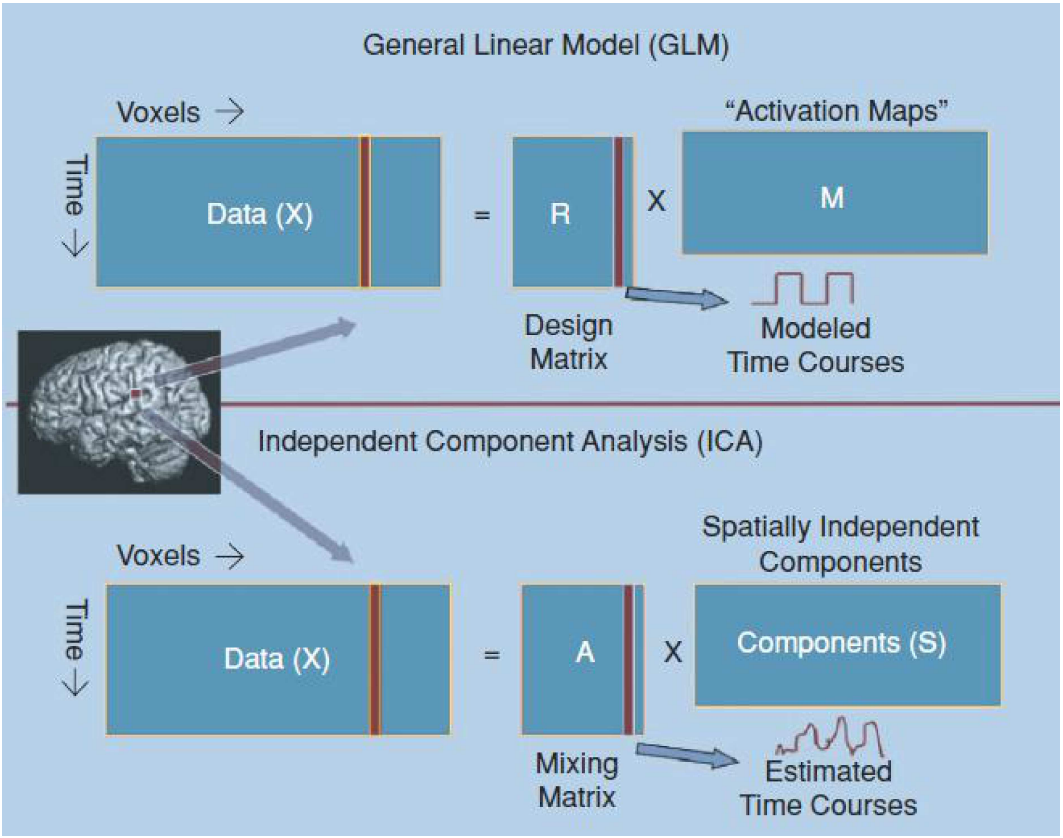

Fig. 10. Application of GLM and ICA to fMRI data

Rowe considers a number of cases for modeling the phase, in [15] and [14], a task-related phase is considered, in [17] the phase is modeled as an arbitrary value (and under this model, i.e., uninformative phase, the model is shown to be equivalent to magnitude only case), and finally in [16], a constant value (identical at all time-points) has been used for modeling the phase. With the given linear model, the hypotheses regarding task related magnitude and phase changes can be evaluated on an individual complex-valued voxel-wise basis, using maximum likelihood estimators.

5.3. GLM group analysis. Few studies have examined phase data in a larger group of subjects for multiple types of fMRI tasks, nor have studies examined phase changes due to event-related stimuli. In recent work from our group, we evaluate the correspondence between the magnitude and phase changes at a group level in a block-design motor tapping task and in an event-related auditory oddball task [6]. The results for both block-design and event-related tasks indicate the presence of task related information in the phase data with phase-only and magnitude-only approaches showing signal changes in the expected brain regions. Although there is more overall activity detected with magnitude data, the phase-only analysis also reveals activity in regions expected to be involved in the task, some of which were not significantly activated in the magnitude-only analysis, suggesting that the phase might provide some unique information. In addition, the phase can potentially increase sensitivity within regions also showing magnitude changes. The identification of regions which 1) show signal changes for magnitude data only, 2) show signal changes for phase data only, or 3) show signal changes for both magnitude and phase data were of particular interest.

Figure 11 shows the magnitude change and phase change of the results for motor tapping and auditory oddball. As expected the highest magnitude change for motor tapping was observed in the left motor cortex and for the auditory oddball highest change was in bilateral temporal lobe. Similarly, maximal phase changes were also observed in motor cortex for MT and in temporal lobe for AOD. The images in the top-right and bottom-right panels of Fig. 1 are the RGB (R-red, G-greed, B-blue) color maps for MT and AOD similar to the display provided in [15]. The areas in red are where only significant magnitude signal changes were observed, the ones in green are for significant phase-only signal changes and the areas in blue are where both significant magnitude and significant phase signal changes were observed. The resulting signal change changes for phase and magnitude data for both motor tapping and AOD were cluster thresholded to correct for multiple comparisons at family wise error (FWE).

The color activation maps in Fig. 11 show the correspondence between the magnitude and phase responses. The regions of interest in each of these maps are labeled such that red shows magnitude only areas, green shows phase only, and the areas for magnitude and phase are shown by blue. Tapping movement mainly activates regions in the motor cortex, hence for the motor tapping paradigm it is expected to see peaks in precentral gyrus. The results are encouraging and corroborate with patterns observed in the ROI analysis. The presence of these areas in phase only activation maps (without any magnitude signal change) suggests that using the phase date in fMRI may provide useful information beyond the magnitude data.

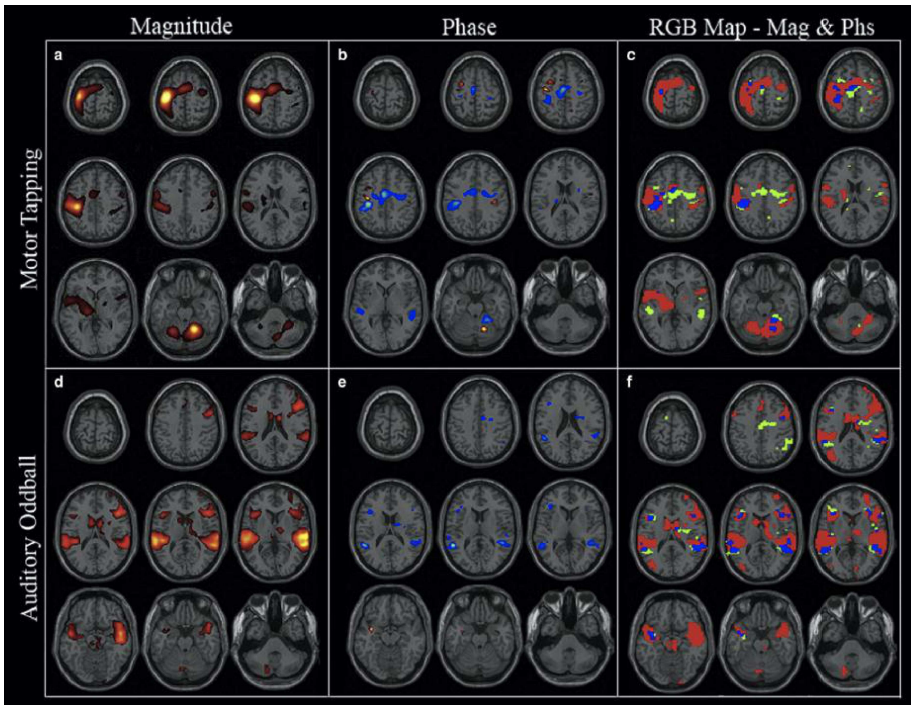

Fig. 11. Whole brain analysis results

Separate analyses of phase and magnitude fMRI data at a group level for two different paradigms were analyzed. The group statistical results show significant phase changes in both block design and event related design. The presence of phase activation in the regions expected to be activated by the task, suggests that the information in the phase might help increase the ability to isolate the task-related functional changes.

6. Data-driven analysis of complex fMRi data

6.1. Blind Source Separation (BSS) and Independent Component Analysis (ICA). Data-driven methods are based on a simple generative model and hence can minimize the assumptions on the nature of the data. They have emerged as promising alternatives to the traditional model-based approaches in many applications where the underlying dynamics are hard to characterize. Blind source separation, in particular, has been a popular data-driven approach and an active area of research. Most BSS formulations start with the linear mixing model $\boldsymbol{x} = \boldsymbol{A}\boldsymbol{s}$ with the possibility of an additive noise term), where $\boldsymbol{x}$ is the mixture that is factorized into latent variables through two matrices (a mixing matrix $\boldsymbol{A}$ and a component (source) vector $\boldsymbol{s}$ where each entry correspond to a source in random variable notation) and replaced by the observation matrix $\boldsymbol{X}$ and component matrix $\boldsymbol{S}$in an implementation. For uniqueness of the decomposition (subject to certain ambiguities), constraints are applied to the two matrices such as sparsity, uncorrelatedness, or independence of the components. ICA is a popular blind source separation technique that imposes the constraint of statistical independence on the components, i.e., source distributions and hence can recover the original sources by estimating a demixing matrix $\boldsymbol{W}$ such that $\boldsymbol{u} = \boldsymbol{W}\boldsymbol{x}$ subject to only a scaling and permutation ambiguity. It has been successfully applied to numerous data analysis problems in areas as diverse as biomedicine, communications, finance, geophysics, and remote sensing [22, 61].

To solve the source separation problem, different properties of source signals have been exploited including non-Gaussianity, non-stationarity, and sample correlation – see e.g. [58–63]. The most commonly used property among those has been non-Gaussianity. The natural cost in this context that leads to ICA is the mutual information among separated components, which can be shown to be equivalent to maximum likelihood estimation, and to negentropy maximization [40, 59, 61, 64] when we constrain the demixing matrix to be orthogonal. In these approaches, one either estimates a parametric density model [61, 63, 65, 85] along with the demixing matrix, or maximizes the information transferred in a network of non-linear units [58, 67], or estimates the entropy using a parametric or nonparametric approach [58, 63, 68, 69]. A recent semi-parametric approach uses the maximum entropy bound to estimate the entropy given the observations, and uses a numerical procedure thus resulting in accurate estimates for the entropy [42]. We have showed that the method can successfully approximate a wide class of source distributions by selecting few measuring functions, and when incorporated into ICA, the flexible density matching in this approach, ICA by entropy bound minimization (ICA-EBM) provides a very attractive trade-off between performance and computational cost [42, 70]. As presented in [71, 72], one way to incorporate prior information to an ICA algorithm is by working in a constrained optimization framework and directly adding the constraints through Lagrange multipliers. ICA-EBM, on the other hand, besides the use of such a direct constrained approach allows easy incorporation of prior information in a number of ways, in particular by selecting the best nonlinearities to model the underlying source densities.

We have made considerable progress in the development of data-driven algorithms for processing complex-valued fMRI data. Many of the approaches discussed in this paper are available in two Matlab software tools, the Group ICA of fMRI Toolbox (GIFT; http://mialab.mrn.org/software) and the LibrarY of Complex Independent component analysis Algorithms (LYCIA; http://mlsp.umbc.edu/lycis/lycia.html).

6.2. Complex ICA. When performing ICA in the complex domain, all quantities are assumed to be complex and an important result in the complex case is that one can make use of *noncircularity* to achieve source separation. Specifically, when all the sources in the mixture are improper with distinct circularity coefficients, we can achieve ICA through joint diagonalization of covariance and complementary covariance matrices to achieve source separation as in the strongly uncorrelating transform (SUT) [73, 74]. For the real-valued case, separation using second-order statistics can be achieved only when the sources have sample-to-sample correlations.

Algorithms such as joint approximate diagonalization of eigenmatrices (JADE) [75] explicitly calculate the higher-order statistics, the cumulants in the case of JADE, and can be directly used for ICA of complex-valued data. A recent extension for these algorithms [76] enables joint diagonalization of matrices that can be Hermitian and/or complex symmetric and hence can be used for more efficient ICA solutions using both the commonly used statistics and the complementary statistics that have been traditionally neglected. The algorithms that rely on joint diagonalization of cumulant matrices are robust. However, their performance suffers as the number of sources increases, and the cost of computing and diagonalizing cumulant matrices might become prohibitive for separating a large number of sources. On the other hand, ICA techniques that exploit non-Gaussianity are the more attractive solutions for the complex case as well. As in other areas for complex-valued processing, circularity assumption was a common one for the extension of popular ICA algorithms to the complex case as in complex Infomax [77, 78] and complex FastICA [78]. As expected, in the presence of noncircular sources, the performance of those algorithms suffer. There are now a number of powerful solutions available for complex ICA for the general case where sources can be either circular or noncircular, e.g., [36, 38, 41, 43, 44, 80] as well as those that adapt to different source distributions using general models such as complex generalized Gaussian distributions [43, 81], or more flexible models through efficient entropy estimation techniques as in ICA by entropy bound minimization (ICA-EBM) [70].

6.3. An application example: importance of accounting for noncircularity. Two most commonly used ICA techniques are based on maximum likelihood (ML) or maximization of negentropy (MN), and the two are equivalent when the demixing matrix is constrained to be unitary [40]. Infomax [58] has been the most widely used algorithm for analysis of fMRI data following its first application to the problem [82] and can be shown to be equivalent to maximum likelihood when the score function is matched to the source density, and in the case of orginal infomax [58] the super-Gaussian source that corresponds to the sigmoid nonlinearity (score function). Its first extension to the complex domain, circular infomax [77], assumes again a fixed nonlinearity, again of sigmoid form that matches most fMRI sources well as they tend to be mostly super-Gaussian. However, it also assumes a circular distribution, which might be quite limiting as discussed in Subsec. 2.2. Circular infomax uses the nonlinear score function that is a good match to typical super-Gaussian pdf given as

$$\varphi(u) = -\log \frac{\partial p(u)}{\partial u} = \text{sign}(u)\frac{1-\exp(-|u|)}{1+\exp(-|u|)},$$

where only the magnitude of the data has been considered and all the phase information has been discarded. In this example, we compare its performance with that of the complex version of ICA-EBM [69] as discussed in detail in [10], which is a powerful ICA approach using an adaptive density model.

Complex ICA-EBM algorithm. The complex ICA-EBM algorithm uses the minimization of the mutual information principle, which is equivalent to ML, to perform source separation. The cost function can be written as [42] $I(y) = \sum_{k=1}^{n} H(u_k) - 2\log|\det(W)| - H(x)$ here $H(u_k)$ is the entropy of the k-th spatial map. Instead of estimating $H(u_k)$ directly, complex ICA-EBM estimates the tightest bound of the entropy by assuming that the density of the sources is either weighted linear combinations or elliptical distribution. Complex ICA-EBM can obtain a reliable estimate of the bound of entropy by solving for the maximum entropy distribution that maximizes the entropy under certain constraints. The associated maximum entropy distribution includes many bivariate distributions, such as Gaussian, uniform, (double) exponential, Student t, and GGD. Let us define two density forms as $p(u) = A\exp[-au^2 - bu - cG_m(u)]$, $q(|u|) = A\exp[-a|u|^2 - cG(|u|)]$ where G_m is one of a set of pre-determined measure functions and the parameters k, a, b, and c are solved by using a normalization constraint, the associated maximum entropy distribution of s could be $kp(s_r)p(s_i)$ or $kq(|u|)$ for two different entropy bounds. Four function forms of G, including the unbounded fourth order symmetric and bounded second-order asymmetric, are considered for the first entropy bound where the density is weighted linear combinations. Two function forms of G, including fourth order symmetric and first order asymmetric, are considered for the second entropy bound where the sources are elliptical distributions. Among all the entropy estimates, only the minimum one is used as the final estimate of the entropy.

Dataset. The dataset used in the experiment is from 16 subjects performing a finger-tapping motor task while receiving auditory instructions [10]. The data are first preprocessed using the quality map phase de-noising (QPMD) [4] discussed in Subsec. 4.3. The fMRI data were multiplied by the mask generated using QMPD and smoothed for the real and imaginary parts separately. Then components are estimated using both the complex versions of Infomax and ICA-EBM.

6.4. Results of bivariate t-maps and difference t-maps. To study the statistics across subjects, we can define a bivariate t-map using the Hotelling $\boldsymbol{T}^2$-test defined as [81]

$$T^2 = N < \mathbf{s} >^T \mathbf{C}_{\overline{S}}^{-1} < \mathbf{s} >, \tag{3}$$

where N is the number of realizations of random vector s. For Hotelling T^2-test, $< s >$ in (3) represents the sample mean vector of a set of realizations from a multivariate Gaussian distributed s. For a group of subjects, we can calculate the mean image $< \mathbf{s} >$ of 16 subjects, where $< \mathbf{s} >$ represents the sample mean vector of 16 2×1 vectors for each voxel. The covariance matrix $C_{\overline{S}}$ is also defined with respect to the 16 2×1 vectors, where each 2×1 vector is treated as a realization of a 2×1 Gaussian random vector. Therefore we can construct an image of size v using (3) and the value of each pixel represents a Hotelling T^2 value, where we have assumed that the 16 2×1 vectors for each voxel are the realizations of a multivariate Gaussian distribution. Such an image might be called a group bivariate t-map. It should be noted that 16 may be too small as a sample size and the multivariate Gaussian distribution across different subjects is also assumed for simplicity.

Using the Hotelling T^2 statistic defined in (3), we construct a bivariate t-map for the two algorithms to check for voxels that are significant active across the 16 subjects. However, the fMRI images estimated by the ICA algorithms have phase rotation ambiguity and we cannot simply apply the T^2-test. The phase ambiguity, is due to the ICA model $\mathbf{x} = \mathbf{As}$. As we can observe, $\mathbf{x} = \mathbf{As} = \mathbf{A}'\mathbf{s}'$ where $\mathbf{A}' = \mathbf{AD}^{-1}$, $\mathbf{s}' = \mathbf{Ds}$ and $\mathbf{D}$ represents a diagonal matrix whose entries are complex, and hence include a magnitude and phase part. Therefore there are infinitely many solutions of A and s since D is an arbitrary diagonal phase rotation matrix. That is, for the general ICA problem, it is impossible to recover the original scale of the sources, which in the complex case includes a magnitude and a phase term.

Hence, we perform the phase rotation on each estimate to ensure that the largest magnitude of the estimate is on the real axis since that is how the data we are using is acquired. The value for each voxel in the bivariate t-map tells us how the voxel values are distributed across different subjects. High T^2-values in such figures might be regarded as an index indicating that the voxel values are probably high for all the subjects at that specific pixel and with probably lower variations across different subjects. We observed that the bivariate t-maps looked visually similar for all the four algorithms. However, in terms of hypothesis testing, the results were not the same. For hypothesis testing, we are testing $H_0 : \mu_s = 0$

versus $H_1 : \mu_s \neq 0$ where μ_s is the mean spatial map of 16 subjects. We accept H_0 if $T^2 < T^2_{\alpha,d,N-1}$ where α is the probability of Type I error (accept H_1 when H_0 is in fact true), $d-2$ is the dimension of random vector, and $N-1 = 15$ is the degrees of freedom. For instance, $T^2_{0.05,2,15} = 8.01$. We then evaluate the number of voxels for the right motor component when thresholded $T^2 > T^2_{0.05,2,15}$ at as 2761 for Infomax and as 2951 for ICA-EBM, hence resulting in significantly greater number of voxels for the flexible ICA-EBM that also accounts for noncircularity of the sources.

We can also compute difference t-maps such that given any two sets of estimated spatial maps with voxels X_{ijk} and Y_{ijk}, where X_{ijk} denotes the k-th voxel in the j-th component of the i-th subject, each voxel of 16 difference images are calculated as $D_{ijk} = X_{ijk} - Y_{ijk}$. The difference images of 16 subjects were calculated first, then a T^2-test was performed. Results of difference bivariate t-maps show that the adaptive ICA algorithms have significantly higher activation within the motor area for each class as shown in Fig. 12.

Thresholding of complex analysis results. Estimated sources for complex-valued data require a method which takes into account both phase and magnitude. The thresholding method introduced in [4] takes into account the phase by using a Mahalanobis distance metric in the real and imaginary data of the estimated sources given by $d_{k,i} = \sqrt{[\widehat{\mathbf{s}}_{k,i} - \boldsymbol{\mu}_k]^T \mathbf{C}_k^{-1} [\widehat{\mathbf{s}}_{k,i} - \boldsymbol{\mu}_k]}$ where $\widehat{\mathbf{s}}_{k,i} = [\widehat{s}_{k,i,r,e}, \widehat{s}_{k,i,im}]^T$; and μ_k and CZ_k are the corresponding mean and covariance of the estimated sources. Figure 13 shows results with this new Z-score that takes the complex nature of data fully into account. An additional challenge for fMRI group studies using complex-valued ICA is the well-known inherent scaling ambiguity of ICA algorithms, which in the complex case includes a phase term. Hence, for complex-valued ICA, the phase term in the scaling ambiguity presents an additional problem, since the estimated distribution of matching components across subjects then will have different unknown rotations (in the complex plane), without phase ambiguity correction, they can add destructively, hence creating group average component images with lower magnitude and noisy phase images. In [4], two effective approaches are introduced to correct for the phase ambiguity such that successful group results can be obtained and presented using complex fMRI data. In Fig. 12, we show the estimation results for a motor component where a total of 30 components were estimated using circular Infomax [76] using data from 16 subjects performing a finger-tapping task, and using the Mahalanobis z-score.

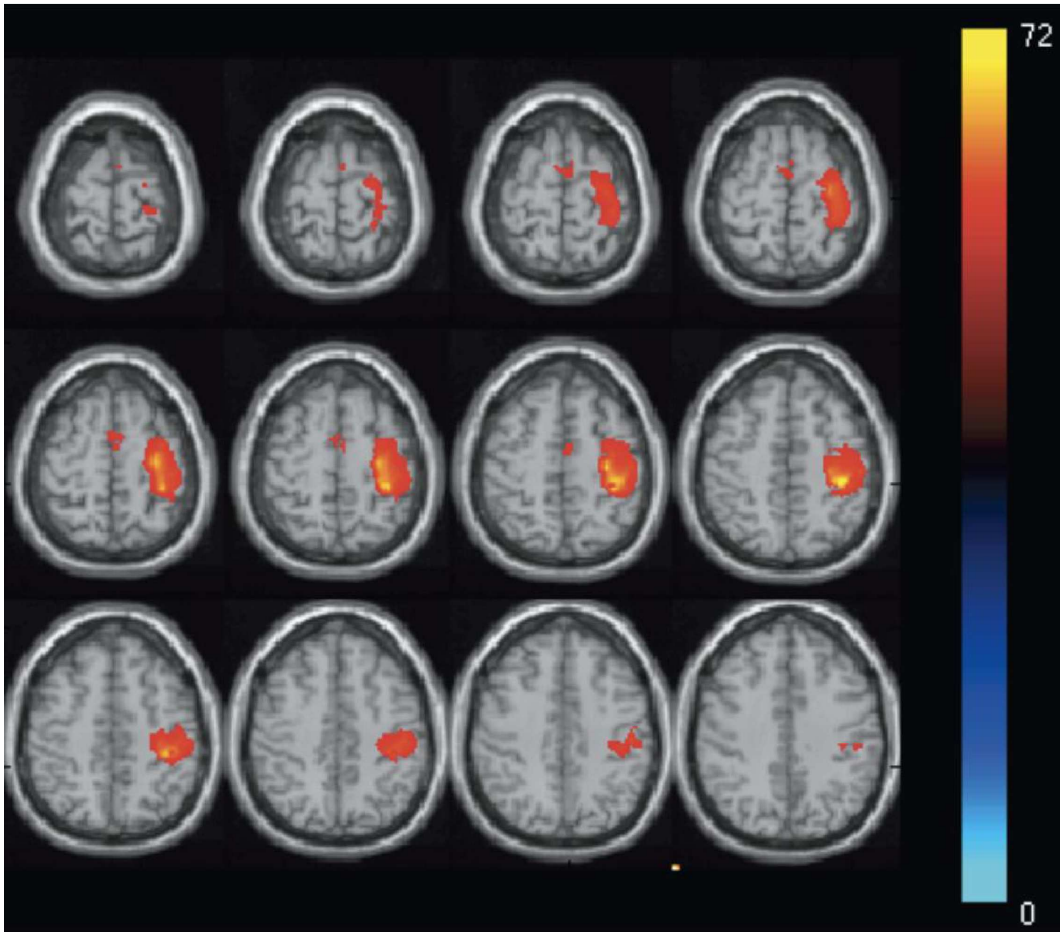

Fig. 12. Difference bivariate t-map for the motor component with ICA-EBM and circular Infomax

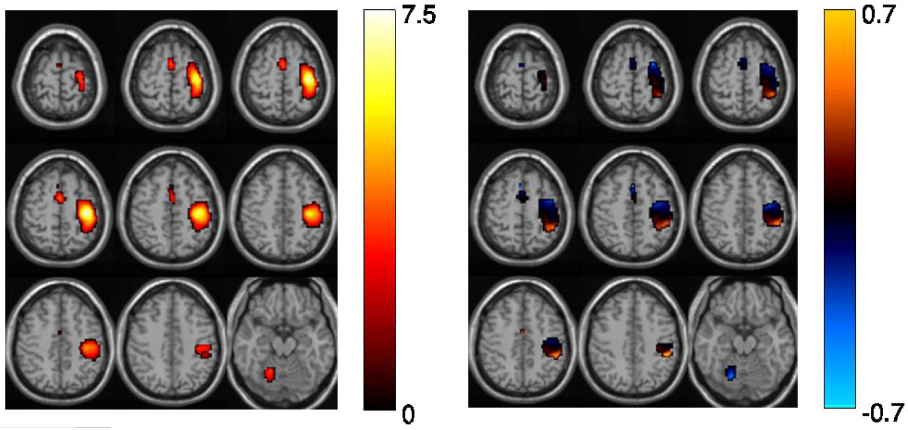

Fig. 13. Mean magnitude (left) and phase (right) maps for the motor component (Mahalanobis z-score of 4)

7. Summary

In summary, we believe there is great potential in using the phase information in an fMRI analysis. The convergence of biophysical models and simulation approaches, high-field and high-resolution data acquisition, preprocessing and denoising approaches, and statistical modeling approaches which utilize the fully complex data are pushing the field forward. However significant challenges still remain and need to be addressed before complex-valued fMRI data will become a mainstream approach.

Acknowledgements. This work was supported by NSF grants 0715022, 0840895, 0635129 and 0612076.

REFERENCES

[1] S. Ogawa, D.W. Tank, R. Menon, J.M. Ellermann, S.G. Kim, H. Merkle , and K. Ugurbil, "Intrinsic signal changes accompanying sensory stimulation, functional brain mapping with magnetic resonance imaging", *Proc. Natl. Acad. Sci.* 89 (13), 5951–5955 (1992).

[2] N. Petridou, A. Schafer. P. Gowland, and R. Bowtell, "Phase vs. magnitude information in functional magnetic resonance imaging time series, toward understanding the noise", *Magn. Reson. Imaging* 27 (8), 1046–57 (2009).

[3] P. Rodriguez, V.D. Calhoun, and T. Adali, "Phase ambiguity correction and visualization techniques for complex-valued ICA of group fMRI data, *Pattern Recognition* 45 (6), 2050–2063 (2012).

[4] P. Rodriguez, N. Correa, T. Adali, T. Eichele, and V.D. Calhoun, "Quality map thresholding for de-noising of complex-valued fmri data and its application to ICA of fMRI", *J. Signal Processing Systems* 1, 1–16 (2009).

[5] T. Adali and V.D. Calhoun, "Complex ICA of brain imaging data", *IEEE Signal Proc. Magazine* 24 (5), 136–139 (2007).

[6] S. Arja, Z. Feng, Z. Chen, A. Caprihan, K.A. Kiehl, T. Adali, and V.D. Calhoun, "Changes in fMRI magnitude data and phase data observed in block-design and event-related tasks", *NeuroImage* 49 (4), 3149–3160 (2010).

[7] V.D. Calhoun and T. Adali, "Complex ICA for fMRI analysis, performance of several approaches", *Proc. ICASSP* 1, CD-ROM (2003).

[8] V.D. Calhoun, T. Adali, G.D. Pearlson, P.C. van Zijl and J.J. Pekar, "Independent component analysis of fMRI data in the complex domain", *Magn. Reson. Med.* 48 (1), 180–192 (2002).

[9] H. Li, T. Adali, N. Correa, P. Rodriguez, and V.D. Calhoun, "Flexible complex ICA of fMRI data", *Proc. ICASSP* 1, CD-ROM (2010).

[10] H. Li, N. Correa, V.D. Calhoun, and T. Adali, "Application of independent component analysis with adaptive density model to complex-valued fMRI data", *IEEE Trans. Biomed. Eng.* I 58 (10), 2794–2803 (2011).

[11] F. G. Hoogenraad, P.J. Pouwels, M.B. Hofman, J.R. Reichenbach, M. Sprenger, and E.M. Haacke, "Quantitative differentiation between BOLD models in fMRI", *Magn. Reson. Med.* 45 (2), 233–246 (2001).

[12] F.G Hoogenraad, J.R. Reichenbach, E.M. Haacke, S. Lai, K. Kuppusamy, and M. Sprenger, "In vivo measurement of changes in venous blood-oxygenation with high resolution functional MRI at 0.95 tesla by measuring changes in susceptibility and velocity", *Magn. Res. Med.* 39 (1), 97–107 (1998).

[13] R. Menon, "Postacquisition suppression of large-vessel BOLD signals in high-resolution fMRI", *Magn. Res. Med.* 47 (1), 1–9 (2002).

[14] D.B. Rowe, "Parameter estimation in the magnitude-only and complex-valued fMRI data models", *Neuroimage* 25 (4), 1124–32 (2005b).

[15] D.B. Rowe, "Modeling both the magnitude and phase of complex-valued fMRI data", *Neuroimage* 25(4), 1310–24 (2005a).

[16] D.B. Rowe and B.R. Logan, "A complex way to compute fMRI activation", *Neuroimage* 23 (3), 1078–92 (2004).

[17] D.B. Rowe and B.R. Logan, "Complex fMRI analysis with unrestricted phase is equivalent to a magnitude-only model", *Neuroimage* 24 (2), 603–6 (2005).

[18] A.S. Nencka and D.B. Rowe, "Reducing the unwanted draining vein BOLD contribution in fMRI with statistical post-processing methods", *Neuroimage* 37 (1), 177–88 (2007).

[19] D.G. Tomasi and E.C. Caparelli, "Macrovascular contribution in activation patterns of working memory", *J. Cereb. Blood Flow Metab.* 27 (1), 33–42 (2007).

[20] F. Zhao, T. Jin, P. Wang, X. Hu, and S.G. Kim, "Sources of phase changes in BOLD and CBV-weighted fMRI", *Magn. Reson. Med.* 57 (3), 520–7 (2007).

[21] Z. Feng, A. Caprihan, K. Blagoev and V.D. Calhoun, "Biophysical modeling of phase changes in BOLD fMRI", *NeuroImage* 47, 540–548 (2009).

[22] T. Adali and S. Haykin, *Adaptive Signal Processing Next Generation Solutions*, Wiley-IEEE Press, New York, 2010.

[23] T. Adali, P.J. Schreier, and L.L. Scharf, "Complex-valued signal processing, The proper way to deal with impropriety", *IEEE Trans. Signal Processing* 59 (11), 5101–5123 (2011).

[24] B. Picinbono and P. Chevalier, "Widely linear-estimation with complex data", *IEEE Trans. on Signal Processing* 43 (8), 2030–2033 (1995).

[25] P. Schreier and L.L. Scharf, "Second-order analysis of improper complex random vectors and processes", *IEEE Trans. on Signal Processing* 51 (3), 714–725 (2003).

[26] P. Schreier and L.L. Scharf, "Statistical signal processing of complex-valued data", *The Theory of Improper and Noncircular Signals* 1, CD-ROM (2010).

[27] K. Kreutz-Delgago, *The Complex Gradient Operator and the CR-Calculus*, University of California, San Diego, 2007.

[28] W. Wirtinger, Zur formalen theorie der funktionen von mehr complexen veräänderlichen, *Math. Ann.* 97, 357–375 (1927).

[29] B. Picinbono, "On circularity", *IEEE Trans. Signal Processing* 42, 3473–3482 (1994).

[30] P. Chevalier and F. Pipon, "New insights into optimal widely linear array receivers for the demodulation of BPSK, MSK, and GMSK signals corrupted by noncircular interferences – application to SAIC", *IEEE Trans. Signal Processing* 54 (3), 870–883 (2006).

[31] F. Roemer and M. Haardt, "Efficient 1-D and 2-D DOA estimation for non-circular sources with hexagonal shaped espar arrays", *Proc. IEEE Int. Conf. Acoust. Speech, Signal Processing (ICASSP)* 1, 881–884 (2007).

[32] E. Hardy, D. Hoferer, D. Mertens, and G. Kasper, "Automated phase correction via maximization of the real signal", *Mag. Res. Imag.* 27, 393–400 (2009).

[33] A. Macovski, "Noise in MRI", *Magn. Res. Med.* 36 (3), 494–497 (1996).

[34] D.H. Brandwood, "A complex gradient operator and its application in adaptive array theory", *Proc. Inst. Elect. Eng.* 1, 11–16 (1983).

[35] K.B Petersen and M.S. Pedersen, *The Matrix Cookbook*, Technical University of Denmark, Copenhagen, 2008.

[36] H. Li, T. Adali, "Complex-valued adaptive signal processing using nonlinear functions", *J. Advances in Signal Processing* B, 1–9 (2008).

[37] A. Van den Bos, "Complex gradient and Hessian", *IEE Proc. Vision, Image, and Signal Processing* 1, 380–382 (1994).

[38] T. Adali, T. Kim, and V.D. Calhoun, "Independent Component analysis by complex nonlinearities", *Proc. ICASSP* 1, 525–528 (2004).

[39] T. Adali and H. Li, *Complex-Valued Adaptive Signal Processing, Adaptive Signal Processing, Next Generation Solutions*, Wiley, New York, 2009.

[40] T. Adali, M. Novey, and J.F. Cardoso, "Complex ICA using nonlinear functions", *IEEE Trans. Signal Processing* 59 (9), 4356–4544 (2008).

[41] H. Li and T. Adali, "A class of complex ICA algorithms based on the kurtosis cost function", *IEEE Trans. Neural Netw.* 19 (3), 408–420 (2008).

[42] X. Li and T. Adali, "Independent component analysis by entropy bound minimization", *IEEE Trans. on Signal Processing* 58 (10), 5151–5164 (2010).

[43] M. Novey and T. Adali, "Complex ICA by negentropy maximization", *IEEE Trans. Neural Networks* 19 (4), 596–609 (2008).

[44] M. Novey and T. Adali, "On extending the complex FastICA algorithm to noncircular sources", *IEEE Trans. Signal Processing* 56 (5), 2148–2154 (2008).

[45] J. Martindale, A.J. Kennerley, D. Johnston, Y. Zheng, and J.E. Mayhew, "Theory and generalization of Monte Carlo models of the BOLD signal source", *Magnetic Resonance in Medicine* 59 (3), 607–618 (2008).

[46] J.P. Marques and R.W. Bowtell, "Using forward calculations of the magnetic field perturbation due to a realistic vascular model to explore the BOLD effect", *NMR Biomed.* 21 (6), 553–65 (2008).

[47] Z. Chen, A. Caprihan, and V.D. Calhoun, "Effect of surrounding vasculature on intravoxel BOLD signal", *Med.Phys.* 37 (4), 1778–1787 (2010).

[48] K.M. Koch, X. Papademetris, D.L. Rothman, and R.A. de Graaf, "Rapid calculations of susceptibility-induced magnetostatic field perturbations for in vivo magnetic resonance", *Physics in Medicine and Biology* 51 (24), 6381–6402 (2006).

[49] D.A. Yablonskiy and E.M. Haacke, "Theory of NMR signal behavior in magnetically inhomogeneous tissues, the static dephasing regime", *Magn. Reson. Med.* 32 (6), 749–63 (1994).

[50] W.M. Spees, D.A. Yablonskiy, M.C. Oswood, and J.J. Ackerman, "Water proton MR properties of human blood at 1.5 Tesla, magnetic susceptibility, T(1), T(2), T*(2), and non-Lorentzian signal behavior", *Magn. Reson. Med.* 45 (4), 533–42 (2001).

[51] A.C. Guyton and J.E. Hall, *Textbook of Medical Physiology,* W.B. Saunders Company, Philadelphia, 1996.

[52] L. Freire, A. Roche, and J.F. Mangin, "What is the best similarity measure for motion correction in fMRI time series?", *IEEE Trans. Med. Imaging* 21 (5), 470–484 (2002).

[53] E.M. Haacke, N.Y. Cheng, M.J. House, Q. Liu, J. Neelavalli, R.J. Ogg, A. Khan, M. Ayaz, W. Kirsch, and A. Obenaus, "Imaging iron stores in the brain using magnetic resonance imaging", *Magn. Reson. Imaging* 23 (1), 1–25 (2005).

[54] S. Khullar, A. Michael, N. Correa, T. Adali, S. Baum, and V.D. Calhoun, "Wavelet-based fMRI analysis, 3-D denoising, signal separate, and validation metrics", *NeuroImage* 54 (4), 2867–2884 (2011).

[55] G. Gilboa, N. Sochen, and Y.Y. Zeevi, "Image enhancement and denoising by complex diffusion processes", *IEEE Trans. Pattern Anal. Mach. Intell* 26 (8), 1020–36 (2004).

[56] T. Adali and H. Li, "A practical formulation for computation of complex gradients and its application to maximum likelihood", *Proc. ICASSP* 1, CD-ROM (2007).

[57] D.B. Rowe, C.P. Meller, and R.G. Hoffmann, "Characterizing phase-only fMRI data with an angular regression model", *J. Neurosci. Methods* 161 (2), 331–41 (2007).

[58] A.J. Bell and T.J. Sejnowski, "An information maximisation approach to blind separation and blind deconvolution", *Neural Computing* 7 (6), 1129–1159 (1995).

[59] P. Comon, "Independent component analysis – a new concept?", *Signal Proc.* 36, 287–314 (1994).

[60] A. Hyvarinen, "One-unit contrast functions for independent component analysis. A statistical analysis", *Proc. NNSP* 1, 388–397 (1997).

[61] A. Hyvarinen, J. Karhunen, and E. Oja, *Independent Component Analysis,* Johns Wiley & Sons, New York, 2001.

[62] Z. Koldovsky, P. Tichavski, and E. Oja, "Efficient variant of algorithm FastICA for independent component analysis attaining the Cramer-Rao lower bound", *IEEE Trans. Neural Netw*. 17 (5), 1265–77 (2006).

[63] E.G. Learned-Miller, J.W. Fisher III, and T.W. Lee, "ICA using spacings estimates of entropy", *J. Machine Learning Research* 4, 1271–1295, (2003).

[64] J.F. Cardoso, "Blind signal separation, statistical principles", *Proc. IEEE* 9 (10), 2009–2025 (1998).

[65] J.A. Palmer, S. Makeig, K. Kreutz-Delgago, and B.D. Rao, "Newton method for the ICA mixture model", *Proc. IEEE Int. Conf. Acoust. Speech, Signal Processing* 1, CD-ROM (2008).

[66] D.T. Pham and P. Garat, Blind separation of mixture of independent sources through a quasi-maximum likelihood approach, *IEEE Trans. Signal Proc*. 45 (7), 1712–1725 (1997).

[67] T.W. Lee, M. Girolami, and T.J. Sejnowski, "Independent Component Analysis Using an Extended Infomax Algorithm for Mixed Subgaussian and Supergaussian Sources, *Neural Comput.* 11, 417–441 (1999).

[68] D. Erdogmus, K.E. Hild, Y. Rao, and J.C. Principe, "Minimax mutual information approach for independent component analysis", *Neural Comput*. 16 (1235), 1252 (2004).

[69] A. Hyvarinen, "New approximations of differential entropy for independent component analysis and projection pursuit", *Advances in Neural Inf. Proc. Sys*. 10, 273–279 (1998).

[70] X. Li and T. Adali, "Complex independent component analysis by entropy bound minimization", *IEEE Trans. Circuits and Systems* I 57 (7), 1417–1430 (2010).

[71] W. Lu W and J.C. Rajapakse, "Constrained independent component analysis", in *Adv. Neural Inf. Proc. Sys.* pp. 570–576, MIT Press, Cambridge, 2000.

[72] W. Lu and J.C. Rajapakse, "ICA with reference", *Proc. Int. Conf. on ICA and BSS* 1, 120–125 (2001).

[73] L. De Lathauwer and B. De Moor, "On the blind separation of non-circular sources", *Proc. Eur. Signal Process. Conf. (EUSIPCO)* 1, CD-ROM (2002).

[74] J. Eriksson and V. Koivunen, "Complex random vectors and ICA models, Identifiability, uniqueness and separability", *IEEE Trans. Info. Theory* 52 (3), 1017–1029 (2006).

[75] J.F. Cardoso and A. Souloumiac, "Blind beamforming for non Gaussian signals", *IEE-Proc.* F 140 (6), 362–370 (1993).

[76] T. Trainini, X.-L. Li, E. Moreau, and T. Adali, "A relative gradient algorithm for joint decompositions of complex matrices", *Proc. Eur. Signal Process. Conf. (EUSIPCO)* 1, CD-ROM (2010).

[77] J.T.J. Annemueller, T.J. Sejnowski, and S. Makeig, "Complex Independent component analysis of frequency-domain electroencephalographic data", *Neural Networks* 16, 1311–1323 (2003).

[78] P. Smaragdis, "Blind separation of convolved mixtures in the frequency domain", *Neurocomputing* 22 (1–3), 21–34 (1998).

[79] E. Bingham and A. Hyvarinen, "A fast fixed-point algorithm for independent component analysis of complex-valued signals", *Int. J. Neural Syst*. 10 (1), 1–8 (2000).

[80] V.P. Zarzoso and P. Comon, "Robust independent component analysis by iterative maximization of the kurtosis contrast with algebraic optimal step size", *IEEE Trans. Neural Netw.* 21 (2), 248–61 (2010).

[81] M. Novey and T. Adali, "A complex generalized Gaussian distribution-characterization, generation, and estimation", *IEEE Trans. on Signal Processing* 58 (3), 1427–1433 (2010).

[82] M.J. McKeown, S. Makeig, G.G. Brown, T.P. Jung, S.S. Kindermann, A.J. Bell, and T.J. Sejnowski, "Analysis of fMRI data by blind separation into independent spatial components", *Human Brain Mapping* 6, 160–188 (1998).

[83] A.C. Rencher, *Methods of Multivariate Analysis,* John Wiley & Sons, New York, 1995.

[84] J.A. Mumford and T. Nichols, "Modeling and inference of multisubject fMRI data", *IEEE Eng Med. Biol. Mag.* 25 (2), 42–51 (2006).

[85] J. Karvanen, J. Eriksson, and V. Koivunen, "Pearson system based method for blind separation", *Proc. Second Int. Workshop on ICA* 1, CD-ROM (2000).

BULLETIN OF THE POLISH ACADEMY OF SCIENCES
TECHNICAL SCIENCES, Vol. 60, No. 3, 2012
DOI: 10.2478/v10175-012-0051-4

Fast and unique Tucker decompositions via multiway blind source separation

G. ZHOU[1,2] and A. CICHOCKI[3,4,5*]

[1] Laboratory for Advanced Brain Signal Processing, RIKEN, Brain Science Institute, Wako-shi, Saitama 3510198, Japan
[2] School of Electronic and Information Engineering, South China University of Technology, Guangzhou 510641, China
[3] RIKEN Brain Science Institute, 2-1 Hirosawa Wako City, Saitarna 351-0198, Japan
[4] Electrotechnical Faculty, Warsaw University of Technology, 1 Politechniki Sq., 00-661 Warszawa, Poland
[5] System Research Institute, 6 Newelska St., 01-447 Warszawa, Poland

Abstract. A multiway blind source separation (MBSS) method is developed to decompose large-scale tensor (multiway array) data. Benefitting from all kinds of well-established constrained low-rank matrix factorization methods, MBSS is quite flexible and able to extract unique and interpretable components with physical meaning. The multilinear structure of Tucker and the essential uniqueness of BSS methods allow MBSS to estimate each component matrix separately from an unfolding matrix in each mode. Consequently, alternating least squares (ALS) iterations, which are considered as the *workhorse* for tensor decompositions, can be avoided and various robust and efficient dimensionality reduction methods can be easily incorporated to pre-process the data, which makes MBSS extremely fast, especially for large-scale problems. Identification and uniqueness conditions are also discussed. Two practical issues dimensionality reduction and estimation of number of components are also addressed based on sparse and random fibers sampling. Extensive simulations confirmed the validity, flexibility, and high efficiency of the proposed method. We also demonstrated by simulations that the MBSS approach can successfully extract desired components while most existing algorithms may fail for ill-conditioned and large-scale problems.

Key words: Multiway Blind Source Separation (MBSS), Multilinear Independent Component Analysis (MICA), Constrained tensor decompositions, Tucker models, Nonnegative Tucker Decomposition (NTD).

1. Introduction and problem statement

How to find informative and sparse/compact representations of massive experimental or measured multidimensional large-scale tensor data is a fundamental and challenging problem in data mining and data analysis. Although the basic models for tensor (i.e., multiway array) decompositions such as Canonical Polyadic (CP) and Tucker decomposition models were proposed a long time ago [1–4], they have only recently emerged as promising tools for exploratory analysis of multi-dimensional data in diverse applications, especially in dimensionality reduction, feature extraction, Independent Component Analysis (ICA), classification, prediction, multiway clustering, and data mining [4, 5]. By virtue of their multiway nature, tensors provide powerful tools for analysis and fusion of large-scale, multi-modal, massive data together with a mathematical backbone for the discovery of underlying hidden complex data structures [4, 7–9]. From the data analysis point of view, tensor decompositions are very attractive because they take into account spatial, temporal and spectral information, and provide links among the various extracted factors or latent variables with physical or physiological meanings and interpretations [5, 8, 10]. For example, tensor representations and decompositions allow us to investigate temporal, spatial and spectral independent components and links among them. Moreover, tensor decompositions are emerging techniques for data fusion, pattern recognition, object detection, classification, multiway clustering, Blind Source Separation (BSS), sparse representation and coding [11–17], etc.

Most of the existing tensor decomposition methods are focused on the minimum fitting error to the data. However, quite different from the matrix case, the optimal low-rank approximation may not exist at all [18] or, if it exists, may not be unique for high-order tensors [7, 19, 20]. Particularly, for Tucker decompositions the results are always non-unique due to rotational freedom. As a result the extracted factors often lack of physical meaning and are hard to interpret. To overcome this drawback, constrained tensor decompositions have received increasing interest in recent years. In this regard, several authors have proposed applying ICA to the CP and Tucker models, i.e., impose statistical independence in at least one mode [21–24]. For example, in the methods proposed in [21] and [22] ICA was combined with the CP model. However, the CP model and its associated algorithms are often too restrictive as the number of components in each mode is the same and there are no mutual interactions between components in different modes. Very recently Unkel *et al.* (2011) proposed a two-step method based on the Tucker-3 model in which ordinary Tucker decomposition is performed first and then statistical independence is imposed to refine the components in only one mode by exploiting the rotational freedom of the Tucker model [24]. Furthermore, Vasilescu and Terzopoulos (2005) proposed a multilinear ICA method which is also a two-step method but independence can be imposed on either all the temporal components or the mixing matrix (spatial components) [23]. However, this approach has not been investigated deeply and only ICA is considered.

*e-mail: cia@brain.riken.jp

On the other hand, in the (2D) matrix case, very efficient low-rank constrained matrix factorization techniques (also called penalized matrix factorizations) have been developed, such as principal component analysis (PCA), ICA [25–28], sparse component analysis (SCA) [29, 30], smooth component analysis (SmoCA) [5] and nonnegative matrix factorization (NMF) [5, 31], just to name a few. These matrix factorization techniques have their own bias, advantages, and are widely applied to blind source separation (BSS), dimensionality reduction, data compression and feature extraction, by exploiting various assumptions and *a priori* knowledge. We do not intend to duplicate these works which have been done for matrices. Instead, we would like to show that such well-established matrix factorization methods (especially, NMF, SCA and ICA) can be extended to tensor scenarios directly and uniformly. Motivated by efficiency and high level of flexibility of BSS and various Component Analysis methods, we investigate in this paper a multiway BSS (MBSS) approach to perform constrained tensor decompositions with various constraints and diversities[1], in order to provide more interpretable, essentially unique[2] components with physical meanings. To the best of our knowledge, till now there was no available systematic investigation of the validity and performance of this approach which could incorporate any powerful and flexible BSS techniques (beyond ICA[3]) to tensor decompositions. Finally, the MBSS method can be viewed as a generalization and extension of the wide variety of BSS techniques and algorithms to multiway data.

The remainder of the paper is organized as follows. In Sec. 2 basic models and concepts for Tucker decomposition are briefly introduced. In Sec. 3 the flexible and general scheme of Multiway BSS is developed, as well as the discussion on identifiability and uniqueness conditions are provided. In Sec. 4 a method for dimensionality reduction and estimation of the number of components is addressed. Finally, some simulation results are presented in Sec. 5 and conclusions are made in Sec. 6.

Basic notations. Tensors are denoted by underlined capital boldface letters, e.g., $\underline{\mathbf{Y}} \in \mathbb{R}^{I_1 \times I_2 \times \cdots \times I_N}$. The order of a tensor is the number of modes, also known as ways or dimensions (e.g., space, time, frequency, subjects, trials, classes, groups, and conditions). In contrast, matrices (two-way tensors) are denoted by boldface capital letters, e.g., $\mathbf{Y}$; vectors (one-way tensors) are denoted by boldface lowercase letters, e.g., the columns of a matrix $\mathbf{A}$ are denoted by $\mathbf{a}_j$, and scalars are denoted by lowercase letters, e.g., a_{ij}.

The mode-n product $\underline{\mathbf{Y}} = \underline{\mathbf{G}} \times_n \mathbf{A}$ of a tensor $\underline{\mathbf{G}} \in \mathbb{R}^{J_1 \times J_2 \times \cdots \times J_N}$ and a matrix $\mathbf{A} = [a_{i,j_n}] \in \mathbb{R}^{I \times J_n}$ is a tensor $\underline{\mathbf{Y}} \in \mathbb{R}^{J_1 \times \cdots \times J_{n-1} \times I \times J_{n+1} \times \cdots \times J_N}$, with elements $y_{j_1,j_2,\ldots,j_{n-1},i,j_{n+1},\ldots,j_N} = \sum_{j_n=1}^{J_n} (g_{j_1,j_2,\ldots,j_N})(a_{i,j_n})$. The symbol $\otimes$ denotes the Kronecker product, i.e., $\mathbf{A} \otimes \mathbf{B} = [a_{ij}\mathbf{B}]$, and the symbol $\odot$ denotes the Khatri-Rao product or column-wise Kronecker product, i.e., $\mathbf{A} \odot \mathbf{B} = [\mathbf{a}_1 \otimes \mathbf{b}_1 \cdots \mathbf{a}_J \otimes \mathbf{b}_J]$. Unfolding (matricization, flattening) of a tensor $\underline{\mathbf{Y}} \in \mathbb{R}^{I_1 \times I_2 \times \cdots \times I_N}$ in mode-n is denoted as $\mathbf{Y}_{(n)} \in \mathbb{R}^{I_n \times \overline{I_{p \neq n}} I_p}$, which consists of arranging all possible mode-n tubes (vectors) as the columns of the unfolded matrix [4]. For simplicity, we define $\breve{I}_n = \Pi_{p \neq n} I_p$, $\breve{J}_n = \Pi_{p \neq n} J_p$, $\bigotimes_{p \neq n} \mathbf{A}^{(p)} = \mathbf{A}^{(N)} \otimes \cdots \mathbf{A}^{(n+1)} \otimes \mathbf{A}^{(n-1)} \cdots \otimes \mathbf{A}^{(1)}$ and $\bigodot_{p \neq n} \mathbf{A}^{(p)} = \mathbf{A}^{(N)} \odot \cdots \mathbf{A}^{(n+1)} \odot \mathbf{A}^{(n-1)} \cdots \odot \mathbf{A}^{(1)}$. Readers are referred to [4, 5] for more details about the notations and tensor operations.

2. Tucker decomposition models

Tucker decomposition has been received intensive study in recent years as one of the most important and flexible tensor decomposition models. In Tucker decompositions, the data are decomposed as the product of a core tensor with N mode component matrices [2] (see Fig. 1), i.e., a given data tensor $\underline{\mathbf{Y}} \in \mathbb{R}^{I_1 \times I_2 \times \cdots \times I_N}$ is decomposed as

$$\begin{aligned} \underline{\mathbf{Y}} &= \underline{\mathbf{G}} \times_1 \mathbf{A}^{(1)} \times_2 \mathbf{A}^{(2)} \cdots \times_N \mathbf{A}^{(N)} + \underline{\mathbf{E}} = \widehat{\underline{\mathbf{Y}}} + \underline{\mathbf{E}} \\ &= \sum_{j_1=1}^{J_1} \cdots \sum_{j_N=1}^{J_N} g_{j_1 j_2 \cdots j_N} \left(\mathbf{a}_{j_1}^{(1)} \circ \mathbf{a}_{j_2}^{(2)} \cdots \circ \mathbf{a}_{j_N}^{(N)} \right) + \underline{\mathbf{E}}, \end{aligned} \tag{1}$$

where $\underline{\mathbf{G}} \in \mathbb{R}^{J_1 \times J_2 \times \cdots \times J_N}$ is the core tensor, $\mathbf{A}^{(n)} = [\mathbf{a}_1^{(n)}, \mathbf{a}_2^{(n)}, \ldots, \mathbf{a}_{J_n}^{(n)}] \in \mathbb{R}^{I_n \times J_n}$ is the mode-n component matrix for $n = 1, 2, \cdots, N$, and the tensor $\underline{\mathbf{E}} \in \mathbb{R}^{I_1 \times I_2 \times \cdots \times I_N}$ represents errors or noise. We may also use a shorter notation for (1) in the form $\widehat{\underline{\mathbf{Y}}} = [\![\underline{\mathbf{G}}; \mathbf{A}^{(1)}, \mathbf{A}^{(2)}, \ldots, \mathbf{A}^{(N)}]\!]$ for simplicity [4].

To extract the latent factors $\mathbf{A}^{(n)}$ from $\underline{\mathbf{Y}}$, a Tucker-1 model is often useful

$$\underline{\mathbf{Y}} \approx \underline{\mathbf{G}}^{(-n)} \times_n \mathbf{A}^{(n)}, \tag{2}$$

where

$$\begin{aligned} \underline{\mathbf{G}}^{(-n)} &= \underline{\mathbf{G}} \times_1 \mathbf{A}^{(1)} \cdots \times_{n-1} \mathbf{A}^{(n-1)} \\ &\quad \times_{n+1} \mathbf{A}^{(n+1)} \cdots \times_N \mathbf{A}^{(N)}, \end{aligned}$$

or by using unfolding operations and matrix representation

$$\mathbf{Y}_{(n)} \approx \mathbf{A}^{(n)} \mathbf{G}_{(n)}^{(-n)} = \mathbf{A}^{(n)} [\mathbf{B}^{(n)}]^T, \tag{3}$$

where

$$\mathbf{G}_{(n)}^{(-n)} = \mathbf{G}_{(n)} \left[\bigotimes \mathbf{A}^{(p)} \right]^T \stackrel{\text{def}}{=} [\mathbf{B}^{(n)}]^T. \tag{4}$$

In other words, $\mathbf{A}^{(n)}$ and $\mathbf{G}_{(n)}$ are solutions to the following least-square problem[4]:

$$\min \left\| \mathbf{Y}_{(n)} - \mathbf{A}^{(n)} \mathbf{B}^{(n)T} \right\|_F^2, \qquad (n = 1, 2, \ldots, N). \tag{5}$$

[1] By diversity, we mean different characteristics, features or morphology of source signals or hidden latent variables [27].

[2] By essentially unique, we understand a unique decomposition with arbitrary scaling and permutation of components.

[3] By "beyond ICA", we understand that any BSS method can be applied, e.g., PCA/SVD, NMF, SCA.

[4] Alternatively, we can solve the least-square problem $\min \|\mathbf{Y}_{(n)}^{(-n)} - \mathbf{A}^{(n)} \mathbf{G}_{(n)}\|_F^2$ instead, where $\mathbf{Y}_{(n)}^{(-n)}$ is the mode-n unfolding of tensor $\underline{\mathbf{Y}}^{(-n)} = \underline{\mathbf{Y}} \times_1 [\mathbf{A}^{(1)\dagger}] \cdots \times_{n-1} [\mathbf{A}^{(n-1)\dagger}] \times_{n+1} [\mathbf{A}^{(n+1)\dagger}] \cdots \times_N [\mathbf{A}^{(N)\dagger}]$.

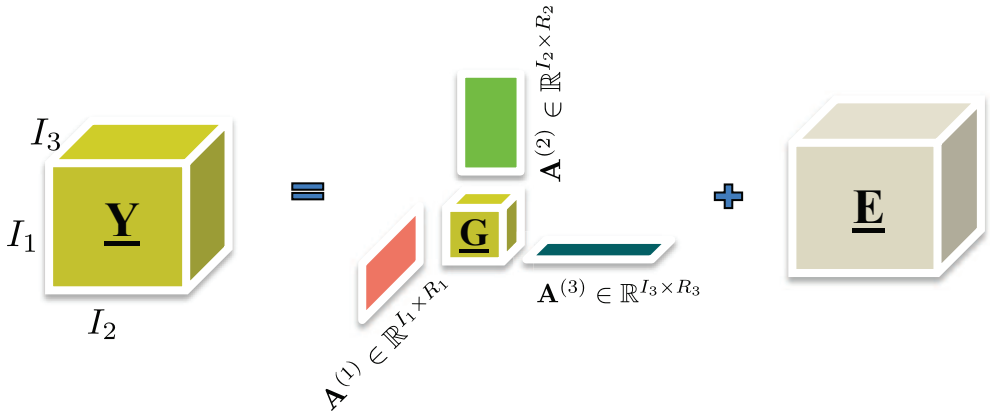

Fig. 1. Illustration of a 3-way tensor decomposition using the Tucker-3 model. The objective is to estimate the components $\mathbf{a}_{j_n}^{(n)}$, i.e., columns of the component matrices $\mathbf{A}^{(n)} = [\mathbf{a}_1^{(n)}, \mathbf{a}_2^{(n)}, \ldots, \mathbf{a}_{J_n}^{(n)}] \in \mathbb{R}^{I_n \times J_n}$, with desired diversities or statistical properties, and a possibly sparse core tensor $\underline{\mathbf{G}} \in \mathbb{R}^{J_1 \times J_2 \times J_3}$, typically with $J_n \ll I_n$, $(n = 1, 2, 3)$. Instead of applying the standard Alternating Least Squares (ALS) algorithms to the Tucker-3 model, we can apply the unfolding of the data tensor according to the Tucker-1 models and then perform constrained matrix factorizations for the unfolded matrices (multiway BSS) by imposing desired constraints (e.g., nonnegativity, sparseness, statistical independence, smoothness or decorrelation, etc)

Hence, $\mathbf{A}^{(n)}$ and $\underline{\mathbf{G}}$ can be updated sequentially by freezing all set of matrices except one

$$\begin{aligned} \mathbf{A}^{(n)} &\leftarrow \mathbf{Y}_{(n)}[\mathbf{B}^{(n)}]^{\dagger}, \qquad (n = 1, 2, \ldots, N), \\ \underline{\mathbf{G}} &\leftarrow \underline{\mathbf{Y}} \times_1 \mathbf{A}^{(1)\dagger} \times_2 \mathbf{A}^{(2)\dagger} \cdots \times_N \mathbf{A}^{(N)\dagger}, \end{aligned} \tag{6}$$

where † denotes the Moore-Penrose pseudo inverse of matrices. To achieve the optimal fitting error, the above steps are repeated till convergence. These update rules are often referred to as alternating least-square (ALS) method.

From the above analysis, standard ALS methods involve frequently unfolding operations and matrix-matrix Kronecker/Khatri-Rao products. For example, the matrix $\mathbf{B}^{(n)} \in \mathbb{R}^{I_n \times \check{I}_n}$ having a Kronecker structure in (4) is huge for large-scale problems. This makes the ALS methods quite time and memory consuming, and therefore not suitable for large-scale data.

3. Constrained Tucker decomposition using Multiway BSS

3.1. Motivation. The Tucker decomposition attempts to give optimal low-rank $(\{J_1, J_2, \ldots, J_N\})$ approximations of the original data. However, quite different from the matrix case, the optimal low-rank approximation may not exist at all or, if it exists, may not be unique for high-order tensors [7, 18–20]. Particularly, unconstrained Tucker decompositions are always non-unique since

$$\begin{aligned} \underline{\mathbf{Y}} &\approx \underline{\mathbf{G}} \times_1 \mathbf{A}^{(1)} \times_2 \mathbf{A}^{(2)} \cdots \times_N \mathbf{A}^{(N)} \\ &= [\underline{\mathbf{G}} \times_1 \mathbf{Q}^{(1)\dagger} \times_2 \mathbf{Q}^{(2)\dagger} \cdots \times_N \mathbf{Q}^{(N)\dagger}] \\ &\quad \times_1 (\mathbf{A}^{(1)}\mathbf{Q}^{(1)}) \cdots \times_N (\mathbf{A}^{(N)}\mathbf{Q}^{(N)}), \end{aligned} \tag{7}$$

where $\mathbf{Q}^{(n)} \in \mathbb{R}^{J_n \times J_n}$ is any nonsingular matrix. So the component matrices in unconstrained Tucker decompositions are with many degrees of freedom and usually have no specific physical meaning or interpretation.

Based on these facts, it is reasonable to consider constrained tensor decompositions, which achieves not necessarily the best fit but the most meaningful and featured components instead. Generally, a constrained Tucker decomposition problem can be formulated as minimization of the cost function:

$$\begin{aligned} &D_F\left(\underline{\mathbf{Y}} \| \widehat{\underline{\mathbf{Y}}}\right) = \\ &\|\underline{\mathbf{Y}} - \underline{\mathbf{G}} \times_1 \mathbf{A}^{(1)} \times_2 \mathbf{A}^{(2)} \cdots \times_N \mathbf{A}^{(N)}\|_F^2 \\ &\quad + \sum_{n=1}^{N} \alpha_n H_n(\mathbf{A}^{(n)}), \end{aligned} \tag{8}$$

where $\|\underline{\mathbf{Y}}\|_F = (\sum_{i_1=1}^{I_1} \cdots \sum_{i_N=1}^{I_N} y_{i_1 \cdots i_N}^2)^{1/2}$, $\alpha_n \geq 0$ are penalty coefficients and $H_n(\mathbf{A}^{(n)})$ are penalty terms which are added to achieve specific properties of the components. For example, if we need to impose mutual independence constraints the penalty terms can take the form $H_n(\mathbf{A}^{(n)}) = \sum_{j=1}^{J_n} \sum_{p \neq j} \mathbf{a}_p^{(n)T} \phi_n(\mathbf{a}_j^{(n)})$, where $\phi_n(x)$ are suitable nonlinear functions.

In principle, model (8) leads to a penalized or constrained ALS algorithms which allows us to find component matrices $\mathbf{A}^{(n)}$ and the associated core tensor $\underline{\mathbf{G}}$, as the ALS algorithms are considered as basic "workhorses" for tensor decompositions. However, as mentioned above, ALS iteration based algorithms have high computational complexity, and due to constraints, they may suffer often from slow convergence. For example, existing nonnegative Tucker decomposition methods often converge very slowly. Particularly, even if we optimize (8) in a global way, the ALS algorithms may stuck in local minima due to noncovexity of cost functions.

3.2. Multiway BSS. In this section, we investigate a simpler yet much more efficient and flexible approach by exploiting separately each mode-n unfolding matrix $\mathbf{Y}_{(n)}$ of

the data tensor $\underline{\mathbf{Y}}$, according to the Tucker-1 decompositions (3), which allows us to directly apply suitable constrained matrix factorization methods to Tucker decompositions. Let $\underline{\mathbf{Y}} \approx [\![\underline{\mathbf{G}}; \mathbf{A}^{(1)}, \mathbf{A}^{(2)}, \ldots, \mathbf{A}^{(N)}]\!]$. We have

$$\mathbf{Y}_{(n)} \approx \mathbf{A}^{(n)} \mathbf{B}^{(n)T}, \qquad (n = 1, 2, \ldots, N), \tag{9}$$

where the mixing matrices have a special Kronecker structure $\mathbf{B}^{(n)} = [\mathbf{G}_{(n)}^{(-n)}]^T$ defined by (4).

From (9), we note that the columns of the mode-n matricization of $\underline{\mathbf{Y}}$ are just linear mixtures of the columns of $\mathbf{A}^{(n)}$, $(n = 1, 2, \ldots, N)$. This suggests that we can use various BSS algorithms to directly extract the component matrices with specific properties and diversities, without consideration of the special Kronecker structure of the basis matrices $\mathbf{B}^{(n)}$ due to the essential uniqueness of BSS.

Assume that the component matrices of interest can be separated by a standard BSS algorithm with unavoidable scaling and permutation ambiguities:

$$\widehat{\mathbf{A}}^{(n)} = \Psi_n(\mathbf{Y}_{(n)}) = \Psi_n(\mathbf{A}^{(n)} \mathbf{B}^{(n)T}) = \mathbf{A}^{(n)} \mathbf{P}_n \mathbf{D}_n, \quad (n = 1, 2, \ldots, N), \tag{10}$$

where Ψ_n denotes symbolically a specific BSS method, the subindex n indicates the fact that for each mode different method and criteria can be employed, and for each mode we have different scaling $\mathbf{D}_n$ and permutation $\mathbf{P}_n$ ambiguity. From (10), for each mode different constraints can be imposed depending on the expected or known physical properties of the components. This is also one major difference between MBSS and the existing multilinear ICA algorithms where only ICA criteria are considered.

We have two basic ways to implement constrained Tucker decomposition in practice:

Independent Extraction of Factor Matrices. In this case each component matrix $\mathbf{A}^{(n)}$ is estimated from the mode-n matricization of $\underline{\mathbf{Y}}$ independently and separately by using (10). Once all desired component matrices $\mathbf{A}^{(n)}$ $(n = 1, 2, \ldots, N)$ have been estimated, the core tensor can be computed, for example, from:

$$\widehat{\underline{\mathbf{G}}} = \underline{\mathbf{Y}} \times_1 \mathbf{A}^{(1)\dagger} \times_2 \mathbf{A}^{(2)\dagger} \cdots \times_N \mathbf{A}^{(N)\dagger}. \tag{11}$$

Alternatively, we can apply multiplicative update formula proposed in [5, 16], e.g., if we wish to impose nonnegativity constraints on the components and the core tensor[5].

Sometimes only partial pre-specified factors, say $\mathbf{A}^{(K)}$, $K < N$, can be extracted by using BSS. For the Tucker decomposition, the remainder component matrices and the core tensor can be obtained, e.g., by using ordinary ALS iteration based methods, such as HOOI [7, 32]. In most cases, however, the remainder component matrices are simply of no interest because they do not carry any important information, or the information they carry can be simply absorbed into the core tensor. This often leads to a partial Tucker decomposition. Without loss of generality, let us assume that we are interested in extracting only the first K, with $K \leq N$ component matrices. In such a case, we can use a simplified Tucker-K model described as

$$\underline{\mathbf{Y}} = \breve{\underline{\mathbf{G}}} \times_1 \mathbf{A}^{(1)} \times_2 \mathbf{A}^{(2)} \cdots \times_K \mathbf{A}^{(K)} + \underline{\mathbf{E}}, \tag{12}$$

where the partial core tensor $\breve{\underline{\mathbf{G}}} \in \mathbb{R}^{J_1 \cdots \times J_K \times I_{K+1} \cdots \times I_N}$ is expressed as

$$\breve{\underline{\mathbf{G}}} = \underline{\mathbf{G}} \times_{K+1} \mathbf{A}^{(K+1)} \times_{K+2} \mathbf{A}^{(K+2)} \cdots \times_N \mathbf{A}^{(N)}. \tag{13}$$

Note that the Tucker-K model (12) can be represented equivalently by a set of K different matrix factorizations with three factors:

$$\mathbf{Y}_{(k)} \approx \mathbf{A}^{(k)} \breve{\mathbf{G}}_{(k)} \mathbf{Z}^{(k)}, \qquad (k = 1, 2, \ldots, K), \tag{14}$$

where $\mathbf{Z}^{(k)} = \left[\mathbf{A}^{(K)} \otimes \cdots \otimes \mathbf{A}^{(k+1)} \otimes \mathbf{A}^{(k-1)} \cdots \otimes \mathbf{A}^{(1)}\right]^T$. Again, $\mathbf{A}^{(k)}$ can be extracted by using proper BSS methods due to the linearity of (14). Finally, $\widehat{\underline{\mathbf{G}}}$ can be computed from

$$\widehat{\breve{\underline{\mathbf{G}}}} = \underline{\mathbf{Y}} \times_1 \mathbf{A}^{(1)\dagger} \times_2 \mathbf{A}^{(2)\dagger} \cdots \times_K \mathbf{A}^{(K)\dagger} \tag{15}$$

or some other proper methods. This procedure is illustrated in the rightmost diagram of Fig. 2.

Sequential extraction and update of factor matrices. In this case, after $\mathbf{A}^{(n)}$ has been estimated by using (10), then the observation tensor $\underline{\mathbf{Y}}$ can be updated (reduced) as

$$\underline{\mathbf{Y}} \leftarrow \underline{\mathbf{Y}} \times_n \mathbf{A}^{(n)\dagger}. \tag{16}$$

After update, the size of new data $\underline{\mathbf{Y}}$ can be significantly reduced taking into account that $J_n \ll I_n$. For large-scale problems this can reduce the total computational complexity. After all component matrices have been estimated, we let $\underline{\mathbf{G}} = \underline{\mathbf{Y}}$. This way is often more efficient than the *Independent Extraction* approach if the order of data tensor is not very high. However, we have to carefully chose the BSS methods in this approach, because, first of all, current poor separation accuracy may deteriorate the subsequent separation accuracy. Second, the order of selection of modes should be carefully considered according to the constraints and the dimensionality of factor matrices. For example, it is suggested to estimate first nonnegative components since many standard BSS algorithms may often destroy the nonnegativity. Otherwise, the mode with the highest dimensionality may be considered first as it can reduce the data tensor $\underline{\mathbf{Y}}$ most significantly. See Fig. 2 (middle of the figure) for the diagram illustrating this approach.

[5] Since core tensors can be represented in unfolded form via matrix factorizations (see e.g., Eq. 14), we can apply any suitable BSS method to estimate constrained core tensors (e.g., NMF, SCA, ICA) with a little sacrifice in fit.

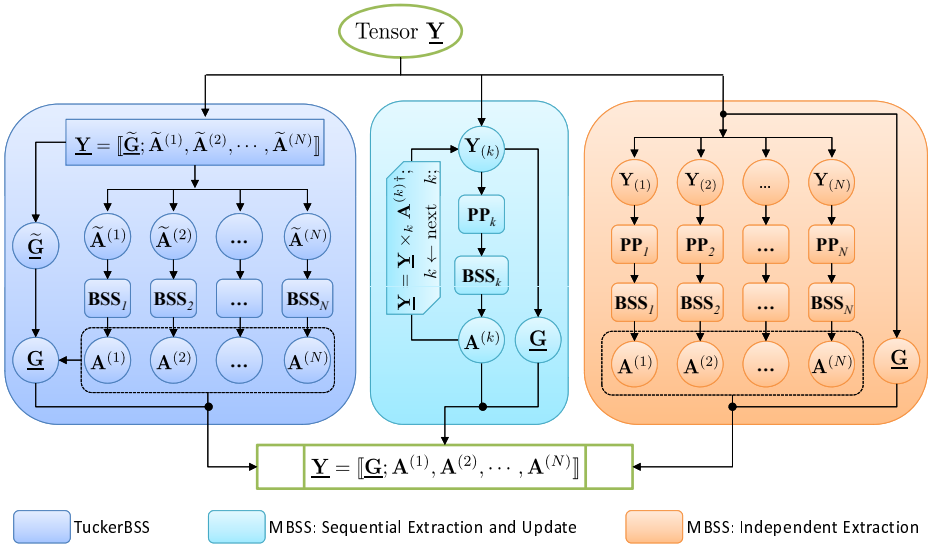

Fig. 2. TuckerBSS versus MBSS. Here, PP_n and BSS_n denote the pre-processing procedure and the BSS method for mode-n, respectively, $(n = 1, 2, \cdots, N)$. Theoretically all the three approaches for noiseless data should give the same results but MBSS methods are more efficient and flexible

The methods described above are referred to as multiway blind source separation (MBSS) since multiple sets of signals with specific physical meaning are extracted from different modes of the data tensor by using BSS methods, based on the multilinear structures of Tucker model. The name MBSS is used to emphasize its difference from ordinary unconstrained Tucker decompositions.

It is worth noticing that there are two possible interpretations of the results using constrained Tucker decompositions for the MBSS. In the first approach the columns of component matrices $\mathbf{A}^{(n)}$ represent the desired components or latent variables, and the core tensor represents a kind of "mixing process". More precisely, the core tensor shows the links among the components from different modes, while the data tensor $\underline{\mathbf{Y}}$ represents a collection of multidimensional mixing signals. In the second approach, the core tensor represents the desired but unknown (hidden) N-dimensional signal (e.g., 3D MRI image or 4D video) and the component matrices represent specific dictionaries or transformations, e.g., time frequency transformations or wavelets dictionaries (mixing or filtering processes). In this case the data tensor $\underline{\mathbf{Y}}$ represents the observed N-dimensional signal, which may be distorted, transformed, compressed or mixed, depending on the specific applications. In this paper we only consider the first interpretation or approach.

Remark. The similar approach can be applied for constrained Candecomp/PARAFAC (CP) model, especially when components are highly collinear or problem is very ill conditioned or sample number in some modes are very small. However, for the CP model we need only to perform unfolding in a single (one) mode and apply a suitable standard BSS (e.g., ICA, NMF or SCA). On basis of the components in this mode we can compute uniquely components in all other models using SVD. Details can be found in our separate paper [33].

3.3. Identifiability conditions and uniqueness of MBSS.

Note that the separability of the MBSS depends on two conditions: full column rank of each mixing matrix $\mathbf{B}^{(n)}$ and suitable assumptions on the component matrices $\mathbf{A}^{(n)}$, for example, assuming that the components in specific modes are statistically independent, or nonnegative and/or sparse. These assumptions are generally application-dependent and are based on some *a priori* knowledge of expected features of $\mathbf{A}^{(n)}$. Here, we always assume that this *a priori* knowledge is available in order to choose suitable BSS algorithms and criteria[6].

For the constrained Tucker decompositions, we have the following proposition:

Proposition 3. If the elements of $\mathbf{A}^{(n)}$ and $\underline{\mathbf{G}}$ are drawn from independent Gaussian distributions, and $\min(\check{I}_n, \check{J}_n) \geq J_n$, then $\mathbf{B}^{(n)}$ given by (4) is of full column rank with probability one.

Proof. First $\text{rank}(\mathbf{G}_{(n)}) = J_n$ and $\text{rank}(\mathbf{A}^{(n)}) = \min(I_n, J_n)$, $n = 1, 2, \ldots, N$, hold with probability one [34]. Thus the matrix $\mathbf{G}_{(n)}$ is of full column rank with probability one. Moreover, $\text{rank}(\bigotimes_{p \neq n} \mathbf{A}^{(p)}) = \Pi_{p \neq n} \text{rank}(\mathbf{A}^{(p)})$. It can be easily verified that $\det(\mathbf{B}^{(n)T}\mathbf{B}^{(n)})$ is not identical to zero. The set satisfying $\det(\mathbf{B}^{(n)T}\mathbf{B}^{(n)}) = 0$ is therefore Lebesgue measure zero [35] (Theorem 5 A.2). In other words, $\mathbf{B}^{(n)}$ is of full column rank with probability one. This ends the proof.

[6]For example, components in the frequency domain are usually nonnegative and smooth, while spatial components are usually sparse and temporal components are often mutually independent.

3.4. MBSS versus Tucker BSS. As a matter of fact, many authors have considered imposing constraints on the factor matrices to retrieve meaningful factors [21–24, 36]. For example, Beckamnn and Smith [21], and De Vos *et al*. [22] combined the CP model and ICA. Unkel *et al*. [24] proposed adding ICA algorithms to the Tucker-3 model and this method can be referred to as Tucker-ICA. However, MBSS allows us imposing various constraints in each mode. There is neither a theoretical nor experimental basis for the idea that statistical independence (ICA) is the uniquely correct concept to extract latent hidden components [37, 38]. In real world scenarios, latent (hidden) components may have various statistical properties and features. We often need to apply a fusion of strategies by employing several suitably chosen criteria and the associated learning algorithms to extract all desired components in specific modes [5, 6, 38]. Therefore, if instead the ICA alternative BSS algorithms are adopted, this two-step approach can be referred to as the TuckerBSS method. Figure 2 depicts the basic scheme of TuckerBSS. TuckerBSS looks quite intuitive, simple, and often gives meaningful results.

In the following we explain why we propose MBSS in more details. First of all, MBSS theoretically gives the consistent results with TuckerBSS in the ideal noiseless case, however it is usually more robust for noisy data.

Proposition 4. Suppose that we have two exact Tucker decompositions $\underline{\mathbf{Y}} = [\![\underline{\mathbf{G}}; \mathbf{A}^{(1)}, \mathbf{A}^{(2)}, \ldots, \mathbf{A}^{(N)}]\!]$ and $\underline{\mathbf{Y}} = [\![\underline{\mathbf{H}}; \mathbf{X}^{(1)}, \mathbf{X}^{(2)}, \ldots, \mathbf{X}^{(N)}]\!]$ for the same tensor $\underline{\mathbf{Y}}$, obtained by an arbitrary Tucker decomposition algorithm, and $\text{rank}(\mathbf{A}^{(n)}) = \text{rank}(\mathbf{Y}_{(n)}) = J_n$. Then there holds that $\mathbf{X}^{(n)} = \mathbf{A}^{(n)}\mathbf{Q}^{(n)}$, where $\mathbf{Q}^{(n)} \in \mathbb{R}^{J_n \times J_n}$ is an invertible matrix, $(n = 1, 2, \ldots, N)$.

The proof is straightforward and is omitted here. Proposition 4 means that the Tucker decomposition just gives a linear mixture (i.e., the range) of $\mathbf{A}^{(n)}$. Indeed, any linear mixture of the columns of $\mathbf{A}^{(n)}$ is a solution. To retrieve the unique component matrices from their linear mixtures, the two-step TuckerBSS method applies specific BSS algorithms to the component matrices obtained by unconstrained Tucker decompositions:

$$\widehat{\mathbf{A}}^{(n)} = \Psi_n(\mathbf{X}^{(n)}) = \Psi_n(\mathbf{A}^{(n)}\mathbf{Q}^{(n)}) = \mathbf{A}^{(n)}\mathbf{P}_n\mathbf{D}_n, \quad (n = 1, 2, \ldots, N). \tag{17}$$

By using the MBSS approach, however, these constrained component matrices can be extracted directly from the unfolded matrices $\mathbf{Y}_{(n)}$, as $\mathbf{Y}_{(n)}$ itself is assumed to be a linear mixture of the columns of $\mathbf{A}^{(n)}$. In other words, the source separation and the unique Tucker decomposition can be performed simultaneously, see (10) and (17) for a comparison. Note also that the results are just the same as those obtained via TuckerBSS, because the separation results of BSS are independent of the mixing matrix $\mathbf{B}^{(n)}$ if it is full rank. In other words, although both MBSS and TuckerBSS are able to give unique, meaningful, and essentially consistent components, in MBSS the additional unconstrained Tucker decomposition is simply unnecessary.

In the following we summarize the advantages of MBSS versus TuckerBSS.

1. **Considerable flexibility and robustness**. In MBSS, any existing matrix factorization methods can be employed directly. Furthermore, various pre-processing procedures such as dimensionality reduction, source number estimation developed for matrices can be easily and straightforwardly incorporated, which can significantly improve the efficiency and performance of MBSS. However, in the TuckerBSS we have to carefully design different Tucker algorithms to adapt to different situations. Typically, most existing Tucker decomposition methods have assumed the noises are drawn from independent Gaussian distributions. However, if the noises are, e.g., very sparse and of very high amplitude, they lead to very high approximation error and thus TuckerBSS will achieve very low separation accuracy. In the MBSS, however, we can simply use, e.g., robust PCA proposed in [39] to remove the sparse noise and then extract the latent signals. This feature of MBSS will be illustrated in Simulation 2.
2. **High efficiency and simplicity**. In ALS based methods we have to unfold the tensor and perform matrix-matrix (Kronecker/Khatri-Rao) products frequently. These operations are often time and memory consuming, which severely hinders their applicability, especially for large-scale and noisy data. In the MBSS, we unfold the data tensor in each mode only once. Moreover, we do not need to consider the Kronecker/Khatri-Rao structure of $\mathbf{B}^{(n)}$ in (4) and (10) explicitly due to the essential uniqueness of BSS. This will significantly reduce the computational complexity. Moreover, as we will see later, by incorporating state of the art dimensionality reduction methods, the efficiency of MBSS can be further substantially improved. This feature will be illustrated by extensive simulations in Sec. 5.

Another subtle difference between MBSS and TuckerBSS is that in TuckerBSS the minimum fitting error is pursued first and then the feature information of the components is maximized, whereas in MBSS the feature information is maximized based on the multilinear structure and the feature information directs the components to the desired one. As pure pursuit of minimum fitting error has theoretical limitation [18], and existing Tucker decomposition methods have implicitly or explicitly assumed the noises are Gaussian, MBSS can be more flexible and practicable for real data analysis.

One may argue that MBSS is simply ordinary BSS. It is the truth if we only consider one mode[7]. However, we usually have to extract several factors from the data in different. These multiple factors are linked or associated via the core tensor, see (1), and provide extra information and facilities in data exploration, interpretation, projection, and transformation,

[7]Also, if we look only in one mode, tensor decomposition is simply ordinary constrained matrix factorization, by using matricization. The key point is that in tensor decomposition multiple factors from multiple modes are involved, and links between them are established.

etc. In summary, in MBSS the high-way data is explained and interpreted by a Tucker structure but this structure is realized by using ordinary BSS methods. The MBSS benefits from its delicate and comprehensive multilinear structures compared with ordinary BSS. Moreover, it provides more interpretable components with physical meanings, compared with unconstrained tensor decompositions.

4. Dimensionality reduction and estimation of the number of components

In this section we discuss two important pre-processing procedures, that is, dimensionality reduction and estimation of the number of components. The matrices $\mathbf{Y}_{(n)}$ and $\mathbf{B}^{(n)}$ have the large sizes of $I_n \times \breve{I}_{(n)}$ and $\breve{I}_{(n)} \times J_n$, respectively, typically with $\breve{I}_n \gg J_n$. Therefore, problems we encounter here are usually large-scale, highly over-determined and thus could be challenge in practice. To reduce the computational complexity, the dimensionality reduction step should be performed first. Moreover, the adaptive estimation of the number of components J_n in each specific mode of interest is another important issue. Note that at first, we have assumed that the noises are Gaussian, which is the standard assumption for most tensor decomposition methods. After that we will briefly discuss how to deal with the cases when have different non-Gaussian distributions.

In order to perform dimensionality reduction, we can apply standard PCA (e.g., using truncated SVD) to each unfolding matrix $\mathbf{Y}_{(n)}$. In more detail, we perform eigenvalue decompositions $\mathbf{Y}_{(n)}\mathbf{Y}_{(n)}^T = \mathbf{U}_{J_n}\mathbf{\Lambda}\mathbf{U}_{J_n}^T$ first (supposing that $\breve{I}_n > I_n$), where $\mathbf{U}_{J_n}$ consists of the first J_n leading eigenvectors. Then, we run BSS on the dimensionality reduced matrix $\mathbf{U}_{J_n}^T$ directly[8]. This way involves the eigenvalue decomposition of an $I_n \times I_n$ matrix, and gives the optimal low-rank approximation of the observations, in the sense of least square. Therefore, PCA is preferred for some ordinary BSS tasks if the scale of the problem is moderate. However, it suffers from a heavy computation load and huge memory use for large-scale problems, i.e., both $\breve{I}_n$ and I_n are very large [40]. Moreover, PCA/SVD will not preserve nonnegativity constraints, thus it is not directly suitable for the cases in which nonnegative components are desired.

Note that each column of $\mathbf{Y}_{(n)}$, namely $\mathbf{y}_{(n)}$, is exactly a linear combination of the columns of $\mathbf{A}^{(n)}$. Thus, we can estimate $\mathbf{A}^{(n)}$ from a new observation matrix whose columns are sampled from the columns of $\mathbf{Y}_{(n)}$ since BSS is generally independent of the specific mixing matrix. By thus, the dimensionality of observations can be significantly reduced, and the nonnegativity can be preserved. In ideal noise free case, even only J_n columns would be sufficient to estimate $\mathbf{A}^{(n)}$. In general, we want to use as small as possible number of columns to approximate the original huge observation matrix, then run BSS on the significantly reduced observation matrix. The CUR method presented in [41] confirms that a huge matrix can be approximated by suitably sampling its columns and/or rows. Based on this, we can run BSS on the sampled columns of $\mathbf{Y}_{(n)}$ without accessing the whole tensor[9]. By using this approach the computational efficiency can be significantly improved and the use of memory can be reduced as well.

Another important fact is that the columns of $\mathbf{Y}_{(n)}$ are simply built up from the mode-n fibers[10] of $\underline{\mathbf{Y}}$. Using MATLAB notations, the mode-n fibers of an N-way tensor $\underline{\mathbf{Y}}$ are denoted as $\mathbf{y}_{i_1 i_2 \cdots i_{n-1}, :, i_{n+1} \cdots i_N}$, or in short, $\mathbf{y}_{(n)}$ [32]. In the MATLAB environment, thanks to the support for multi-dimensional arrays, we can access and sample the fibers directly from the tensor, and the sampled fibers form a reduced observation matrix, say $\widetilde{\mathbf{Y}}_{(n)}$, without the need to explicitly construct the full unfolding matrix $\mathbf{Y}_{(n)}$ in advance. Consequently, the sampling procedure can be very efficient and it is very similar to the Fiber Sampling Tensor Decomposition (FSTD) method [42], which is a generalization of CUR decomposition for tensors (see Fig. 3). The FSTD is based on the following theoretical results [42]:

$$\underline{\mathbf{Y}} \approx \widetilde{\underline{\mathbf{G}}} \times_1 \widetilde{\mathbf{Y}}_{(1)} \times_2 \widetilde{\mathbf{Y}}_{(2)} \cdots \times_N \widetilde{\mathbf{Y}}_{(N)}, \tag{18}$$

where $\widetilde{\mathbf{Y}}_{(n)} \in \mathbb{R}^{I_n \times J_{r_n}}$ are matrices consisting of mode-n fibers sampled from the data tensor $\underline{\mathbf{Y}}$ directly, $I_n \gg J_{r_n} \geq J_n$. The value of J_{r_n} depends on the level of noise and in practice it is often sufficient that $J_{r_n} \geq 5J_n$ [5]. It should be noted that each column of $\widetilde{\mathbf{Y}}_{(n)}$ is a linear combination of the columns of $\mathbf{A}^{(n)}$. Hence, we can directly apply the FSTD procedure in the MBSS, i.e., run BSS on $\widetilde{\mathbf{Y}}_{(n)}$ and retrieve $\mathbf{A}^{(n)}$ from the linear mixtures $\widetilde{\mathbf{Y}}_{(n)}$, as illustrated in Fig. 3. However, in our MBSS approach there are some major simplifications and modification with comparison to the original FSTD:

- The computation of the core tensor $\widetilde{\underline{\mathbf{G}}}$ is unnecessary, since it is not essential for the estimation of $\mathbf{A}^{(n)}$, $n = 1, 2, \ldots, N$.
- We do not need to sample all the modes simultaneously. Instead we sample each mode sequentially and independently.
- The numbers of components, i.e., J_n, are usually unknown in practice. In such case we need to determine the value of J_n (and thus J_{r_n}).

[8] If occasionally $I_n > \breve{I}_n$, the eigenvalue decomposition of $\mathbf{Y}_{(n)}^T\mathbf{Y}_{(n)} = \mathbf{V}_{J_n}\mathbf{\Sigma}\mathbf{\Lambda}_{J_n}^T$ should be computed instead. Then we apply a suitable BSS method for low-rank approximation matrix $\mathbf{V}_{J_n}^T\mathbf{Y}_{(n)}^T$.

[9] This sampling procedure only reduces the redundant mixed (observed) signals without destroying any property (e.g., temporal property) of source signals. Therefore, we can run BSS methods on the sampled mixtures to estimate the sources.

[10] A *fiber* of a tensor $\underline{\mathbf{Y}}$ is a vector defined by fixing every subscript of $\underline{\mathbf{Y}}$ but one.

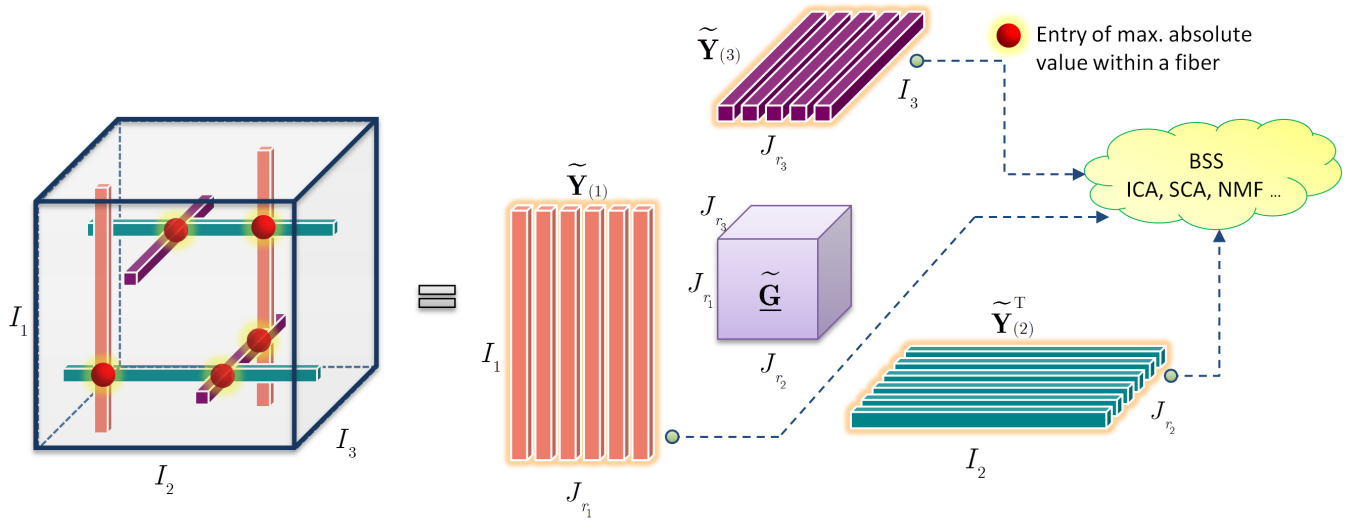

Fig. 3. Illustration of FSTD and MBSS based on fiber sampling of a 3D tensor. Note that on one hand, the columns of $\widetilde{\mathbf{Y}}_{(n)}$ are sampled from the fibers of the original data tensor $\underline{\mathbf{Y}}$; on the other hand, these columns/fibers are the linear combinations of the columns of factors $\mathbf{A}^{(n)}$. Thus we can run various BSS algorithms (optionally, with PCA) on the sampled fibers directly to extract $\mathbf{A}^{(n)}$

Now, we will discuss how to determine the number of fibers to be sampled. Assume that the additive noises are drawn from independent Gaussian distributions with zero mean, and a total of J_{r_n} fibers are sampled and stored in $\widetilde{\mathbf{Y}}_{(n)}$. Let $\widetilde{\mathbf{Y}}_{(n)}^T\widetilde{\mathbf{Y}}_{(n)} = \mathbf{V}\mathbf{\Lambda}\mathbf{V}^T$ be the eigenvalue decomposition of $\widetilde{\mathbf{Y}}_{(n)}^T\widetilde{\mathbf{Y}}_{(n)}$ with the eigenvalues $\lambda_i,\ i = 1, 2, \cdots, J_{r_n}$. It is well known that $\widehat{\lambda}_i = \lambda_i + \sigma_\varepsilon^2$ for $i = 1, 2, \cdots, J_n$, and $\widehat{\lambda}_i = \sigma_\varepsilon^2$ for $i > J_n$, where λ_i corresponds to the signal space and σ_ε^2 measures the level of noise. Without loss of generality, assume that [9]

$$\widehat{\lambda}_1 \geq \widehat{\lambda}_2 \cdots \geq \widehat{\lambda}_{J_n} > \widehat{\lambda}_{J_n+1} \approx \cdots \approx \widehat{\lambda}_{J_{r_n}} \approx \sigma_\varepsilon^2. \tag{19}$$

Intuitively, to estimate the number of components, i.e., J_n, we only need to locate the GAP (jump) between the eigenvalues corresponding to the signal space (with noise) and the pure noise space. Based on (19), a so-called Second ORder sTatistic of the Eigenvalues (SORTE) method is developed to locate this GAP [9]. Let $\nabla\widehat{\lambda}_i = \widehat{\lambda}_i - \widehat{\lambda}_{i+1}$ denote the difference of neighbor eigenvalues and $\widehat{\sigma}_p^2$ be the variance of $\{\nabla\widehat{\lambda}_i :\ i = p, p+1, \cdots, J_{r_n} - 1\}$. That is,

$$\begin{aligned}\widehat{\sigma}_p^2 &= \mathrm{var}\left[\{\nabla\widehat{\lambda}_i\}_{i=p}^{J_{r_n}-1}\right] \\ &= \frac{1}{J_{r_n}-p}\sum_{i=p}^{J_{r_n}-1}\left[\nabla\widehat{\lambda}_i - \frac{1}{J_{r_n}-p}\sum_{i=p}^{J_{r_n}-1}\nabla\widehat{\lambda}_i\right]^2.\end{aligned} \tag{20}$$

The SORTE method estimates the number of components, i.e., J_n, by locating the maximal GAP between the eigenvalues of $\widehat{\lambda}_i$ as follows:

$$\begin{aligned}J_n = \arg\min_p \mathrm{GAP}(p) = \arg\min_p \frac{\widehat{\sigma}_{p+1}^2}{\widehat{\sigma}_p^2}, \\ p = 1, 2, \ldots, J_{r_n} - 3.\end{aligned} \tag{21}$$

The SORTE implicitly depends on a reliable and stable estimation of the eigenvalues of the covariance matrix, which means that the number of samples should be sufficiently large. Therefore, we keep sampling the columns of $\mathbf{Y}_{(n)}$ until a satisfactory estimate of $\widehat{\lambda}_i$, i.e., a stable estimate of J_n, is reached, as demonstrated by Fig. 4. In Fig. 4 the data (observation) matrix $\mathbf{Y} \in \mathbb{R}^{100\times 1000}$ with rank 10 is contaminated by white Gaussian noise with SNR=20dB, r is the rank estimated by SORTE from the J_r sampled columns, and ρ is defined as

$$\rho = \frac{Err_s - Err^*}{\|\mathbf{Y}\|_F}, \tag{22}$$

where Err_s is the best rank-r approximation error by running PCA on the J_r sampled columns, whereas Err^* is the optimal rank-r fitting error achieved by PCA using the matrix $\mathbf{Y}$. From Fig. 4, with the sampled columns J_r increasing, the number of components r estimated by SORTE increases and fluctuates at first. However, after $J_r \geq 20$, r does not increase any more. Moreover, the approximation is gradually closer to the optimal low-rank approximation. Thus, the number of components is estimated, and at the same time, the observation matrix is approximated by a much smaller submatrix $\widetilde{\mathbf{Y}}$. In the next section simulations will show that this sampling procedure achieves a good tradeoff between efficiency and accuracy. Based on above analysis, a fast Fiber Sampling-based SORTE (FSSORTE) method is proposed and implemented to perform estimation of the number of components and dimensionality reduction, see Algorithm 4 for details. (In the algorithm, freq(r_n) computes the frequency of occurrence of r_n).

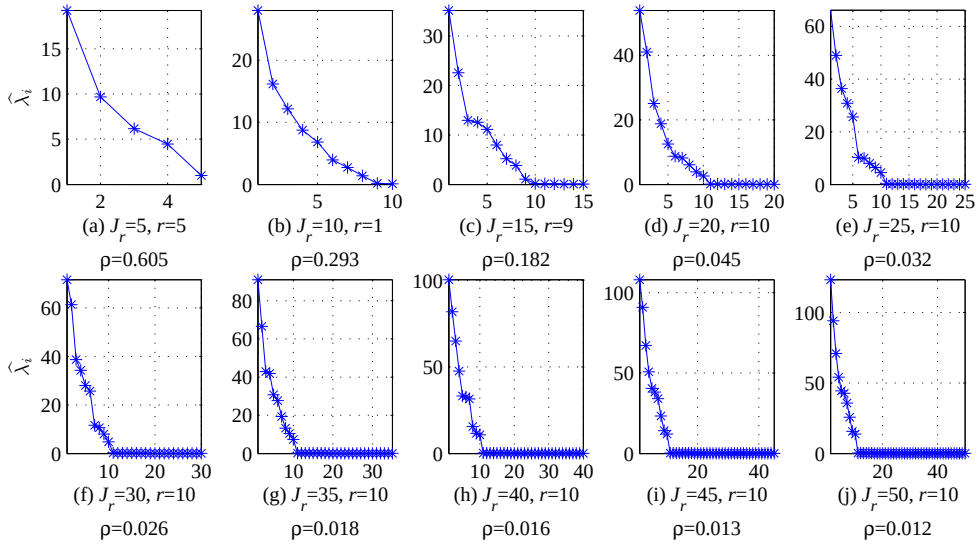

Fig. 4. Illustration of adaptive low-rank approximation and rank detection by random sampling-based SORTE. The rank r is the rank estimated from the J_r sampled columns by using SORTE, and ρ is defined by (22)

Algorithm 1: Fiber sampling-based SORTE for dimensionality reduction and rank detection (FSSORTE)

Input: $\mathbf{Y}_{(n)} \in \mathbb{R}^{I_n \times \breve{I}_n}$, $(n = 1, 2, \ldots, N)$.
Output: $J_n = r_n$ and $\widetilde{\mathbf{Y}}_{(n)} \in \mathbb{R}^{I_n \times J_n}$ (or $\widetilde{\mathbf{Y}}_{(n)} \in \mathbb{R}^{I_n \times t}$ for NMF).
for $t = 1, 2, \cdots$, **do**
  $\widetilde{\mathbf{Y}}_{(n)}(:, t) = \mathbf{y}_{(n)}^{(t)}$, where $\mathbf{y}_{(n)}^{(t)}$ is a randomly sampled mode-n fiber and $\|\mathbf{y}_{(n)}^{(t)}\| > \varepsilon$;
  if mode$(t, p_0) = 0$ **then**
    $\widehat{\lambda}_t \leftarrow$ eigenvalues of $\widetilde{\mathbf{Y}}_{(n)}^T \widetilde{\mathbf{Y}}_{(n)}$;
    $r_n = \text{SORTE}(\widehat{\lambda}_t)$;
    if freq$(r_n) > \gamma$ and $t > p \times r_n$ **then**
      Output $\widetilde{\mathbf{Y}}_{(n)}$ if nonnegativity is required; otherwise output $\widetilde{\mathbf{Y}}_{(n)} = \widetilde{\mathbf{Y}}_{(n)} \mathbf{V}_{r_n}$, where $\mathbf{V}_{r_n}$ is the r_n eigenvectors corresponding to the r_n largest eigenvalues of $\widetilde{\mathbf{Y}}_{(n)}^T \widetilde{\mathbf{Y}}_{(n)}$.
      break;
    end if
  end if
end for

In the FSTD method the entries with larger absolute values dominate the sampling procedure. In our case random uniform sampling is utilized instead but with the restriction that $\|\mathbf{y}_{(n)}^{(t)}\| > \epsilon$. In the case where the number of components is known, we can simply terminate FSSORTE if $J_{r_n} > pJ_k$, and $p \geq 5$ is an empirically-based choice [5]. FSSORTE outputs the optimal number of components $r_n = J_k$ and the significantly reduced matrix $\widetilde{\mathbf{Y}}_{(n)}$. Compared with standard PCA, Algorithm 1 performs eigenvalue decomposition of a series of $J_{r_n} \times J_{r_n}$ matrices. Considering that the number of latent sources of the high dimensional data is relatively small with $J_n \leq J_{r_n} \ll I_n$, Algorithm 1 is more efficient than standard PCA. Note that the projection $\widetilde{\mathbf{Y}}_{(n)} \mathbf{V}_{r_n}$ actually gives a random approximation of PCA and it can be used for ordinary BSS algorithms. However, if the original tensor is nonnegative and we want to run NMF to estimate the component matrices, we generally use the sampled fibers $\widetilde{\mathbf{Y}}_{(n)}$ directly without projection.

It is worth noticing that in the above analysis the noises have been assumed to be Gaussian. Under this consumption, some methods to estimate the number of components has been proposed for three way tensors, see, e.g., [43, 44]. On the other hand, some alternative methods have been proposed to estimate the latent components in the matrix case [45]. Apparently, the proposed approach enables us to employ all these methods freely and avoid extensively repeating these work which has been done for matrices.

If the noise is not Gaussian, we need to apply another suitable low-rank approximation methods. For example, if the additive noise is very sparse, we can use the robust PCA (RPCA) proposed in [39] to perform dimensionality reduction and filter out noise. From this point of view, MBSS is actually quite flexible because any well-established matrix factorization methods can be easily incorporated for specific purposes and analysis, instead of re-designing all kinds of new methods for tensors.

5. Simulations

In this section the validity and efficiency of the MBSS is investigated by simulations of synthetic and real data. We use two performance indices (PI) to evaluate the performance. The first one is the signal-to-interference ratio (SIR) which is defined by

$$\text{SIR}(\mathbf{a}, \widehat{\mathbf{a}}) = 10 \log_{10} \frac{\sum_t a_t^2}{\sum_t (a_t - \widehat{a}_t)^2}, \tag{23}$$

where $\mathbf{a}$, $\widehat{\mathbf{a}}$ are normalized with zero mean and unit variance, and $\widehat{\mathbf{a}}$ is an estimate of $\mathbf{a}$. The value of SIR reflects how well

the estimated component (source) matches the true original one. The second PI measures the fit of the estimated tensor to the original raw data tensor and is defined as

$$\text{fit}(\underline{\mathbf{Y}}, \widehat{\underline{\mathbf{Y}}}) = 1 - \frac{\|\underline{\mathbf{Y}} - \widehat{\underline{\mathbf{Y}}}\|_F}{\|\underline{\mathbf{Y}}\|_F}, \tag{24}$$

where $\widehat{\underline{\mathbf{Y}}}$ is an estimate of $\underline{\mathbf{Y}}$. For synthetic data $\underline{\mathbf{Y}}$ denotes the noiseless tensor whereas it denotes the observation data for real data because in this case the latent noiseless data are unknown. Obviously, $\text{fit}(\underline{\mathbf{Y}}, \widehat{\underline{\mathbf{Y}}}) = 1$ if and only if $\widehat{\underline{\mathbf{Y}}} = \underline{\mathbf{Y}}$. All the simulations were done in MATLAB 2008a on a computer with Intel 7i 3.33GHz CPU and 24GB memory running Windows 7.

Simulation 1. In this simulation different constraints were imposed on the components in different modes, that is, temporal (second-order statistics) decorrelation in mode-2 and mode-3 (they were chosen as acsin10d, which is included in the benchmark of ICALAB [46]), and the higher-order statistical independence in mode-1. The elements of $\mathbf{A}^{(1)} \in \mathbb{R}^{500\times 4}$ and the core tensor $\underline{\mathbf{G}} \in \mathbb{R}^{4\times 5\times 5}$ were drawn from independent uniform distributions. Finally, very heavy Gaussian noise with SNR=0dB was added. We used EFICA [47] to extract the first component matrix and the SOBI [48] to extract the two others, respectively. The MBSS approach was compared with the higher-order orthogonal iteration (HOOI) algorithm presented in [32] and the standard ALS, i.e., TuckerALS implemented in the N-way toolbox [49]. Because the ordinary Tucker decompositions are always non-unique, we used EFICA and SOBI to refine the component matrices obtained by HOOI and TuckerALS, which can be viewed as two-step implementations of TuckerBSS, and were denoted as HOOI+BSS and TuckerALS+BSS, respectively. The maximum iteration number was set 100 for HOOI and TuckerALS. The results are shown in Table 1. It can be seen that if all the fibers were employed, MBSS achieved the same separation accuracy as the other two methods. However, MBSS was about two times faster. When $500J_n$ fibers were sampled (denoted by 500x), MBSS was about five times faster than the other methods and achieved satisfactory separation accuracy. This feature makes MBSS very competitive for large-scale problems.

Table 1
Comparison of performances of the MBSS, HOOI+BSS and TuckerALS+BSS for the decomposition of a large tensor with mixed constraints. Very heavy Gaussian noise with SNR=0dB was added. MBSS [500x] used $500J_n$ randomly sampled fibers whereas MBSS [100%] used all the fibers

Algorithm	mSIR_1	mSIR_2	mSIR_3	Runtime(s)	Fit
MBSS [500x]	41	17	25	1.9	0.96
MBSS [100%]	41	18	25	4.1	0.99
HOOI	41	18	24	9.3	0.99
TuckerALS	47	18	25	11	0.99

In some applications the noise may not be Gaussian. For example, in electroencephalography (EEG) signal processing, eye blink artifacts typically are sparse yet have very large amplitude. To simulate this kind of situations, we added sparse noise to the observation tensor $\underline{\mathbf{Y}}$ as follows. We randomly selected 1000 entries from $\underline{\mathbf{Y}}$ and added huge bipolar sparse noise (outliers drawn from Gaussian distribution) with the SNR = -20 dB.

For this corrupted by spiky noise tensor, both HOOI+BSS and TuckerALS+BSS failed to retrieve the latent components, see Fig. 5c and d. In fact they also achieved very low fit to the original tensor, as shown in Table 2. In MBSS, we randomly sampled only $100J_n$ fibers first. Then, we applied the Robust PCA (RPCA) proposed in [39] on the sampled fibers to filter out the sparse outliers noise. Finally, we apply ordinary PCA, SOBI and FastICA algorithms to retrieve hidden factors. The recovered waveforms were plotted in Fig. 5b. It can be seen that the recovered signals match the true sources very well. The mean SIRs, runtime, and fit are detailed in Table 2. In fact, only MBSS was able to extract the desired components with a high accuracy in the presence of outliers. From the simulation results, MBSS is more flexible and versatile as any off-the-shelf matrix factorization methods can be easily incorporated[11]. Figure 6 plots the mean SIRs of $\mathbf{A}^{(1)}$ obtained by MBSS with different configurations over 50 independent runs. The blue crosses mark the results obtained by MBSS [500x] when 0 dB Gaussian noise was involved and the red asterisks denote the MBSS incorporating RPCA when -20 dB sparse noise was involved, which shows that

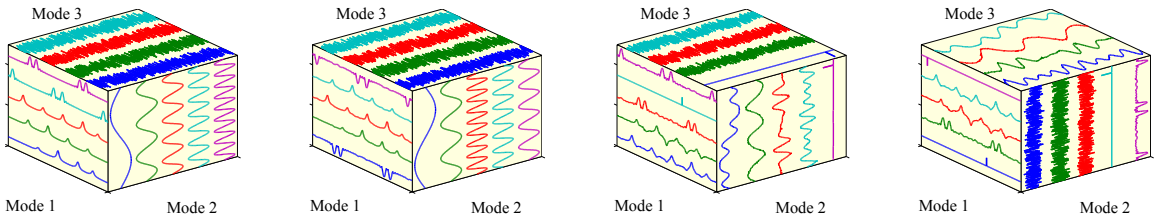

(a) The sources (b) MBSS (c) HOOI+BSS (d) TuckerALS+BSS

Fig. 5. Comparison of performances of the MBSS, HOOI+BSS and TuckerALS+BSS in the decomposition of a tensor with mixed constraints. Very sparse noise with SNR=-20dB was added to the observations tensor. In MBSS we used $100J_n$ randomly sampled fibers and then we preprocessed them by employing RPCA

[11] In this case the improved performance was achieved via suitable preprocessing which was relatively easy to incorporate into the MBSS approach. The implementation of such preprocessing, however, is not so straightforward for other existing methods.

the separation accuracy was quite stable although MBSS only used randomly sampled fibers. By fibers sampling, MBSS can make a good trade-off between the separation accuracy and efficiency. This feature is quite promising for large-scale data analysis. To justify that the favorable performance achieved by the MBSS with the RPCA was not due to the sampled fibers (which occasionally noise-free, since the noises were very sparse), the MBSS procedure was repeated but without the RPCA preprocessing procedure and results are presented in the same figure with the cyan circles marks). From the figure, it is evident that the RPCA played a key role to improve the performance of the MBSS for data with outliers. In summary, compared with ordinary Tucker decomposition, carefully designed MBSS is more flexible and robust and it is able to tackle some very challenging problems in practical applications.

Table 2
Comparison of performances of the MBSS, HOOI+BSS and TuckerALS+BSS in the decomposition of a tensor with mixed constraints. Very large sparse noise with SNR = -20 dB was added. The MBSS used the RPCA to preprocess the sampled fibers

Algorithm	mSIR_1	mSIR_2	mSIR_3	Runtime (s)	Fit
MBSS	**47**	**18**	**21**	**2.4**	**1.0**
HOOI	2.1	2.4	1.0	63	-0.4
TuckerALS	5.1	7.7	11	58	-0.0

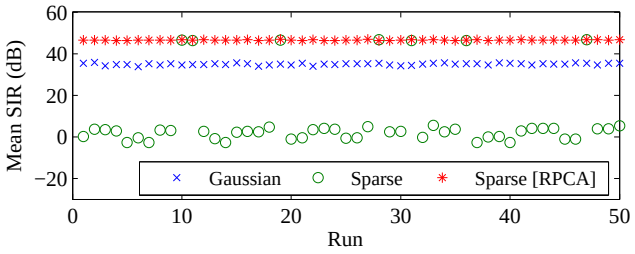

Fig. 6. Mean SIRs of $\mathbf{A}^{(1)}$ obtained by the MBSS with different configurations over 50 runs. The results are stable although randomly sampled fibers were used. The MBSS without the RPCA performed poorly, which justifies to use the RPCA

Simulation 2. In this simulation MBSS incorporating NMF methods is applied to perform nonnegative Tucker decomposition (NTD) of large-scale data. Three sets of nonnegative signals were chosen from the benchmarks of NMFLAB, see Fig. 7a-c for their waveforms. Each set consisted of five signals and the sample numbers were all 1,000. The entries of the core tensor $\underline{\mathbf{G}} \in \mathbb{R}^{5\times5\times5}$ were drawn from a uniform distribution, and 60% of them were randomly set to zero. By using such components a large data tensor $\underline{\mathbf{Y}} \in \mathbb{R}^{1000\times1000\times1000}$ with sparse components was constructed using the Tucker model. Finally, 20 dB noise drawn from independent uniform distributions was added to $\underline{\mathbf{Y}}$. For this large data tensor, most of existing NTD algorithms such as the HALSNTD [50] and HONMF algorithm [16] ran *out of memory* or their convergence was extremely slow in our computer and thus failed to perform nonnegative Tucker decompositions. In MBSS, this time we applied the DNNMF algorithm [51] to extract nonnegative components in each mode and using only $60J_n$ (i.e., 300) fibers $n = 1, 2, 3$. Figure 7d-f shows the recovered waveforms by the MBSS and (g) shows the corresponding SIRs of each component. From the figure, it is evident that all components were nicely recovered by the MBSS. The averaged SIRs of the estimated components were 21 dB, 29 dB, and 26 dB. Moreover, MBSS consumed only 32.3 seconds and achieved a fit of 0.9192 in a typical run. (We have used the multiplicative update rule proposed in [52] to obtain the nonnegative core tensor). For a comparison, TuckerALS with nonnegativity constraints consumed 2344.9 seconds to achieve a fit of 0.8132, using only one iteration. By setting the maximum iteration number only 10, TuckerALS consumed 23440 seconds and achieved a fit of 0.92. However, the averaged SIRs of the components estimated by TuckerALS were only 3.9, 2.4, and 2.4 dB. From these results we can conclude that the MBSS is quite competitive with existing algorithms for large-scale nonnegative Tucker decomposition.

Simulation 3. In this simulation we applied MBSS to the COIL-20 images clustering [53]. The database COIL-20 consists of 1440 gray images of 20 objects (72 images per object). Each image has been preprocessed and was with the size of 128×128, which was captured from different orientations of a object. We stacked these images together and formed a tensor $\underline{\mathbf{Y}}$ with the size of $128 \times 128 \times 1440$. In the first step the tensor $\underline{\mathbf{Y}}$ was decomposed by using MBSS with $J_1 = J_2 = 5,\ J_3 = 25$. In MBSS, we used LRA-NMF described in detail in [52] to extract each factor. Then we obtained two sets of features: $\mathbf{F}_\text{M}$=$\widehat{\mathbf{A}}^{(3)}$ and

$$\mathbf{F}_\text{T} = \underline{\mathbf{Y}} \times_1 \widehat{\mathbf{A}}^{(1)\dagger} \times_2 \widehat{\mathbf{A}}^{(2)\dagger}, \tag{25}$$

where the features in $\mathbf{F}_\text{M}$ are a sort of features which can actually be extracted by running matrix factorization, e.g., NMF, on the unfolding version $\mathbf{Y}_{(3)}$ directly, whereas the features in $\mathbf{F}_\text{T}$ are tensor features as they have exploited the Tucker structure of tensors. Then we used their two t-SNE [54] components to visualize and cluster the images by using the K-means method. It is well known that K-means often gives slightly different clustering results in different runs. To reduce the uncertainty, in each run of K-means, K-means was replicated 5 times, each with a new of initial cluster centroid positions (see the document for K-means included in Matlab Statistics Toolbox). Then we ran K-means 100 times and their averaged values of clustering accuracy were recorded and compared (see [55] for the definition of clustering accuracy). From our experimental results, if $\mathbf{F}_\text{M}$ was used, the averaged clustering accuracy was 72.57%. If $\mathbf{F}_\text{T}$ was adopted, the averaged accuracy was increased to 79.58%, which shows that the clustering procedure indeed benefitted from the Tucker structure. This also shows that, although the MBSS is based on independent matrix factorizations, it is different from ordinary matrix factorizations because its factors actually share a special multilinear structure. This also partially explain why tensor decompositions cannot be simply replaced by matrix factorizations. In fact, its Tucker structure allows

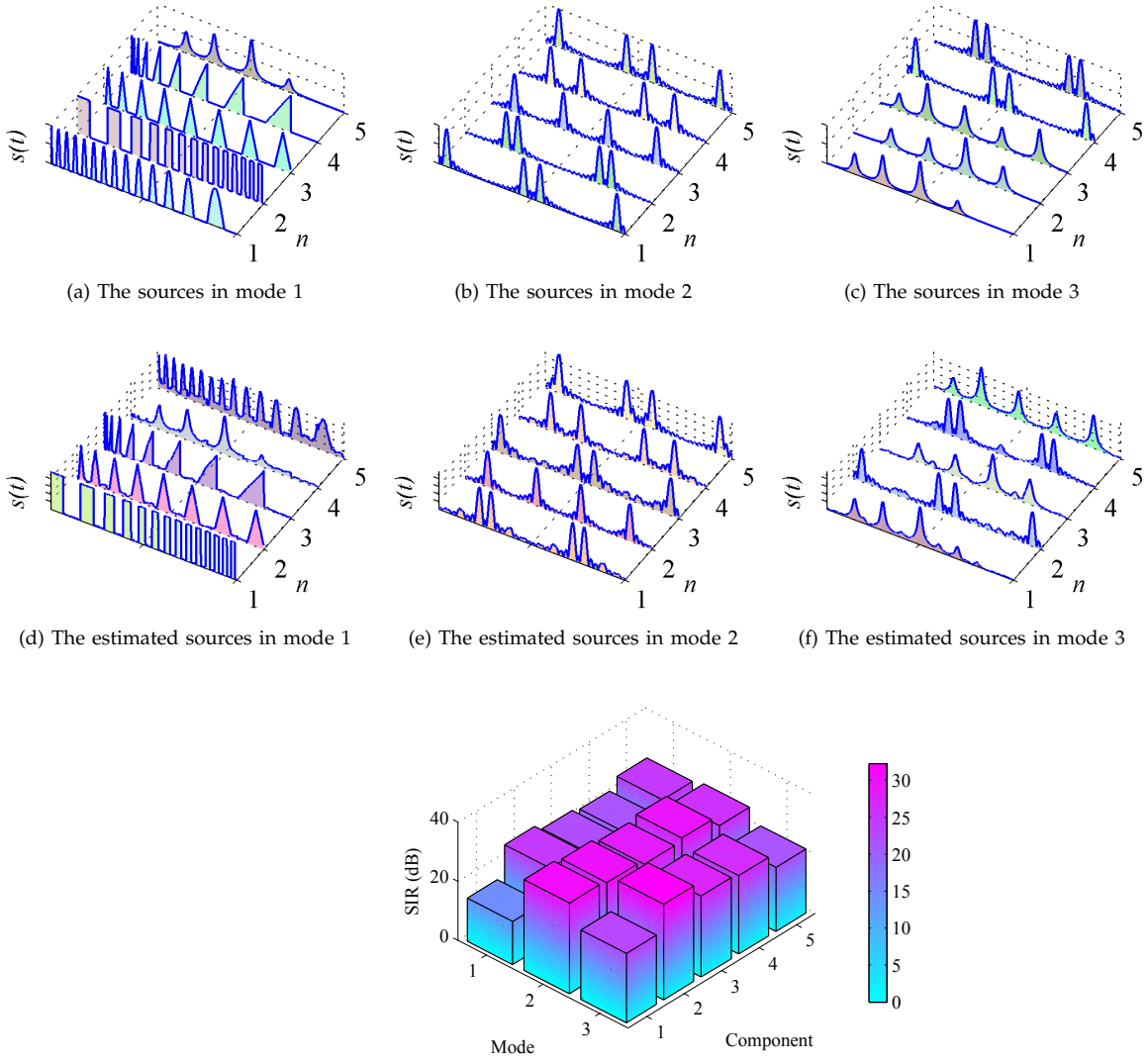

(a) The sources in mode 1 (b) The sources in mode 2 (c) The sources in mode 3

(d) The estimated sources in mode 1 (e) The estimated sources in mode 2 (f) The estimated sources in mode 3

(g) SIRs of individual signals achieved by using the MBSS

Fig. 7. Performance of the MBSS for Nonnegative Tucker Decomposition (NTD) of a large-scale tensor with the size of $1000 \times 1000 \times 1000$, where the DNNMF algorithm was used to extract nonnegative components. Most source signals were nicely recovered and the runtime was only 32 seconds. For this large-scale tensor NTD methods such as HALSNTD and HONMF ran *out of memory* on our computer standard PC

us to perform more complicated data analysis tasks. The above mentioned implementation of the MBSS was also compared with the HOOI, the TuckerALS, and the HALSNTD. The maximum iteration number of these ALS algorithms was set 500. After the decomposition, $\mathbf{F}_{\mathrm{T}}$ defined by (25) were computed and their two t-SNE components were clustered by using K-means. In clustering stage all the algorithms used the same configuration as MBSS, which has been detailed above. The results are shown in Table 3. Note that the HOOI did not impose any nonnegative constraints, Tucker-ALS only imposed the nonnegative constraints on the loading matrices (it currently cannot impose nonnegativity on the core tensor), whereas the HALSNTD and the MBSS impose the full nonnegative constraints (all the loading matrices and the core tensor are nonnegative). So the fits of the HALSNTD and MBSS were slightly lower than those of the HOOI and TuckerALS. MBSS did not use ALS iterations, however, it obtained almost the same fit as the HALSNTD, but much faster than the HALSNTD and the TuckerALS (MBSS was slower than the HOOI because the HOOI did not need to impose nonnegative constraints.) The final fit and clustering accuracy reveals that, although without ALS iterations, the MBSS is able to provide better or similar results by consuming significantly reduced time in comparison to ALS methods.

Table 3
Comparison of performance of 4 algorithms for the real-world application – COIL 20 images clustering

Algorithm	HOOI	TuckerALS	HALSNTD	MBSS
Runtime(s)	13	5644	3603	45
Fit	0.69	0.69	0.67	0.66
Accuracy (%)	73	71	78	80

Simulation 4. In this simulation the MBSS is applied to the steady-state visual evoked potential (SSVEP) data analysis using real EEG data. SSVEP is a periodic electrical response over the occipital scalp areas of the brain, elicited by the repetitive presentation of a flickering visual stimulus. SSVEP has the same frequency (plus higher harmonics) as the stimulus, and can be recorded from the scalp using electroencephalography (EEG) [56]. Based on this mechanism a SSVEP brain-computer interface (BCI) can be designed, which typically depends on the external visual stimuli which are in the form of an array of light sources with different and distinct frequencies [57]. SSVEP BCI can translate the frequency modulation of EEG signals into computer commands, by recognizing the frequency components of the EEG signals recorded during different stimulus presentations [58]. How to extract and recognize SSVEP components accurately is one of the crucial issues for SSVEP BCI. Although SSVEP is evoked by a repetitive stimulus with relatively stationary intensity, the spontaneous EEG signal or noise with the same frequency as the stimulus and its harmonics, but having time-varying intensity, may contaminate the SSVEP measured from the scalp and make it an unstable signal [59]. Effective extraction of the true SSVEP components from the EEG signals will help in enhancing the recognition accuracy of stimulus frequency components, thereby improving the performance of SSVEP BCI. Here, we validate the proposed MBSS algorithm with real EEG data recorded in a SSVEP experiment in comparison to the TuckerALS, the HONMF and the HALSNTD [50] algorithms.

The EEG signals were recorded at a 250 Hz sampling rate from eight channels P7, P3, Pz, P4, P8, O1, Oz and O2 (arranged according to the international 10–20 standard system) by a Biosemi Active Two amplifier, with a bandpass filtering 5–50 Hz. The EEG data were then collected from 12 stimulus trials with 4 s duration for each trial. The first six trials correspond to 6.5 Hz flickering frequency and the remaining to 10.5 Hz. A complex Morlet wavelet transform was first applied to obtain the time-frequency information from the EEG data with the minimum frequency resolution of 0.5 Hz. Finally, an EEG spectrum tensor with dimension of 91 frequency components $\times$ 1000 sample points $\times$ 8 channels $\times$ 12 trials was constructed.

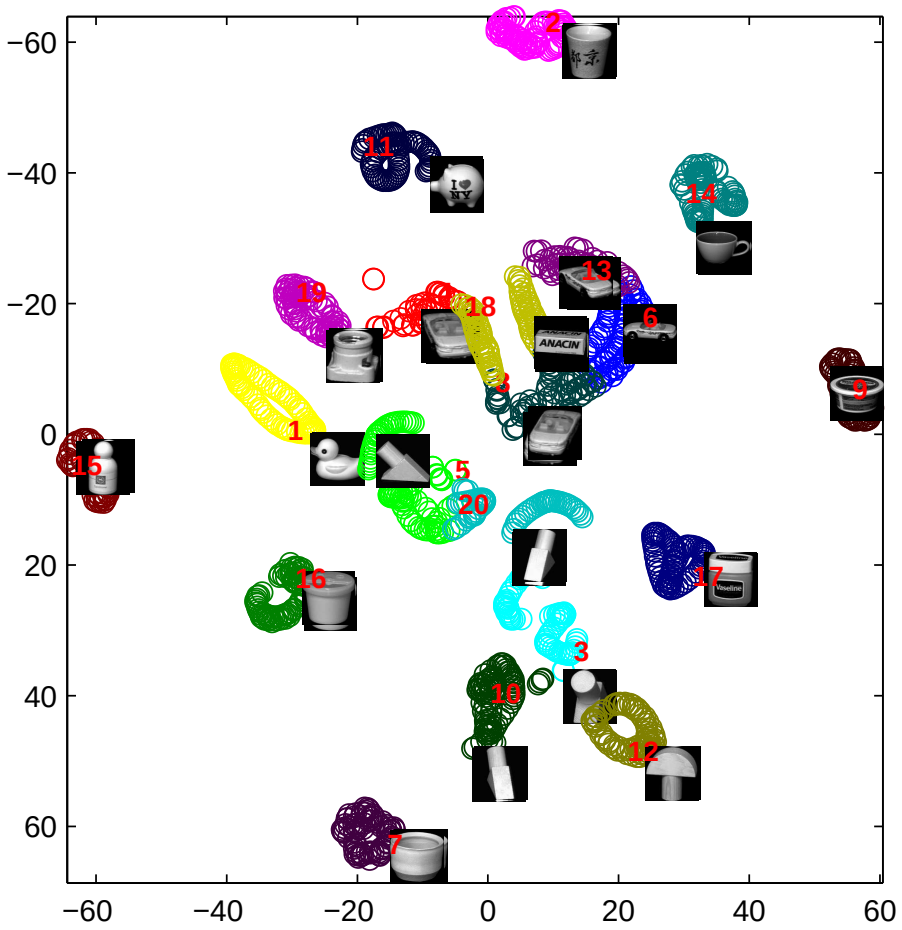

Fig. 8. Example 3: Visualization of two t-SNE components obtained from the feature $\mathbf{F}_{\mathrm{T}}$ extracted by using MBSS with LRA-NMF. The averaged clustering accuracy was 79.58% over 100 runs

In the MBSS, only $40J_n$ fibers were uniformly randomly sampled and then the DNNMF algorithm was employed to extract the latent non-negative components. Figure 9 illustrates the four-way EEG spectrum tensor factorization results upon applying the MBSS. Two components in factor $\mathbf{A}^{(1)}$ explicitly represent the SSVEP frequency components consisting of the fundamental frequency and higher harmonics, corresponding to the stimulus frequencies of 6.5 Hz and 10.5 Hz. The components of $\mathbf{A}^{(2)}$ and $\mathbf{A}^{(3)}$ reflect the temporal and spatial information about the SSVEP spectrum, respectively. The components in factor $\mathbf{A}^{(4)}$ provide considerably discriminative class information, which show trials 1–6 have larger contributions on the stimulus frequency of 6.5 Hz, whereas trials 7–12 are more related to the stimulus frequency of 10.5 Hz. We further compare the TuckerALS with nonnegativity constraints, MBSS, HONMF and HALS. The maximum iteration number for each algorithm was 100. Figure 10 shows the class information obtained by each algorithm. From the figure, it is seen that the MBSS yields much more discriminative class features than the other existing algorithms.

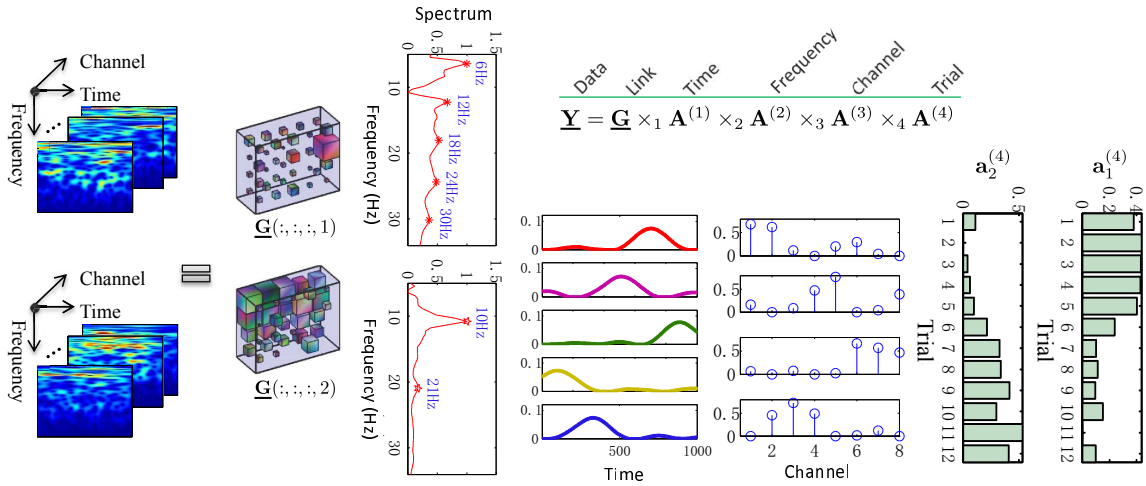

Fig. 9. Example 4: Four-way EEG spectrum tensor (frequency × time × channel × trial) factorization by MBSS. The example includes 12 trials recorded from eight channels P7, P3, Pz, P4, P8, O1, Oz and O2 during 6.5 Hz and 10.5 Hz flickering visual stimulus (6 trials each). Frequency components between 5 Hz and 50 Hz with 0.5 Hz resolution (i.e., 91 frequency bins) were analyzed and the time window length was 4s (i.e., 1000 sample points). Each trial is represented by a 3-way tensor with dimension of 91 × 1000 × 8

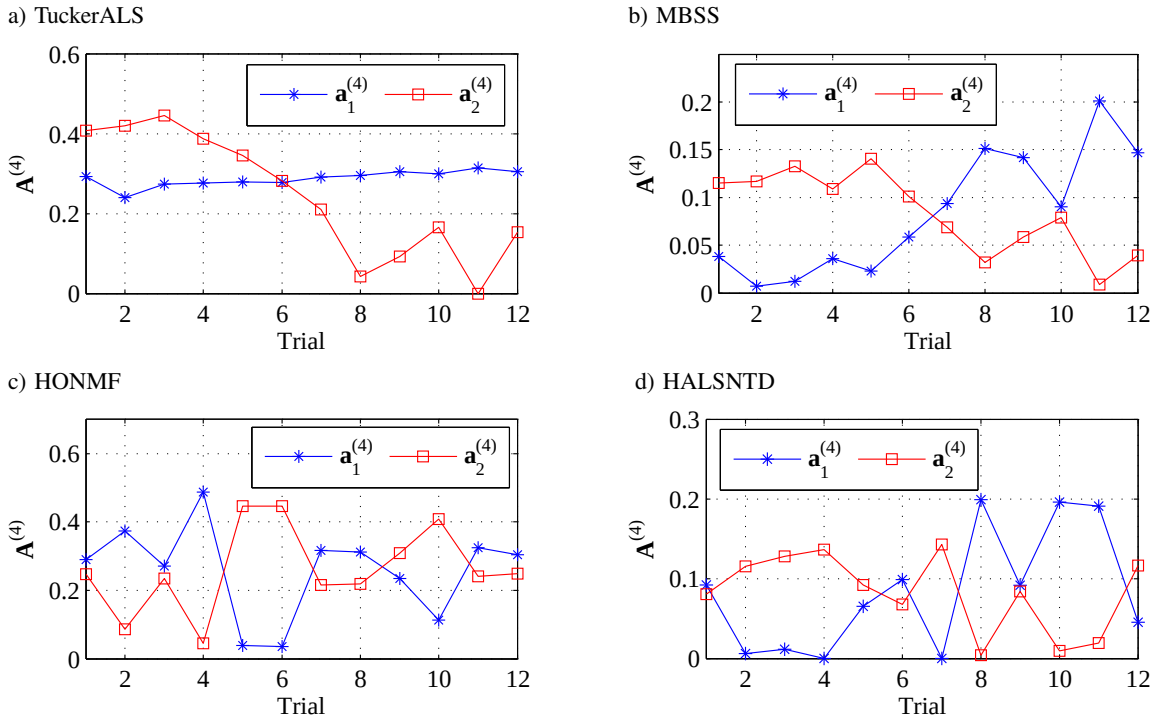

Fig. 10. Plots of vector $\mathbf{a}_1^{(4)}$ and $\mathbf{a}_2^{(4)}$ of the factor matrix $\mathbf{A}^{(4)} = [\mathbf{a}_1^{(4)}, \mathbf{a}_2^{(4)}]$ representing class information of the SSVEP for the TuckerALS, MBSS, HONMF and HALS algorithms. The first 6 trials correspond to the class 1 SSVEP with frequency 6.5 Hz and the next 6 trials correspond to the class 2 SSVEP with frequency 10.5 Hz. From these plots it is clear that the MBSS method provides, in this case, the best discriminative features

Their computation time and fit are shown in Table 4. It should be noted that the MBSS needs much less computation time in comparison to the others, and achieves comparable fit. The TuckerALS and the MBSS implemented here did not impose nonnegativity constraints on the core tensor. From the experimental results, by using the existing the DNN-MF method, the decomposition results obtained by MBSS are more interpretable and the such decompositions are also more efficient than NTD methods employing ALS approach. Here, our aim was not to show that the proposed MBSS can yield better performance than that of other commonly used methods for SSVEP analysis, but rather to show that the MBSS is quite promising in the real-world data analysis. Worth mentioning, this may also provide a novel way to analyze EEG data. Instead of usual two-way analysis (e.g., temporal-spatial analysis) for the EEG data, the MBSS approach attempts to extract the SSVEP components by multiway-array factorization from the four-way EEG spectrum tensor which integrates time-frequency features, temporal-spatial patterns and trial-to-trial variability. The MBSS can impose various constraints on the data in different ways according to the corresponding characteristics of the electrophysiological signals, and may provide more intuitive interpretations for the physical meaning of the signals, thereby assisting the follow-up signal analysis, such as the classification or detection in BCIs.

Table 4
Comparison of performances of 4 algorithms for the steady-state visual evoked potential (SSVEP) data analysis in terms of run time and fit

Algorithm	TuckerALS	MBSS	HALSNTD	HONMF
Runtime(s)	596	9	236	238
Fit	0.54	0.53	0.53	0.52

6. Conclusions

The existing methods for the constrained Tucker decompositions are often slow, stuck in local minima and do not provide unique desired decompositions and therefore, the results are difficult to interpret. In this paper, a simple approach based on the generalized multiway blind source separation (MBSS) is investigated. Using the MBSS approach described in detail, the component matrices, which are the subject of our main interest, are estimated directly by applying existing efficient BSS methods to each unfolding matrix of the data tensor. This approach leads to essentially unique (neglecting unavoidable scaling and permutation ambiguities of the components) Tucker decompositions with usually meaningful and physically interpretable results. In other words, we have demonstrated that by employing the MBSS approach, constrained or penalized Tucker decompositions provide essentially unique decompositions and thus the extracted components have specific statistical or deterministic properties (e.g., statistical independence, smoothness, sparseness and nonnegativity)[12]. The MBSS approach provides an attractive and efficient alternative to existing algorithms for unique tensor analysis. Note that in the MBSS approach the specific component matrices of interest can be extracted independently of other modes, directly from a reduced matricized data without the need to perform a full decomposition of the whole data tensor, e.g.,without the need to employ ALS algorithms which may fail to perform such decompositions, especially for ill-conditioned, highly collinear or noisy data. Simulations show the validity and efficiency of the proposed method, especially for large-scale problems.

In summary, the MBSS approach can be viewed as a very flexible and general technique for constrained or penalized tensor decompositions, which is an efficient alternative to many existing algorithms for tensor decompositions, especially to a wide class of the ALS algorithms. The extensive computer simulations confirmed that by using the MBSS approach, we can reduce the computing time at least by one or two orders of magnitude by comparison with ALS and HOOI algorithms under assumptions that some *a priori* knowledge about the hidden components is available. Moreover, for experimental, real world data, the MBSS often gives more meaningful components of hidden latent variables, with proper physical or physiological interpretations. However, if such kind of *a priori* knowledge is not available, the standard Tucker or CP (PARAFAC) decomposition algorithms should still be the first choices.

Acknowledgements. This work was in part supported by the National Natural Science Foundation of China (Grant 61103122, 61104053), and the China Postdoctoral Science Foundation funded project (Grant 201104360).

REFERENCES

[1] F. Hitchcock, "Multiple invariants and generalized rank of a p-way matrix or tensor", *J. Mathematics and Physics* 7, 39–79 (1927).

[2] L. Tucker, "Some mathematical notes on three-mode factor analysis", *Psychometrika* 31 (3), 279–311 (1966).

[3] L. De Lathauwer, B. De Moor, and J. Vandewalle, "A multilinear singular value decomposition", *SIAM J. on Matrix Analysis and Applications* 21, 1253–1278 (2000).

[4] T.G. Kolda and B.W. Bader, "Tensor decompositions and applications", *SIAM Review* 51 (3), 455–500 (2009).

[5] A. Cichocki, R. Zdunek, A.-H. Phan, and S. Amari, *Nonnegative Matrix and Tensor Factorizations: Applications to Exploratory Multi-way Data Analysis and Blind Source Separation*, Wiley, Chichester, 2009.

[6] A. Cichocki, "Tensors decompositions: new concepts for brain data analysis?", *J. Control, Measurement, and System Integration (SICE)* 7, 507–517 (2011).

[7] L. De Lathauwer, B. De Moor, and J. Vandewalle, "On the best rank-1 and rank-$(R_1, R_2, ..., R_n)$ approximation of higher-order tensors", *SIAM J. on Matrix Analysis and Applications* 21 (4), 1324–1342 (2000).

[8] F. Miwakeichi, E. Martnez-Montes, P. Valds-Sosa, N. Nishiyama, H. Mizuhara, and Y. Yamaguchi, "Decomposing EEG data into space-time-frequency components using parallel factor analysis", *NeuroImage* 22 (3), 1035–1045 (2004).

[12] Of course, some BSS algorithms can also stuck in local minima, but usually the MBSS approach alleviate this problem due to the reduction degree of freedom.

[9] Z. He, A. Cichocki, S. Xie, and K. Choi, "Detecting the number of clusters in n-way probabilistic clustering", *IEEE Trans. on Pattern Analysis and Machine Intelligence* 32 (11), 2006–2021 (2010).

[10] H.A. Phan and A. Cichocki, "Tensor decompositions for feature extraction and classification of high dimensional datasets", *Nonlinear Theory and Its Applications, IEICE* 1 (1), 37–68 (2010).

[11] R. Bro, "Multi-way analysis in the food industry: Models, algorithms & applications", *Food Technology* 309, http://curis.ku.dk/ws/files/13035961/Rasmus_Bro.pdf, (1998).

[12] A.H. Andersen and W.S. Rayens, "Structure-seeking multilinear methods for the analysis of fMRI data", *NeuroImage* 22 (2), 728–739 (2004).

[13] E. Martínez-Montes, P.A. Valdés-Sosa, F. Miwakeichi, R. Goldman, and M. Cohen, "Concurrent EEG/fMRI analysis by multiway partial least squares", *NeuroImage* 22 (3), 1023–1034 (2004).

[14] E. Acar, C. Aykut-Bingol, H. Bingol, R. Bro, and B. Yener, "Multiway analysis of epilepsy tensors", *Bioinformatics* 23 (13), i10–i18 (2007).

[15] M. De Vos, A. Vergult, and L. De Lathauwer, "Canonical decomposition of ictal scalp EEG reliably detects the seizure onset zone", *NeuroImage* 37 (3), 844–854 (2007).

[16] M. Mørup, L.K. Hansen, and S.M. Arnfred, "Algorithms for sparse nonnegative Tucker decompositions", *Neural Computation* 20 (8), 2112–2131 (2008).

[17] L. De Lathauwer, "A survey of tensor methods", *IEEE Int. Symposiumon Circuits and Systems (ISCAS)* 1, 2773–2776 (2009).

[18] V. De Silva and L.-H. Lim, "Tensor rank and the ill-posedness of the best low-rank approximation problem", *SIAM J. on Matrix Analysis and Applications* 30 (3), 1084–1127 (2008).

[19] S. Weiland and F. Van Belzen, "Singular value decompositions and low rank approximations of tensors", *IEEE Trans. on Signal Processing* 58 (3), 1171–1182 (2010).

[20] L. De Lathauwer, "A link between the canonical decomposition in multilinear algebra and simultaneous matrix diagonalization", *SIAM J. on Matrix Analysis and Applications* 28 (3), 642–666 (2006).

[21] C.F. Beckmann and S.M. Smith, "Tensorial extensions of independent component analysis for multisubject fMRI analysis", *NeuroImage* 25 (1), 294–311 (2005).

[22] M. De Vos, L. De Lathauwer, and S. Van Huffel, "Algorithm for imposing SOBI-type constraints on the CP model", *IEEE Int. Symp. Circuits and Systems (ISCAS).*, 2008, 1344–1347.

[23] M. Vasilescu and D. Terzopoulos, "Multilinear independent components analysis", *IEEE Computer Society Conf. on Computer Vision and Pattern Recognition* 1, 547–553 (2005).

[24] S. Unkel, A. Hannachi, N. Trendafilov, and I. Jolliffe, "Independent component analysis for three-way data with an application from atmospheric science", *J. Agricultural, Biological, and Environmental Statistics* 16, 319–338 (2011).

[25] A. Bell and T. Sejnowski, "An information-maximization approach to blind separation and blind deconvolution", *Neural Computation* 7, 1129–1159 (1995).

[26] A. Hyvarinen, J. Karhunen, and E. Oja, *Independent Component Analysis*, Wiley, New York, 2001.

[27] A. Cichocki and S. Amari, *Adaptive Blind Signal and Image Processing: Learning Algorithms and Applications*, John Wiley & Sons, London, 2002.

[28] A. Karfoul, L. Albera, and L. De Lathauwer, "Iterative methods for the canonical decomposition of multi-way arrays: Application to blind underdetermined mixture identification", *Signal Processing* 91 (8), 1789–1802 (2011).

[29] M. Zibulevsky and B. A. Pearlmutter, "Blind source separation by sparse decomposition in a signal dictionary", *Neural Computation* 13 (4), 863–882 (2001).

[30] P. Georgiev, F. Theis, and A. Cichocki, "Sparse component analysis and blind source separation of underdetermined mixtures", *IEEE Trans. on Neural Networks* 16 (4), 992–996 (2005).

[31] D.D. Lee and H.S. Seung, "Learning the parts of objects by non-negative matrix factorization", *Nature* 401 (6755), 788–791 (1999).

[32] B.W. Bader and T.G. Kolda, "MATLAB tensor toolbox version 2.5", http://csmr.ca.sandia.gov/ tgkolda/TensorToolbox/, (2012).

[33] G. Zhou and A. Cichocki, "Canonical polyadic decomposition based on a single mode blind source separation", *IEEE Signal Processing Letters* 19 (8), 523–526 (2012).

[34] X. Feng and Z. Zhang, "The rank of a random matrix", *Applied Mathematics and Computation* 185 (1), 689–694 (2007).

[35] F.M. Fisher, *The Identification Problem in Econometrics*, McGraw-Hill, New York, 1966.

[36] M. De Vos, D. Nion, S. Van Huffel, and L. De Lathauwer, "A combination of parallel factor and independent component analysis", *Tech. Rep.*, ftp://ftp.esat.kuleuven.ac.be/pub/sista/mdevos/reports/Ica_cp08.pdf (2008).

[37] D. Langers, "Unbiased group-level statistical assessment of independent component maps by means of automated retrospective matching", *Human Brain Mapping* 31, 727–742 (2010).

[38] A. Cichocki, "Generalized component analysis and blind source separation methods for analyzing mulitchannel brain signals", *Statistical and Process Models for Cognitive Neuroscience and Aging* 1, 201–272 (2007).

[39] Z. Lin, M. Chen, and Y. Ma, "The augmented Lagrange multiplier method for exact recovery of corrupted low-rank matrices", *ArXiv e-prints*, 1009.5055 (2010).

[40] P. Drineas, R. Kannan, and M.W. Mahoney, "Fast Monte Carlo algorithms for matrices II: computing a low-rank approximation to a matrix", *SIAM J. on Computing* 36 (1), 158–183 (2006).

[41] M.W. Mahoney and P. Drineas, "CUR matrix decompositions for improved data analysis", *Proc. Nat. Ac. Sciences* 106 (3), 697–702 (2009).

[42] C.F. Caiafa and A. Cichocki, "Generalizing the column-row matrix decomposition to multi-way arrays", *Linear Algebra and Its Applications* 433 (3), 557–573 (2010).

[43] E. Ceulemans and H.A.L. Kiers, "Selecting among three-mode principal component models of different types and complexities: a numerical convex hull based method", *British J. Mathematical and Statistical Psychology* 59 (1), 133–150 (2006).

[44] H.A.L. Kiers and A. der Kinderen, "A fast method for choosing the numbers of components in tucker3 analysis", *British J. Mathematical and Statistical Psychology* 56 (1), 119–125 (2003).

[45] M.O. Ulfarsson and V. Solo, "Dimension estimation in noisy pca with sure and random matrix theory", *IEEE Trans. on Signal Processing* 56 (12), 5804–5816 (2008).

[46] A. Cichocki, S. Amari, and K. Siwek, "ICALAB toolbox", http://www.bsp.brain.riken.jp/ICALAB (2007).

[47] Z. Koldovsky, P. Tichavsky, and E. Oja, "Efficient variant of

algorithm FastICA for independent component analysis attaining the Cramer-Rao lower bound", *IEEE Trans. on Neural Networks* 17 (5), 1265–1277 (2006).

[48] A. Belouchrani, K. AbedMeraim, and J.F. Cardoso, "A blind source separation technique using second-order statistics", *IEEE Trans. on Signal Processing* 45 (2), 434–444 (1997).

[49] C.A. Andersson and R. Bro, "The N-way toolbox for MATLAB", http://www.models.life.ku.dk/source/nwaytoolbox/ (2000).

[50] A.H. Phan and A. Cichocki, "Extended HALS algorithm for nonnegative Tucker decomposition and its applications for multiway analysis and classification", *Neurocomputing* 74 (11), 1956–1969 (2011).

[51] R. Zdunek, H.A. Phan, and A. Cichocki, "Damped Newton iterations for nonnegative matrix factorization", *Australian J. Intelligent Information Processing Systems* 12 (1), 16–22 (2010).

[52] G. Zhou, A. Cichocki, and S. Xie, "Fast nonnegative matrix/tensor factorization based on low-rank approximation", *IEEE Trans. on Signal Processing* 60 (6), 2928–2940 (2012).

[53] S.A. Nene, S.K. Nayar, and H. Murase, "Columbia object image library (COIL-20)", http://www.cs.columbia. edu/ CAVE/software/softlib/coil-20.php (1996).

[54] L. Van Der Maaten and C. Detection, "Visualizing data using t-SNE", *J. Machine Learning Research* 9, 2579–2605 (2008).

[55] Y. Yang, D. Xu, and F. Nie, "Image clustering using local discriminant models and global integration", *IEEE Trans. on Image Processing* 19 (10), 2761–2773 (2010).

[56] B.Z.Allison, D.J. McFarland, G. Schalk, S.D. Zheng, M. Jackson, and J.R. Wolpaw, "Towards an independent brain-computer interface using steady state visual evoked potentials", *Clinical Neurophysiology* 119 (2), 399–408 (2008).

[57] Y. Zhang, G. Zhou, Q. Zhao, A. Onishi, J. Jin, X. Wang, and A. Cichocki, "Multiway canonical correlation analysis for frequency components recognition in SSVEP-based BCIs", *Neural Information Processing*, Springer, Berlin, 2011.

[58] X. Gao, D. Xu, M. Cheng, and S. Gao, "A BCI-based environmental controller for the motion-disabled", *IEEE Trans. on Neural Systems and Rehabilitation Engineering* 11 (2), 137–140 (2003).

[59] Z. Wu and D. Yao, "Frequency detection with stability coefficient for steady-state visual evoked potential (SSVEP)-based BCIs", *J. Neural Engineering* 5 (1), 36 (2008).

BULLETIN OF THE POLISH ACADEMY OF SCIENCES
TECHNICAL SCIENCES, Vol. 60, No. 3, 2012
DOI: 10.2478/v10175-012-0052-3

ICA-based EEG denoising: a comparative analysis of fifteen methods

L. ALBERA[1,2], A. KACHENOURA[1,2], P. COMON[3]*, A. KARFOUL[4], F. WENDLING[1,2], L. SENHADJI[1,2], and I. MERLET[1,2]

[1] INSERM, UMR 1099, F-35000 Rennes, France
[2] Université de Rennes 1, LTSI, F-35000 Rennes, France
[3] CNRS, UMR5216, GIPSA-Lab, BP.46, F-38402 St Martin d'Heres cedex, France
[4] Al-Baath University, Faculty of Mechanical and Electrical Engineering, PB. 2244, Homs, Syria

Abstract. Independent Component Analysis (ICA) plays an important role in biomedical engineering. Indeed, the complexity of processes involved in biomedicine and the lack of reference signals make this blind approach a powerful tool to extract sources of interest. However, in practice, only few ICA algorithms such as SOBI, (extended) InfoMax and FastICA are used nowadays to process biomedical signals. In this paper we raise the question whether other ICA methods could be better suited in terms of performance and computational complexity. We focus on ElectroEncephaloGraphy (EEG) data denoising, and more particularly on removal of muscle artifacts from interictal epileptiform activity. Assumptions required by ICA are discussed in such a context. Then fifteen ICA algorithms, namely JADE, CoM_2, SOBI, SOBI_{rob}, (extended) InfoMax, PICA, two different implementations of FastICA, ERICA, SIMBEC, $\text{FOBIUM}_{\text{JAD}}$, TFBSS, ICAR_3, FOOBI_1 and 4-$\text{CANDHAP}_{\text{c}}$ are briefly described. Next they are studied in terms of performance and numerical complexity. Quantitative results are obtained on simulated epileptic data generated with a physiologically-plausible model. These results are also illustrated on real epileptic recordings.

Key words: ICA, comparative analysis, EEG denoising.

1. Introduction

The removal of muscular artifacts from ElectroEncephaloGraphic (EEG) data is a crucial preprocessing step for further analysis of EEG in the diagnosis of epilepsy from Video-EEG recordings. Indeed, in the particular context of epilepsy, EEG signals of interest, such as interictal spikes or ictal discharges, may be corrupted by muscular or myogenic activity arising from the contraction of head muscles. As already reported [1], these artifacts are difficult to remove. This is especially due to i) their high amplitude (possibly several times larger than the EEG signal), ii) the large frequency range of their components and iii) their variable topographical distribution. Due to the complexity of the involved physiological processes and the lack of reference signals, researchers have mostly considered Blind Source Separation (BSS) techniques to solve the EEG denoising problem [2–6].

Among BSS approaches, Independent Component Analysis (ICA) is one of the most famous, especially in biomedical engineering [7, 8]. It was historically the first to be applied to EEG denoising for muscular activity [1, 9, 10]. Indeed, by assuming that EEG data can be modeled as a noisy static mixture of mutual independent sources associated with different physiological phenomena, ICA is generally considered as a powerful tool for extracting the EEG signals of interest [11–13]. However to date, only a few ICA algorithms such as SOBI [14, 15], (extended) InfoMax [16, 17] and FastICA [18, ch.6] are used in practice to process biomedical signals.

In this paper, we have examined whether other ICA methods perform better or enjoy lower computational complexity, especially for the removal of muscle artifacts from interictal epileptiform activity. We first discuss the EEG denoising problem and the assumptions required by ICA. Second, classical statistical tools are provided in order to understand how the ICA concept can be implemented. Next, representative methods of two classes, including the most used ICA techniques in signal processing, are briefly described and studied in terms of performance and numerical complexity: techniques based on the Differential Entropy (DE) such as (extended) InfoMax [16, 17], PICA [19] and two different implementations of FastICA [18, ch.6] versus cumulant-based methods. Among cumulant-based techniques, representative algorithms of three subfamilies are studied: i) the techniques using only SO statistics of the data such as SOBI [14, 15], SOBI_{rob} [20], TFBSS [21], ii) the algorithms based on SO and FO statistics such as JADE [22], CoM_2 [23], and iii) the methods requiring only HO statistics such as ERICA [24], SIMBEC [25], $\text{FOBIUM}_{\text{JAD}}$ [26, 27], ICAR_3 [28, 29], FOOBI_1 [30], 4-$\text{CANDHAP}_{\text{c}}$ [31, 32]. Quantitative results are obtained on simulated epileptic data generated with a physiologically-plausible model [33–35]. These results are also illustrated on real data recorded in a patient with epilepsy.

2. Problem formulation and assumptions

Let's model the EEG signal recorded from N electrodes as one realization of an N-dimensional random vector process $\{\boldsymbol{x}[k]\}$. Each random vector $\boldsymbol{x}[k]$ can then be written as the following noisy static mixture of statistical random processes called *sources*:

*e-mail: p.comon@ieee.org

$$\begin{aligned}\boldsymbol{x}[k] &= \boldsymbol{A}^{(e)}\boldsymbol{s}^{(e)}[k] + \boldsymbol{A}^{(b)}\boldsymbol{s}^{(b)}[k] + \boldsymbol{A}^{(m)}\boldsymbol{s}^{(m)}[k] + \boldsymbol{n}[k] \\ \boldsymbol{x}[k] &= \boldsymbol{A}\,\boldsymbol{s}[k] + \boldsymbol{n}[k]\end{aligned} \quad (1)$$

where $\{\boldsymbol{s}^{(e)}[k]\}$, $\{\boldsymbol{s}^{(b)}[k]\}$, $\{\boldsymbol{s}^{(m)}[k]\}$, $\{\boldsymbol{n}[k]\}$ are random vector processes representing the P_e epileptic activity sources, the P_b background activity sources, the P_m muscular activity sources and the N-dimensional instrument noise, respectively. The mixing matrices $\boldsymbol{A}^{(e)}$, $\boldsymbol{A}^{(b)}$ and $\boldsymbol{A}^{(m)}$ model the transfer from all possible sources of activity within the brain to scalp electrodes.

The assumption of static linear model comes from the mathematical formulation of the EEG/MEG forward problem. More precisely it comes from the use of the quasi-static formulation of Maxwell's equations, called Poisson's equations, in order to compute the electrical transfer between the cortex and the scalp [36]. Indeed, the time-derivatives of the associated electric fields are sufficiently small to be ignored in classical Maxwell's equations. As far as the statistical properties of vector random process $\{\boldsymbol{s}^{(e)}[k]\}$, $\{\boldsymbol{s}^{(b)}[k]\}$, $\{\boldsymbol{s}^{(m)}[k]\}$ and $\{\boldsymbol{n}[k]\}$ are concerned, we can assume that they are independent as they correspond to different physiological/physical phenomena. Nevertheless, such an assumption is not valid within each vector random processes regarding its components. In particular, the P_e epileptic activity sources of $\{\boldsymbol{s}^{(e)}[k]\}$ may be statistically mutually dependent. Eventually, the $\{\boldsymbol{n}[k]\}$ vector random process can be assumed to be Gaussian as most of instrument noises.

Consequently, by using ICA, at best we can hope to identify three vector subspaces corresponding to the epileptic sources, the muscular sources and the background sources, respectively, but not exactly the $P_e + P_b + P_m$ sources involved in Eq. (1). Note that this subspace identification is sufficient for the EEG denoising problem since we don't want to exactly extract the P_e epileptic sources; in fact, we just want to remove the contribution of the muscular and background activities from the scalp data. Indeed, once the epileptic source subspace is identified by applying ICA to the scalp data, we get an estimate of $\boldsymbol{A}^{(e)}\boldsymbol{s}^{(e)}[k]$ for every time index m, say an estimate of the denoised scalp data. Nevertheless, as shown in Sec. 5, the estimation of the three subspace dimensions remains a difficult issue.

3. Statistical tools and ICA methods

3.1. Statistical tools characterizing mutual independence. Let's recall how to characterize the statistical independence of a set of P random signals $\{y_p[k]\}_{m\in\mathbb{N}}$ and how to use it in order to blindly separate mixed mutually independent sources. A random vector $\boldsymbol{y} = [y_1, \cdots, y_P]^\intercal$ has mutually independent components if and only if its Probability Density Function (PDF) $p_{\boldsymbol{y}}$ can be decomposed as the product of the P marginal PDFs, p_{y_p}, where p_{y_p} denotes the PDF of the p-th component y_p of $\boldsymbol{y}$.

Then a natural way of checking whether $\boldsymbol{y}$ has independent components is to measure a pseudo-distance between $p_{\boldsymbol{y}}$ and $\prod_p p_{y_p}$. Such a measure can be chosen among the large class of f-divergences. If the Kullback divergence is used, we get the Mutual Information (MI) of $\boldsymbol{y}$ [18]:

$$\mathrm{MI}(\boldsymbol{y}) = \int_{\mathbb{R}^P} p_{\boldsymbol{y}}(\boldsymbol{u}) \log\left(\frac{p_{\boldsymbol{y}}(\boldsymbol{u})}{\prod_{p=1}^P p_{y_p}(u_p)}\right) d\boldsymbol{u}. \quad (2)$$

It can be shown that the MI vanishes if and only if the P components of $\boldsymbol{y}$ are mutually independent, and MI is strictly positive otherwise.

Another measure based on the PDF of $\boldsymbol{y}$ is the DE of $\boldsymbol{y}$:

$$S(\boldsymbol{y}) = -\int_{\mathbb{R}^P} p_{\boldsymbol{y}}(\boldsymbol{u}) \log(p_{\boldsymbol{y}}(\boldsymbol{u}))\, d\boldsymbol{u} = -\mathsf{E}[\log(p_{\boldsymbol{y}}(\boldsymbol{y}))] \quad (3)$$

sometimes referred to as Shannon's joint entropy, where $\mathsf{E}[\cdot]$ denotes the mathematical expectation. This entropy is not invariant by an invertible change of coordinates, but only by orthogonal transforms. A fundamental result in information theory is that the DE can be used as a measure of non-gaussianity. Indeed, among the random vectors having an invertible covariance matrix, the Gaussian vector is the one that has the largest entropy. Then, to obtain a measure of non-gaussianity of $\boldsymbol{y}$ that is i) zero only for a Gaussian vector, ii) always positive and iii) invariant by any linear invertible transformation, one often uses a normalized version of the DE, called *negentropy*, and given by [18, ch.3]:

$$J(\boldsymbol{y}) = S(\boldsymbol{z}) - S(\boldsymbol{y}), \quad (4)$$

where $\boldsymbol{z}$ stands for the Gaussian vector with the same mean and covariance matrix as $\boldsymbol{y}$. Since MI and negentropy are simply related to each other [23], estimating the negentropy allows to estimate the MI. However, even if consistent estimators of PDFs exist (*e.g.* Parzen estimators [37]), the computation of integral (3) is time consuming, and often prohibitive.

A way to avoid the exact computation of the negentropy consists in using another measure of statistical independence that is less accurate but easier to compute. The *contrast* function [23, definition 5] built from the data cumulants satisfies this condition. From now on, we shall assume that all random variables are real. If we consider $\Phi_{\boldsymbol{x}}(\boldsymbol{u}) = \mathsf{E}[\exp(\mathrm{i}\boldsymbol{u}^\intercal\boldsymbol{x})]$ as the first characteristic function of a random vector $\boldsymbol{x}$, since $\Phi_{\boldsymbol{x}}(\boldsymbol{0}) = 1$ and $\Phi_{\boldsymbol{x}}$ is continuous, then there exists an open neighborhood of the origin, in which $\Psi_{\boldsymbol{x}}(\boldsymbol{u}) = \log(\Phi_{\boldsymbol{x}}(\boldsymbol{u}))$ can be defined. The r-th order moments are the coefficients of the Taylor expansion of $\Phi_{\boldsymbol{x}}$ about the origin, up to a multiplicative coefficient $\mathrm{i}^r/r!$. Similarly cumulants, denoted by $\mathcal{C}_{i,j,\cdots,\ell,\boldsymbol{x}}$, are the coefficients of the second characteristic function, $\Psi_{\boldsymbol{x}}$, up to a multiplicative coefficient of the same form [18, ch.3]. It is noteworthy that the components of the $(N \times N)$ well-known *covariance matrix* of an N-dimensional random vector $\boldsymbol{x}$ exactly match the Second Order (SO) cumulants of $\boldsymbol{x}$. By analogy, the $(N^2 \times N^2)$ matrix containing the Fourth Order (FO) cumulants of $\boldsymbol{x}$ is usually called the *quadricovariance matrix*.

Cumulants are more appropriate than moments for ICA context. Indeed, cumulants enjoy two important properties. First, if at least two components or groups of components of $\boldsymbol{x}$ are statistically independent, then all cumulants involving these components are null. For instance, if all components of $\boldsymbol{x}$ are mutually independent, then $\mathcal{C}_{i,j,\cdots,\ell,\boldsymbol{x}} = \delta[i,j,\cdots,\ell]\,\mathcal{C}_{i,i,\cdots,i,\boldsymbol{x}}$, where the Kronecker $\delta[i,j,\cdots,\ell]$

equals 1 when all its arguments are equal and is null otherwise. Second, if $\boldsymbol{x}$ is Gaussian, then all its Higher Order (HO) cumulants, *i.e.* cumulants of order strictly greater than two are null. So HO cumulants may be seen as a distance to normality. Note that moments do not enjoy these two key properties. Moments and cumulants share two other useful properties. On the one hand, they are both symmetric arrays, since the value of their entries does not change by permutation of their indices. Consequently, covariance and quadricovariance matrices are necessarily symmetric. On the other hand, moments and cumulants satisfy the multi-linearity property [38], which is illustrated in [12, equ. (5) and (6)]. In practice, cumulants can be estimated using both the Leonov-Shiryaev formula [39] and sample statistics [38]. More precisely, the Leonov-Shiryaev formula allows us to relate any qth order cumulant to moments of order lower than or equal to q. For example, the SO and FO cumulants of any zero-mean random vector $\boldsymbol{x}$ symmetrically distributed are given by:

$$\begin{aligned}\mathcal{C}_{n_1,n_2,\boldsymbol{x}} &= \mathsf{E}[x_{n_1}\, x_{n_2}]\\ \mathcal{C}_{n_1,n_2,n_3,n_4,\boldsymbol{x}} &= \mathsf{E}[x_{n_1}\, x_{n_2}\, x_{n_3}\, x_{n_4}] - \mathsf{E}[x_{n_1}\, x_{n_2}]\mathsf{E}[x_{n_3}\, x_{n_4}]\\ &\quad -\mathsf{E}[x_{n_1}\, x_{n_3}]\mathsf{E}[x_{n_2}\, x_{n_4}] - \mathsf{E}[x_{n_1}\, x_{n_4}]\mathsf{E}[x_{n_2}\, x_{n_3}]\end{aligned}$$

And a consistent estimate of q-th order moments of any stationary ergodic process is given by sample statistics. Hence the above relations allow to define consistent estimates of cumulants, called κ-statistics [38].

3.2. Classical ICA techniques. The InfoMax [16, 17] and FastICA [18, ch.6] methods avoid the exact computation of the integral given in (3). In fact, InfoMax solves the ICA problem by maximizing the DE of the output of an invertible non-linear transform of $\boldsymbol{y}[k] = \boldsymbol{W}^{\mathsf{T}}\boldsymbol{x}[k]$ with respect to $\boldsymbol{W}$ using the natural gradient algorithm [40]. In practice, non-linearities whose derivative are sub-Gaussian (resp. super-Gaussian) PDFs are sufficient for sub-Gaussian (resp. super-Gaussian) sources [16]. Regarding the deflationary implementation of FastICA, referred as to $\text{FastICA}_{\text{def}}$ in the sequel, the p-th ($1 \leq p \leq P$) source is extracted by maximizing an approximation of the negentropy $J(\boldsymbol{w}_p^{\mathsf{T}}\boldsymbol{x}[k])$ with respect to the $(N\times 1)$ vector $\boldsymbol{w}_p$. This maximization is achieved using an approximate Newton iteration, which actually reduces to a variable-step gradient algorithm. To prevent all vectors $\boldsymbol{w}_p$ from converging to the same maximum (which would yield several times the same source), the p-th output is decorrelated from the previously estimated sources after every iteration using a simple Gram-Schmidt orthogonalization. A non-deflation implementation of FastICA, referred as to $\text{FastICA}_{\text{sym}}$ in the following, which simultaneously extracts all sources, also exists. The joint orthogonalization is similar to that originally proposed in [41, 42].

In order to cover a wide range of source distributions (i.e. symmetric, assymmetric and multimodal), authors in [19] propose the Pearson-based ICA method, named PICA. This algorithm solves the ICA problem by maximizing the DE via a maximization of the likelihood of the separator $\boldsymbol{W}$. In this approach, the parametric Pearson model is used to model the source distributions. Parameters of this model can be computed using the statistical moments up to the fourth order [19]. In addition to the easy and fast computation of these parameters, Pearson parametric model also shows a good robustness against outliers. Finally, either the relative gradient [43], the natural gradient [40] or the fixed-point [44] algorithms can be used in order to maximize the used maximum likelihood function.

Cumulants can be used instead of non-linearities matched to the PDFs of the sources as proposed in [24]. According to [24], a solution to the ICA problem is nothing else than a saddle point of the obtained cumulant-based DE cost function. This is the principle of the Equivariant Robust ICA (ERICA) algorithm [24], which uses a quasi-Newton approach to get the saddle point. Authors show that its convergence is isotropic and independent of the source statistics. In addition, the SIMBEC (SIMultaneous Blind signal Extraction using Cumulants) algorithm proposed in [25] optimizes the maximum likelihood criterion using a gradient algorithm on the Stiefel manifold. This is done by resorting to a cumulant index-based objective function and consequently no a priori on the sources densities is required [25]. This function satisfies two important properties. First, it is real positive and its minimum value occurs when the normalized random variables follows a Gaussian distribution. Second, it is strictly convex with respect to the linear combination of the independent sources. Then, SIMBEC solves the ICA problem by looking for the maxima of that cumulant index-based objective function [25, Theorem 1].

The JADE [22], CoM_2 [23], SOBI [14, 15], SOBI_{rob} [20], $\text{FOBIUM}_{\text{JAD}}$ [27], TFBSS [21], ICAR_3 [29], FOOBI_1 [30] and $\text{4-CANDHAP}_{\text{c}}$ [32] methods also perform ICA using cumulants of the data [18]. SOBI, SOBI_{rob} and TFBSS use SO cumulants, CoM_2 and JADE use both the SO and FO cumulants, and $\text{FOBIUM}_{\text{JAD}}$, ICAR_3, FOOBI_1 and $\text{4-CANDHAP}_{\text{c}}$ only use the FO cumulants of the data. Next, JADE, SOBI, SOBI_{rob}, TFBSS, $\text{FOBIUM}_{\text{JAD}}$, ICAR_3, FOOBI_1 take advantage of the algebraic structure of the covariance and/or quadricovariance matrices by reformulating the ICA problem as a joint diagonalization problem [45, 46], while CoM_2 explicitly maximizes a contrast function based on the FO cumulants of the data by rooting successive polynomials. Note that the JAD method [45] was originally used to implement the JADE, SOBI, SOBI_{rob}, TFBSS, $\text{FOBIUM}_{\text{JAD}}$, ICAR_3 and FOOBI_1 algorithms. Eventually $\text{4-CANDHAP}_{\text{c}}$ makes use of the canonical decomposition [47] of a third order array having one unitary loading matrix. Such a decomposition is achieved by alternating between solving the Procrustes problem [48] and the computation of rank-one matrix approximations. Note that both SOBI approaches and the TFBSS method jointly diagonalize time delayed and time-frequency covariance matrices of the standardized data, respectively.

In an attempt to analyze more specifically the differences between these ICA methods, the following remarks can be made. First of all, contrary to the other algorithms, CoM_2, along with the seven methods based on a joint diagonalization scheme are semi-algebraic, i.e. they are based on a finite sequence of optimization problems for which an algebraic so-

lution is available. No particular initialization is required contrary to the other iterative approaches, and, in practice, they converge to the global solution even if no theoretical global convergence proof is yet available today. Moreover, contrary to the other methods, FOBIUM$_{\mathrm{JAD}}$, ICAR$_3$, FOOBI$_1$ and 4-CANDHAP$_{\mathrm{c}}$ require that all sources have FO marginal cumulants with the same sign. Unfortunately, such an assumption is not always realistic in biomedical contexts [49]. Another difference is the need for a spatial whitening (also called standardization) [23, Subsec. 2.2] [18]. This preprocessing, based on SO cumulants, is mandatory for JADE, CoM$_2$, SOBI, SOBI$_{\mathrm{rob}}$, PICA, for both implementations of for FastICA and TFBSS. Although it is not necessary, spatial whitening is highly recommended in InfoMax in order to improve its speed of convergence [50]. Regarding ERICA, SIMBEC, FOBIUM$_{\mathrm{JAD}}$, ICAR$_3$, FOOBI$_1$ and 4-CANDHAP$_{\mathrm{c}}$, they can work with HO cumulants without any standardization. In such a case, they are then asymptotically insensitive to the presence of a Gaussian noise with a non-diagonal covariance matrix. Nevertheless, preliminary computer results showed that a whitening should be used for the seven latter methods in the context of EEG denoising. We think that such a preprocessing forces the estimated mixing matrix to be well-conditionned while the original one is clearly underdetermined according to Eq. (1). Our best results were obtained for a standardization without any reduction of dimension. It is noteworthy that contrary to the other whitening-based approaches, the whitening of SOBI$_{\mathrm{rob}}$ is made using non-zero delayed covariance matrices. SOBI$_{\mathrm{rob}}$ is then asymptotically insensitive to the presence of a temporally white noise. Moreover, contrary to the other methods, SOBI and SOBI$_{\mathrm{rob}}$ need that all sources have different spectra. As far as TFBSS is concerned, it requires that all sources are non-stationnary but ergodic. Eventually, all methods except TFBSS, rely on the stationarity-ergodicity assumption to ensure an asymptotical mean square convergence of statistical estimators. Such an assumption is very rarely fulfilled in the context of EEG signals and a consistence analysis is difficult in the presence of such complex biomedical signals. Nevertheless the good behavior of some of these techniques on biomedical data shows that the stationnarity-ergodicity assumption is not absolutely necessary. Regarding the cumulant-based methods, even if sample statistics do not estimate accurately the cumulants of the data, they still satisfy reasonably the basic properties enjoyed by cumulants (see Subsec. 3.1).

4. Numerical complexity of ICA algorithms

Although the ultimate goal of comparing denoising approaches is to evaluate the quality of methods as reflected by the reconstructed signals, it is also interesting to assess the numerical complexity of these methods. Numerical complexity is defined here as the number of floating point operations required to execute an algorithm (flops). A flop corresponds to a multiplication followed by an addition. But, in practice, only the number of multiplications is considered since, most of the time, there are about as many (and slightly more) multiplications as additions. In order to simplify the expressions, the complexity is generally approximated by its asymptotic limit, as the size of the problem tends to infinity. We shall subsequently denote, with some small abuse of notation, the equivalence between two strictly positive functions f and g:

$$f(x) = \mathcal{O}[g(x)] \quad \text{or} \quad g(x) = \mathcal{O}[f(x)] \tag{5}$$

if and only if the ratio $f(x)/g(x)$ tends to 1 as $x \to \infty$. In practice, knowing whether an algorithm is computationally heavy is as important as knowing its performances in terms of SNR. Yet, despite its importance, the numerical complexity of the ICA algorithms is poorly addressed in the literature. This section first addresses the complexity of some elementary mathematical operations needed by ICA algorithms. Then, the numerical complexity of various ICA algorithms are reported and compared to each other as a function of the number of sources.

Many ICA algorithms use standard Eigen Value Decomposition (EVD) or Singular Value Decomposition (SVD), for instance when a whitening step is required to reduce the dimensions of the space. In addition to these decompositions, many other elementary operations are also considered such as solving a linear system, matrix multiplication, joint diagonalization of several matrices and computation of cumulants in the particular case of cumulant-based algorithms.

- Let $\boldsymbol{A}$ and $\boldsymbol{B}$ be two matrices of size $(N \times P)$ and $(P \times N)$, respectively. Then the numerical complexity of their product $\boldsymbol{G} = \boldsymbol{AB}$ is equal to N^2P flops, since each element of $\boldsymbol{G}$ requires P flops to be computed. The latter amount can be reduced to $(N^2 + N)P/2 = \mathcal{O}[N^2P/2]$ flops if $\boldsymbol{G}$ is symmetric.
- The solution of a $N \times N$ linear system via the LU decomposition requires approximately $\mathcal{O}[4N^3/3]$ flops.
- The numerical complexity of the SVD of $\boldsymbol{A} = \boldsymbol{U\Lambda V}^{\mathsf{T}}$ is given by $\mathcal{O}[2N^2P + 4NP^2 + 14P^3/3]$ when it is computed using the Golub-Reinsch algorithm [51]. This amount can be considerably reduced to $\mathcal{O}[2N^2P]$ when $\boldsymbol{A}$ is tall (i.e. $N \gg P$) using Chan's algorithm [52], known to be suitable in such a case.
- The numerical complexity of the EVD $\boldsymbol{G} = \boldsymbol{L\Sigma L}^{\mathsf{T}}$ is $\mathcal{O}[4N^3/3]$ flops.

As mentioned previously, all considered methods in this paper use a whitening step. Therefore computing the numerical complexity of this step is mandatory in our evaluation study. The so-called spatial whitening of the observed data consists of applying a linear transform so that the latent variables (sources) become as decorrelated as possible in the new coordinate system. To do so, this linear transformation is computed as the inverse of the square root of the EVD of the covariance matrix of the observations, [18, ch.1].

Hence and according to Table 1, the numerical complexity of this whitening step is equal to $KN^2/2 + 4N^3/3 + PNK$ flops, where K denotes the number of data samples. However, for the special case $N \ll K$, this linear transformation can be efficiently computed using the SVD of the data matrix $\boldsymbol{X}$ as proposed by Chan [52]. Then, the numerical complex-

ity of such computation is reduced to $\mathcal{O}[2KN^2]$ flops. As a result, when the minimal numerical complexity of the whitening step is considered, it is equal to $\min(KN^2/2+4N^3/3+PNK+,2KN^2)$ flops.

Table 1
Numerical complexity of elementary operations generally used in the ICA methods. $\boldsymbol{A}$ and $\boldsymbol{B}$ are two matrices of size $(N\times P)$ and $(P\times N)$, respectively. I and M stand for the number of executed sweeps and the number of matrices to be jointly diagonalized, respectively. $f_{2q}(N)$ denotes the number of free entries in the $2q$-th order cumulant array

	Numerical complexity (flops)
$\boldsymbol{G}=\boldsymbol{AB}$	N^2P
Lin. system solving	$4N^3/3$
SVD of $\boldsymbol{A}$	$2N^2P+4NP^2+14P^3/3$
EVD of $\boldsymbol{A}$	$4N^3/3$
JAD [45] (Symmetric case)	$IN(N-1)(4NM+17M+4N+75)/2$
Estimation of the $2q$-th order cumulants array	$(2q-1)Kf_{2q}(N)$
EVD – based whitening	$KN^2/2+4N^3/3+PNK$
SVD – based whitening	$\mathcal{O}[2KN^2]$

Some ICA algorithms [14, 21, 22, 53] are based on the joint orthogonal approximate diagonalization of a set $\{\boldsymbol{G}_m\}$ of M matrices of size $(N\times N)$. Recall that the joint orthogonal diagonalization problem is defined as the search for a unitary linear transformation that jointly diagonalizes the target matrices $\boldsymbol{G}_m$. A Jacobi-like algorithm such as JAD [45] is commonly used for joint orthogonal diagonalization. Its numerical complexity is equal to $IN(N-1)(4NM+17M+4N+75)/2$ flops if the M matrices $\boldsymbol{G}_m$ are symmetric where I stands for the number of executed sweeps.

Finally, regarding cumulant estimation, the computation of the $2q$-th order cumulant of a N-dimensional random process requires $(2q-1)K$ flops where K stands for the data length. Consequently, the number of flops required to compute the $2q$-th order cumulant array exploiting all its symmetries is then given by $(2q-1)Kf_{2q}(N)$ flops where $f_{2q}(N)$ denotes the number of its free entries and is given as a function of N, for $q=1,2,3$, by:

$$f_2(N)=\frac{N^2+N}{2}=\mathcal{O}\left[\frac{N^2}{2}\right],$$

$$f_4(N)=\frac{1}{8}N(N+1)(N^2+N+2)=\mathcal{O}\left[\frac{N^4}{8}\right],$$

$$f_6(N)=\frac{N^6}{72}+\frac{N^5}{12}+\frac{13N^4}{72}+\frac{N^3}{4}+\frac{22N^2}{72}+\frac{N}{6}\mathcal{O}\left[\frac{N^6}{72}\right].$$

Table 1 summarizes the numerical complexity of the elementary operations considered in this paper.

Based on the complexity of these elementary operations, the numerical complexity of each of the fifteen ICA methods we have selected is given in Table 2. Again, we insist that a whitening procedure has been applied in all methods.

Table 2
Numerical complexity of fifteen ICA algorithms

	Computational complexity
	N: number of EEG electrodes, P: number of sources, $it_i, i\in\{1,\cdots,12\}$: number of iterations in PICA, InfoMax, FastICA$_{\rm sym}$, FastICA$_{\rm def}$, ERICA, SIMBEC, 4-CANDHAP$_{\rm c}$, Q: required complexity to compute the roots of a real 4-th degree polynomial by Ferrari's technique in CoM$_2$, L_w, N_t, N_f, M_1 and M_2: smoothing window's length, number of time bins, number of frequency bins, number of matrices referred to the time-frequency point wherein sources are of significant energy and number of matrices among those M_1 ones with only one active source in the considered time-frequency point, respectively, in TFBSS, $\delta_{\omega_i}=1$ if $i\in\{2,\cdots,6\}$ and $\delta_{\omega_i}=0$ otherwise.
SOBI$_{\rm rob}$	$MKN^2/2+5M^2N^3-M^3N^3/3+2MN^2P+MP^2N+MP^2+(MP^2+4P^3/3)J_1+MP+MN^2+2N^3/3+NP+(3N-P)P^2/3+IP(P-1)(17M+75+4P+4PM)/2$
SOBI	$\min\{KN^2/2+4N^3/3+PNK,2KN^2\}+4N^3/3+(M-1)N^3/2+IP(P-1)(17(M-1)+75+4P+4P(M-1))/2$
TFBSS	$\min(KN^2/2+4N^3/3+PNK+,2KN^2)+2P\log_2P+P+(K+L_w+\log_2(L_w))N_tN_fP(P+1)/2+2M_1P^3/3+3T_2+IP(P-1)(4PM_2+17M_2+4P+75)/2$
PICA	$\min(KN^2/2+4N^3/3+PNK,2KN^2)+(P^3+(K+1)P^2+3PK)it_1$
InfoMax	$\min(KN^2/2+4N^3/3+PNK,2KN^2)+(P^2+P^3+4P+5KP)it_2$
FastICA$_{\rm def}$	$\min(KN^2/2+4N^3/3+PNK,2KN^2)+(2(P-1)(P+K)+5KP(P+1)/2)it_3$
FastICA$_{\rm sym}$	$\min(KN^2/2+4N^3/3+PNK,2KN^2)+2N^3/2+(16P^3/3+P^2+3KP^2)it_4$
CoM$_2$	$\min(KN^2/2+4N^3/3+PNK,2KN^2)+IP^2Q/2+\min(12If_4(P)P^2+2IP^3+3Kf_4(P)+KP^2,13IKP^2/2)$
JADE	$\min(KN^2/2+4N^3/3+PNK,2KN^2)+3Kf_4(P)+KP^2+\min(4P^6/3,8P^3(P^2+3))+IP(P-1)(75+21P+4P^2)/2$
ERICA	$\min(KN^2/2+4N^3/3+PNK+,2KN^2)+PNT+9PN^2+\frac{11}{3}N^3+N^2+N+it_7(PNT+5P^2T+4PT+3P^2+3P^3+P^2N)$
SIMBEC	$\min(KN^2/2+4N^3/3+PNK+,2KN^2)+N^2T+5P^2+9PN^2+\frac{11}{3}N^3+N^2+N+it_5(PNT+\delta_{\omega_2}(NPT+NP+P^2N+P^3)+\delta_{\omega_3}(2PT+NPT+NP+P^2N+P^3)+\delta_{\omega_4}(2PT+3NPT+2NP^2+P^3)+\delta_{\omega_5}(5PT+3NPT+NP^3+NP+2P^2N+P^3)+\delta_{\omega_6}(7PT+5NPT+4NP^2+P^2N+P^3)+12P^2+12P^2N+\frac{22}{3}P^3+NP)$
FOBIUM$_{\rm JAD}$	$\min(KN^2/2+4N^3/3+PNK+,2KN^2)+3MLf_4(N)+2N^6/3+P^2(3N^2-P)/3+(M-1)N^6/2+IN^2(N^2-1)\{4N^2(M-1)+17(M-1)+4N^2+75\}/2+2N^3P$
ICAR	$\min(KN^2/2+4N^3/3+PNK+,2KN^2)+K(3f_4(N)+2N^6/3+P^2(3N^2-P)/3+N^2P+(8NP^2+11N^3/3+N^2+N)N+N^2P^2(N-1)+IP(P-1)(75+9N(N-1)+8PN(N-1)+4P)+IN(N-1)(4N^2+21N+75)/2$
FOOBI$_1$	$\min(KN^2/2+4N^3/3+PNK+,2KN^2)+3Lf_4(N)+2N^6/3+P^2(3N^2-P)/3+N^2P+N^2P^2+2P(P+1)N^4+\min\{7M_3m_3^2+11m_3^3/3,3M_3m_3^2\}+IP(P-1)[4P^2+21P+75]/2+N^2P(P+1)+\min\{6N^3P,(2N^3/3+(3N-1)/3)P\}$
4-CANDHAP$_{\rm c}$	$\min(KN^2/2+4N^3/3+PNK+,2KN^2)+\frac{97}{72}N^6+N^2P^2+(3N^2P^2+\frac{8}{3}PN^3+10PN+\frac{35}{3}P^3-\frac{2}{3}P)it_{12}+P(IN(N-1)(8N+90))/2$

5. Performance analysis on simulated data

Two experiments are considered in this section to evaluate the fifteen ICA algorithms in the context of epileptic signals (interictal spikes) corrupted by muscle artifacts. The first one uses synthetic spike-like epileptic EEG signals generated by realistic biomathematical models in order to quantify the performance of the methods. In the second experiment, real data are processed in order to get qualitative results. In the first experiment, the behavior of ICA methods is studied as a function of the Signal to Noise Ratio (SNR), for a fixed data length of $K = 8192$ samples, which corresponds to 32 seconds. All reported results are obtained by averaging over 50 realizations the outputs of the performance criterion subsequently defined.

5.1. Data generation. The main purpose of this subsection is to explain how we obtain synthetic but realistic data for quantifying the performance of the methods. The simulated 32-channels EEG data (one observation is displayed in Fig. 1) are generated with a spatio-temporal model developed by our team [33–35]. In this model, EEG sources were represented as a dipole layer distributed over the cortical surface. The geometrical description of the cortical surface was achieved by using a mesh made of 19626 triangles (mean surface of 4.8 mm^2) obtained from the segmentation of the gray-white matter interface from a patient 3D T1-weighted MRI. Each triangle of the mesh was associated to an elementary current dipole. The dipole was placed at the barycenter of the triangle and oriented perpendicular to its surface. The moment of each dipole was weighted by a coefficient proportional to the area of the corresponding triangle. In addition, each dipole was assumed to correspond to a distinct cortical neuronal population. Its time course, which represents the time-varying dynamics of the associated population, was provided by the output of a neuronal population model [54], in which parameters can be adjusted to generate either background-like activity or interictal-spikes. In this model the source of these epileptic activities was manually delineated on the mesh as a set of contiguous triangles. Dipoles associated with triangles within the patch were assigned highly correlated interictal spike activities (i.e. transient interictal spikes) using an appropriate setting of coupling parameters between populations. All other dipoles of the cortical mesh were assigned a null activity. From this setup, we built a spatio-temporal source matrix $\boldsymbol{S}^{(e)}$ containing the time-varying activities of all cortical epileptic dipoles. The p-th line of this matrix contains the time-course of the p-th dipole within the patch. According to Sec. 2, matrix $\boldsymbol{S}^{(e)}$ also represents one realization of the vector random process $\{\boldsymbol{s}^{(e)}[k]\}$ (1).

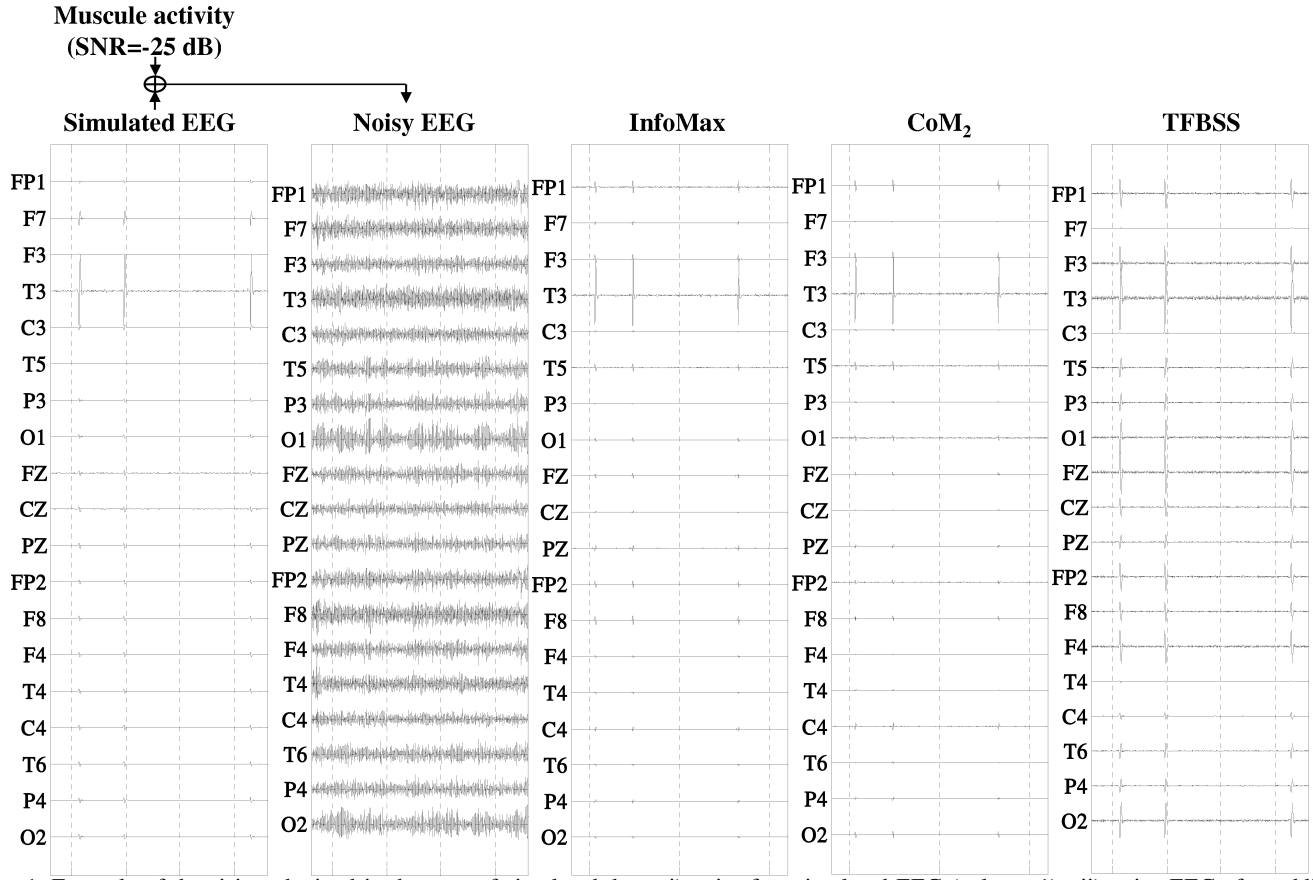

Fig. 1. Example of denoising obtained in the case of simulated data: i) noise free simulated EEG (column 1), ii) noisy EEG after adding real muscle activity with SNR = -25 dB (column 2), iii) EEG denoised by Infomax (column 3), iv) EEG denoised by CoM$_2$ (column 4), and v) EEG denoised by TFBSS (column 5)

Scalp EEG data were then generated using a realistic head model representing the brain, the skull and the scalp [55]. From this head model, the forward problem was then numerically solved for each triangle within the patch using a boundary element method (ASA, ANT, Enschede, Netherlands) to obtain the leadfield matrix $\boldsymbol{A}^{(e)}$ of equation (1). This mixing matrix gives the contribution of each dipole of the patch at the level of 32 scalp electrode positions (19-20 standard 10-20 electrodes plus additional electrodes at FC1, FC2, FC5, FC6, CP1, CP2, CP5, FT9, FT10, P9, P10 and POZ). The $(N \times K)$ matrix $\boldsymbol{X}^{(e)}$ of scalp epileptic data is thus given by $\boldsymbol{X}^{(e)} = \boldsymbol{A}^{(e)}\,\boldsymbol{S}^{(e)}$. In this paper we considered a single patch, made of 100 contiguous triangles (5 cm^2) located in the left superior temporal gyrus, where the activities of dipoles within the patch were highly correlated. In addition, for each experiment and each trial, EEG muscle activity was extracted from real 32-channel EEG data in order to generate the matrix $\boldsymbol{X}^{(b,m)} = \boldsymbol{A}^{(b)}\,\boldsymbol{S}^{(b)} + \boldsymbol{A}^{(m)}\,\boldsymbol{S}^{(m)} + \boldsymbol{N}$ of noisy scalp background and muscular activities, given in (1). More precisely, each trial of EEG muscle activity was normalized with respect to the channel showing the maximal power. Then, different levels of amplitude of noisy background and muscular activities were added to the simulated spike activities to get noisy simulated signals with different SNR values.

5.2. Performance criterion. The performance of the fifteen ICA methods has been evaluated by computing the following Normalized Mean-Squared Error (NMSE):

$$NMSE = \sum_{n=1}^{N} \left(\frac{\sum_{\ell=1}^{L} \sum_{k=1}^{K} \left(x_n^{(e)}[k] - \widehat{x}_n^{(e,\ell)}[k] \right)^2}{L \sum_{k=1}^{K} x_n^{(e)}[k]^2} \right), \quad (6)$$

where $\{x_n^{(e)}[k]\}$ is the n-th row of the $\boldsymbol{X}^{(e)}$ matrix defined in Subsec. 5.1, $\{\widehat{x}_n^{(e,\ell)}[k]\}$ is the reconstructed surface EEG after denoising from the ℓ-th run, L is the number of Monte Carlo runs, K is the data length and N is the number of electrodes. More particularly, the independent components extracted by each method from the ℓ-th run are classified in a descending order according to their respective autocorrelation values. As the autocorrelation of muscle artifacts is relatively low with respect to that of epileptic spikes, the independent components representing muscle artifacts are expected to be among the last components. In turn, components of interest are classified among the first components, which facilitates their visual selection. Then, the signal vector $\{\widehat{\boldsymbol{x}}^{(e,\ell)}[k]\}$ is reconstructed by keeping only the components accounting for the sources of interest (epileptic spikes).

5.3. Effect of SNR. The objective of this experiment is to i) evaluate the impact of SNR on the quality of source extraction and ii) to compare the numerical complexity of the fifteen algorithms. The data length, K, is fixed to 8192 samples, the SNR values are equal to -30, -25, -20, -15, -10 and -5 dB, and the number P of sources varies, in the range $P \in \{2, 3, 4, 5, 6, 7, 8, 12, 16, 20, 24, 28, 32\}$. For conciseness, we display in Fig. 1 an example of EEG signals denoised by only three methods, namely TFBSS, CoM2 and InfoMax. In the original un-noisy EEG (Fig. 2, left), the spike-like activity was clearly visible at electrode T3 (facing the patch), whereas it is entirely buried in noisy data (Fig. 2, column 2). The spike activity at electrode T3 was well reconstructed with TFBSS, InfoMax and CoM2. However, for InfoMax and CoM2, the diffusion of this activity on other channels was slightly different than in original data. This difference is more visible when the TFBSS method is considered.

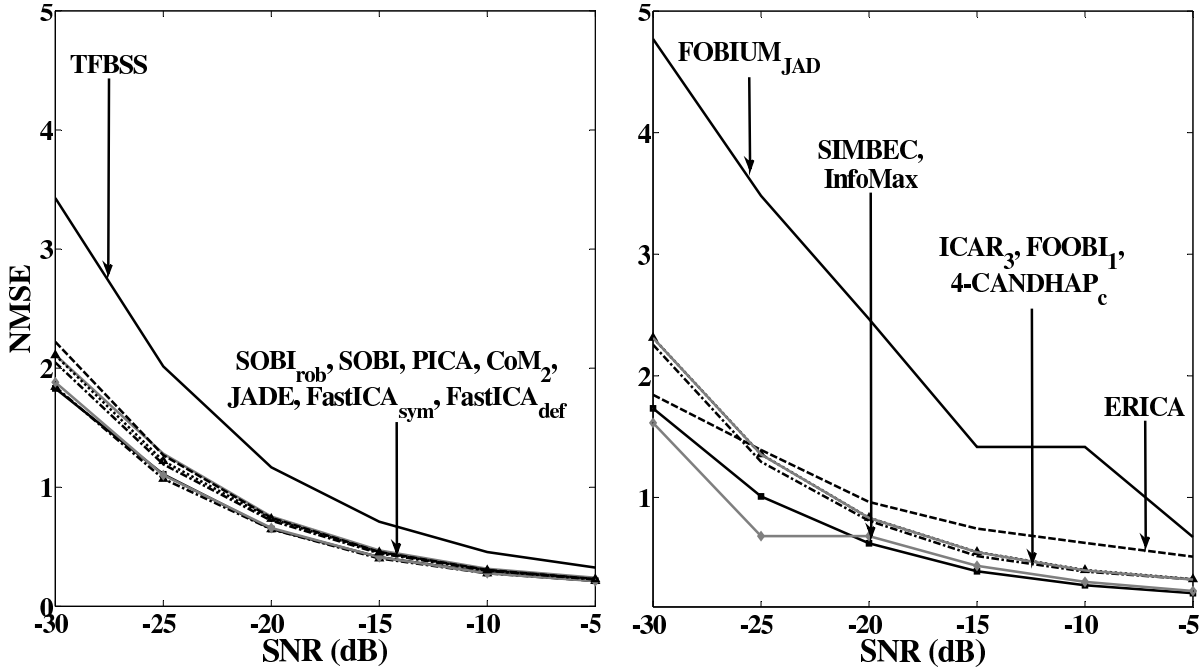

Fig. 2. NMSE as a function of SNR for $K = 8192$ data samples taking the number P of independent components such that each method

gives the best NMSE

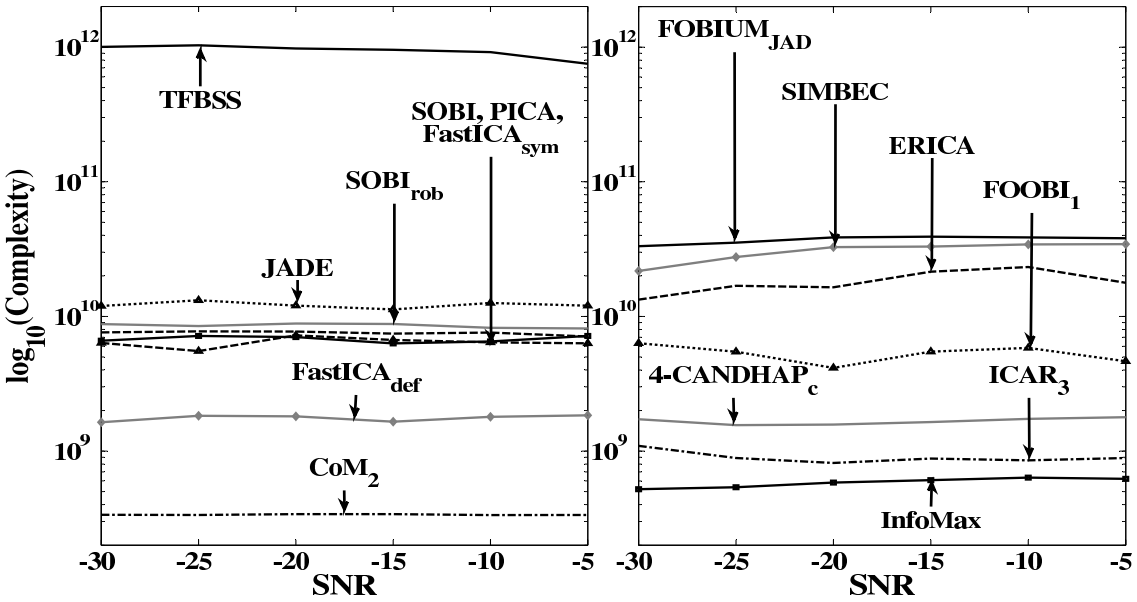

Fig. 3. Numerical complexity as a function of SNR for $K = 8192$ data samples taking the number P of independent components such that each method gives the best NMSE

Figures 2 and 3 show the variations of NMSE and the numerical complexity of the fifteen methods as a function of SNR, respectively. Note that, in the following, the NMSE and the numerical complexity are only illustrated by choosing the value of P yielding the best NMSE. In addition, the methods are classified into two main categories: i) methods with classical standardization, namely JADE, CoM_2, SOBI, $\mathrm{SOBI}_{\mathrm{rob}}$, PICA, $\mathrm{FastICA}_{\mathrm{sym}}$, $\mathrm{FastICA}_{\mathrm{def}}$ and TFBSS, and ii) methods using a standardization without any reduction of dimension, namely $\mathrm{FOBIUM}_{\mathrm{JAD}}$, FOOBI_1, ICAR_3, 4-$\mathrm{CANDHAP}_{\mathrm{c}}$, InfoMax, ERICA and SIMBEC.

From Fig. 2, we can observe that JADE, CoM_2, SOBI, $\mathrm{SOBI}_{\mathrm{rob}}$, PICA, $\mathrm{FastICA}_{\mathrm{sym}}$ and $\mathrm{FastICA}_{\mathrm{def}}$ have a quasi-similar behaviour, whatever the SNR value. FOOBI_1, ICAR_3 and 4-$\mathrm{CANDHAP}_{\mathrm{c}}$ are slightly less effective than the seven previous methods, especially in the case of high SNR values (-10 and -5 dB). Regarding the $\mathrm{FOBIUM}_{\mathrm{JAD}}$ and TFBSS algorithms they clearly show a poorer performance than that of the other algorithms. The SIMBEC method performs similarly to InfoMax for SNR values equal or higher than -20 dB and presents the best performance for an SNR lower than -20 dB. The ERICA method exhibits a performance similar to that of most of other algorithms for an SNR ranging from -30 dB to -25 dB, but becomes less efficient as the SNR of simulated data increases. Results obtained on methods of second category tend to demonstrate that using a standardization without any reduction of dimension as a preprocessing step forces the estimated mixing matrix to be well-conditionned.

The computational complexity (Fig. 3) is calculated by fixing the intrinsic parameters of each method according to those chosen to compute the NMSE criterion. In general, we can observe that, for each method, the numerical complexity is roughly stable, whatever the SNR values. More precisely, $\mathrm{FOBIUM}_{\mathrm{JAD}}$, TFBSS and SIMBEC methods require the largest number of calculations. These three methods are followed by PICA, ERICA, SOBI, $\mathrm{SOBI}_{\mathrm{rob}}$, JADE, $\mathrm{FastICA}_{\mathrm{sym}}$ and FOOBI_1. Regarding the remaining algorithms (CoM_2, $\mathrm{FastICA}_{\mathrm{def}}$, ICAR_3, 4-$\mathrm{CANDHAP}_{\mathrm{c}}$ and InfoMax), and more particularly CoM_2, ICAR_3, and InfoMax, they require a smaller amount of calculations. These results can partially be explained by the number of independent components P needed by each method to reach the best NMSE. Figure 4 indicates for each trial and for three SNR values (-30, -15 and -5 dB) the number P required by each method to obtain the best performance. We observe that all methods of the first category (JADE, CoM_2, SOBI, $\mathrm{SOBI}_{\mathrm{rob}}$, PICA, $\mathrm{FastICA}_{\mathrm{sym}}$, $\mathrm{FastICA}_{\mathrm{def}}$ and TFBSS), ERICA, SIMBEC and InfoMax generally require the extraction of $P = 32$ independent components to obtain the best performance, whereas most of methods of second category, namely $\mathrm{FOBIUM}_{\mathrm{JAD}}$, FOOBI_1, ICAR_3 and 4-$\mathrm{CANDHAP}_{\mathrm{c}}$ need a smaller number of independent components to reach an equivalent performance.

The NMSE and the numerical complexity calculations of the fifteen methods indicate, in the simulated context of epileptic signals (interictal spikes) corrupted by muscle artifacts, that: i) InfoMax generally presents the best performance in the sense of NMSE criterion, ii) CoM_2 offers the best NMSE versus numerical complexity compromise, and iii) $\mathrm{FOBIUM}_{\mathrm{JAD}}$ and TFBSS provide the worse results in terms of performance and computational complexity.

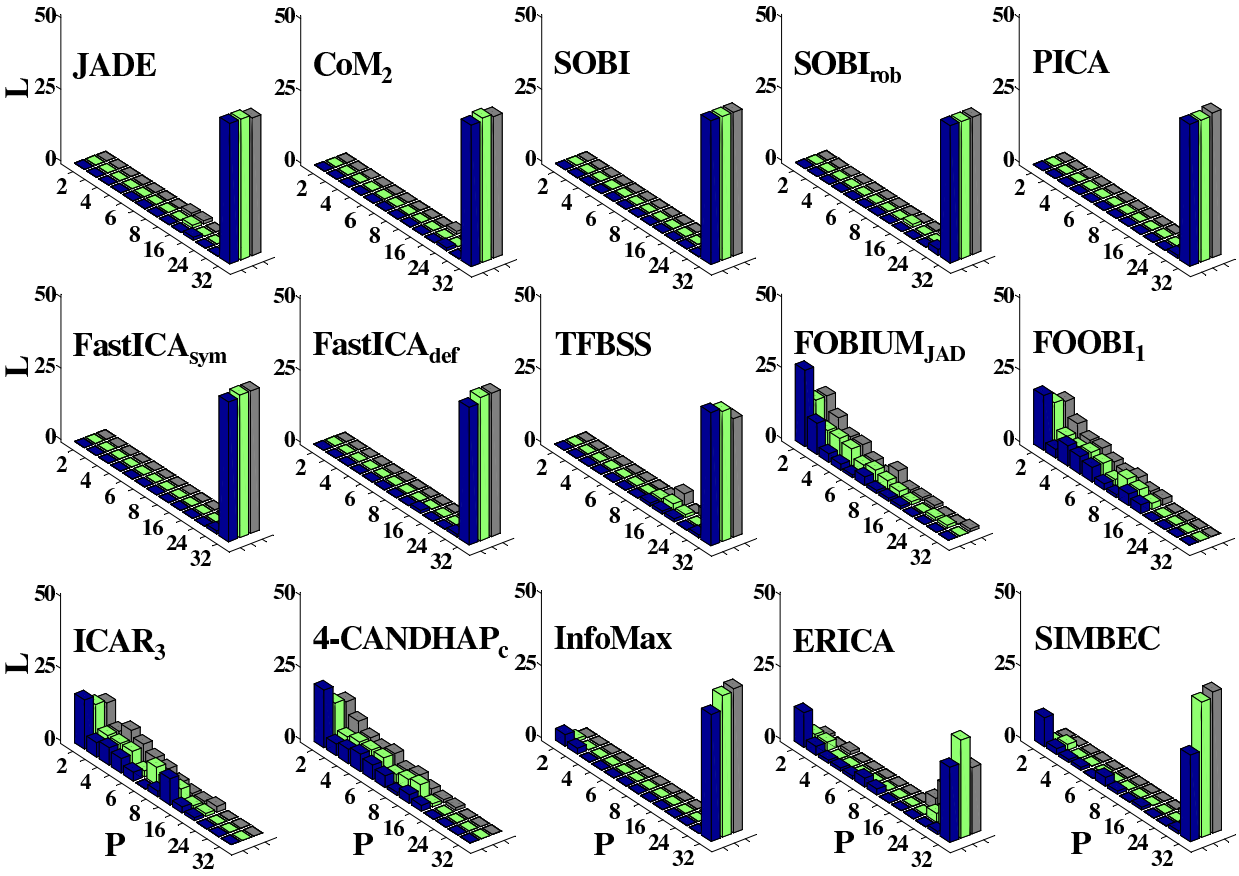

Fig. 4. Histogram of the number P of independent components required by each method to obtain the best NMSE: i) SNR equal to -30 dB (blue bar), ii) SNR equal to -15 dB (green bar), and iii) SNR equal to -5 dB (grey bar)

6. Application to real data

In this section we propose to test the feasibility of ICA algorithms on real data. For conciseness, only results given by TFBSS, CoM2 and InfoMax are shown. It is worth noting that these three methods were marked out by their results on simulated EEG data in terms of NMSE and numerical complexity in the previous section. The three methods were applied to the denoising of interictal spikes in a patient suffering from drug-resistant partial epilepsy. As part of his presurgical evaluation, this patient underwent two sessions of video-EEG monitoring, brain Magnetic Resonance Imaging (MRI), as well as interictal and ictal Single-Photon Emission Computed Tomography (SPECT) acquisition. During video-EEG monitoring, scalp-EEG data were acquired from 32 electrodes (19-20 standard 10-20 electrodes plus additional electrodes at FC1, FC2, FC5, FC6, CP1, CP2, CP5, FT9, FT10, P9, P10 and POZ) at a sampling frequency of 256 Hz.

These data were reviewed in order to isolate three epochs: i) two epochs containing a clean spike (figure 5, first and second column), and ii) one epoch including spikes hidden in muscle activity with very high level of noise (Fig. 5, third column). The same procedure as for simulated data was applied to reconstruct the denoised EEG signals. In addition, to evaluate the qualitative performance of the three methods, a source localization was performed on the two original cleaned signals (considered as a reference), on the noisy data, as well as on the latter data denoised by TFBSS, CoM_2 and InfoMax, respectively. The recent 4-ExSo-MUSIC algorithm [56] was used to achieve the source localization. Figure 5 illustrates that interictal spikes were visible at electrodes F8, T4, FC5, and FT10 of the two epochs of clean data (columns 1 and 2), whereas they were hidden in the noisy data (column 3). Clearly, the three ICA-methods enhance the interictal spikes at F8, T4, FC5, and FT10 electrodes and do not increase the diffusion of spikes on the remaining electrodes. We also calculated the numerical complexity of TFBSS, CoM_2 and showed (in agreement to the simulated results) that CoM_2 required the smallest amount of calculations (about 8.10^7 flops), InfoMax used about 4.10^9 flops and TFBSS needed a larger amount of calculations (about 2.10^{12} flops).

Regarding the source localization results (bottom of each column of Fig. 5), the spikes were localized in the right anterior temporal region for the first epoch of clean data (column 1) and both in the right temporal neocortex and in the right insula for the second epoch of clean data (column 2). Even if these localizations were slightly different, they were in gen-

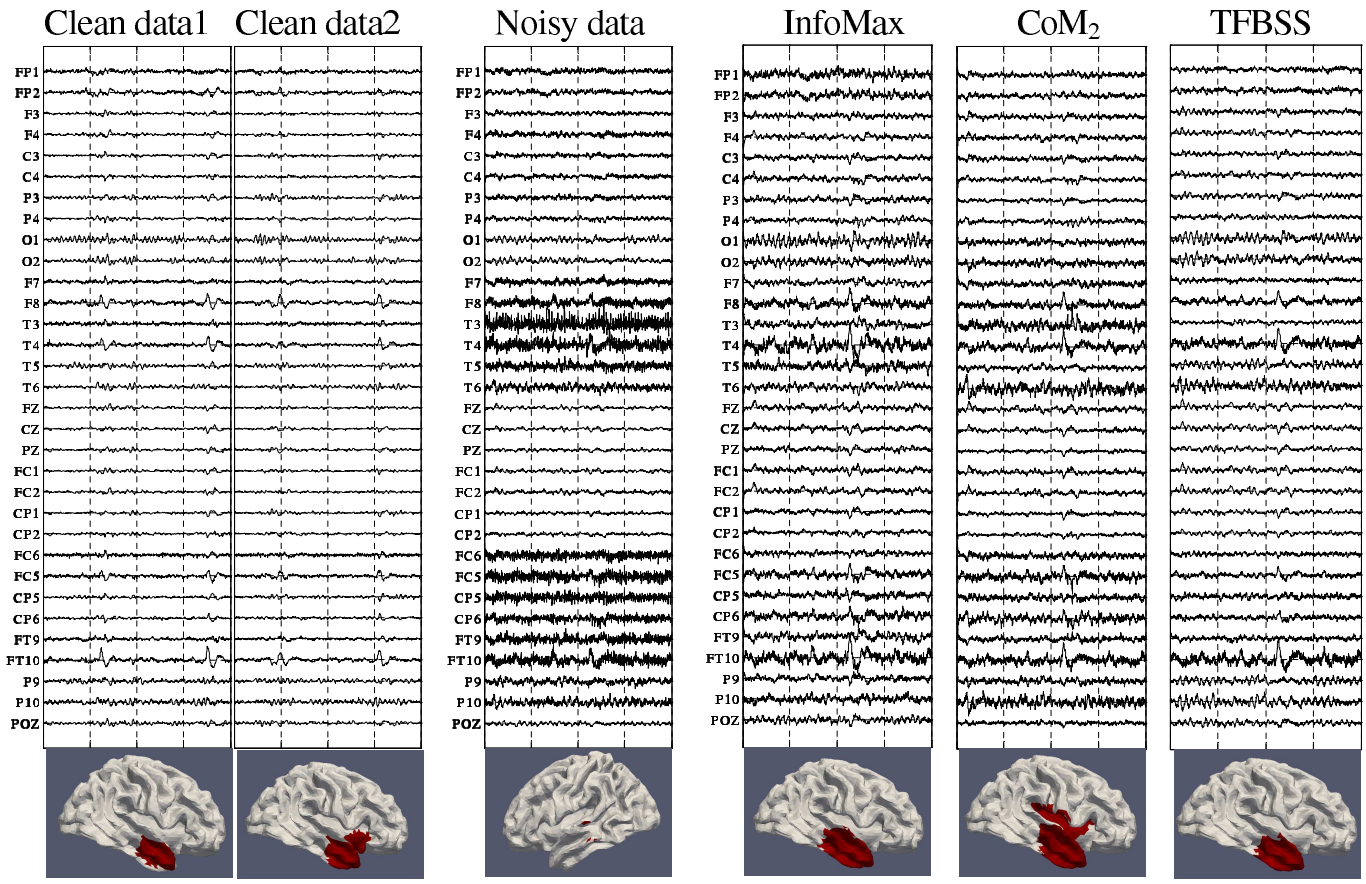

Fig. 5. Denoising of real interictal spikes data: i) two noise-free interictal spikes (columns 1 and 2), ii) epoch including spikes hidden in muscle activity with very high level of noise (column 2), iii) EEG denoised by Infomax, CoM_2 and TFBSS (columns 3, 4 and 5, respectively). The source localization results at the output of 4-ExSo-MUSIC are depicted at the bottom of each column

eral consistent with the visual interpretation of T1-weighted MRI data and also corroborated by interictal SPECT data. For the noisy epoch (column 3), the spike source was incorrectly localized in the left temporal region. Spike data denoised by CoM_2 were localized both in the right temporal neocortex and in the right insula in agreement with the source localization obtained from the second epoch of clean data. The localization results at the output of InfoMax and TFBSS were quasi-similar with those obtained from the second epoch of clean data.

The results obtained on real interictal epileptic spikes suggest that choosing the appropriate ICA method for processing actual data in the context of interictal epileptic spikes is not an easy task. Indeed, it is not obvious to know the true epileptic area with a perfect accuracy, since two clean epochs recorded in the same patient can lead to slightly different source locations. Consequently, it is clearly not possible to say which ICA method denoises better the epileptic spikes on real data, since the source localization after each ICA-based denoising is consistent with that obtained from one of both epochs of clean data. In terms of performance, we can just say that each of our tested ICA methods is doing its work properly, i.e. it removes successfully the muscle artifacts without altering the interictal epileptic spikes, and it significantly improves the quality of the source localization. As far as the numerical complexity is considered, CoM_2 would be the most appropriate choice.

7. Conclusions

Advanced epilepsy research and diagnosis require precise information, which can be extracted from non-invasive EEG data. However, EEG signals may be unfortunately contaminated by instrumental noise and various electrophysiological artifacts, such as power line noise, broken wire contacts, ocular movements and muscular activity. These types of noise and artifacts hide physiological activities of interest. Among all these artifacts, the muscular activity is particularly difficult to remove. Previous investigations in the biomedical engineering context showed that ICA is an efficient approach for the blind extraction of components of interest from a noisy mixture of sources. Nevertheless, the application of ICA to the extraction of epileptic signals in the presence of muscular activities is still challenging; it is indeed difficult to access a ground truth for epileptic sources in order to evaluate the accuracy of ICA. In addition, most of the studies that have used ICA to analyze and to process epileptic signals have only explored a limited number of ICA algorithms, namely InfoMax, FastICA and SOBI. These issues are addressed in

this paper through the comparison of fifteen ICA algorithms, both in terms of performance and numerical complexity. The comparative analysis is first performed on simulated EEG data, reproducing realistic epileptic EEG signals contaminated by muscle artifacts, in order to quantify the accuracy of the ICA methods. CoM_2 then appears as the ICA method offering the best compromise between performance and numerical complexity, while TFBSS and $FOBIUM_{JAD}$ offer the worse. The good behavior of CoM_2 is next confirmed on one set of real data. Forthcoming work will aim first at comparing even more ICA methods, for instance by including improved versions of the techniques analyzed in [57, 58]. Second, we will acquire dense EEG data (> 128 channels) in order to analyze the performance of ICA methods as a function of the number of electrodes.

Acknowledgements. This work has been partly supported by the French ANR contract 10- BLAN-MULTIMODEL.

REFERENCES

[1] B.W. Mcmenamin, A.J. Shackman, J.S. Maxwell, D.R. Bachhuber, A.M. Koppenhaver, L.L. Greischar, and R.J. Davidson, "Validation of ICA-based myogenic artifact correction for scalp and source-localized EEG", *NeuroImage* 49 (3), 2416–2432 (2010).

[2] T.-P. Jung, C. Humphries, T.W. Lee, S. Makeig, M.J. Mckeown, V. Iragui, and T.J. Sejnowski, "Extended ica removes artifacts from electroencephalographic recordings", *Advances in Neural Information Processing Systems* 10, 894–900 (1998).

[3] T.P. Jung, S. Makeig, M. Westerfield, J. Townsend, E. Courchesne, and T.J. Sejnowski, "Independent component analysis of single-trial even-related potentials", *Second Int. Symposium on Independent Component Analysis and Blind Signal Separation* 1, 173–178 (1999).

[4] S. Makeig, A.J. Bell, T.-P. Jung, and T.J. Sejnowski, "Independent component analysis of electroencephalographic data", *Advances in Neural Information Processing Systems* 8, 145–151 (1996).

[5] R. Vigario and E. Oja, "BSS and ICA in neuroinformatics: from current practices to open challenges", *IEEE Reviews in Biomedical Engineering* 1, 50–61 (2008).

[6] R. Vigario, J. Sarela, V. Jousmaki, M. Hamalainen, and E. Oja, "Independent component approach to the analysis of EEG and MEG", *IEEE Trans. on Biomedical Engineering* 47 (5), 589–593 (2000).

[7] L. Albera, P. Comon, L. Parra, A. Karfoul, A. Kachenoura, And L. Senhadji, "Biomedical applications", in *Handbook of Blind Source Separation*, eds. P. Comon and C. Jutten, Academic Press, London, 2010.

[8] Y. Deville, C. Jutten, and R. Vigario, "Overview of source separation applications", in *Handbook of Blind Source Separation*, eds. P. Comon and C. Jutten, Academic Press, London, 2010.

[9] S. Olbrich, J. Jodicke, C. Sander, H. Himmerich, and U. Hegerl, "ICA-based muscle artefact correction of EEG data: What is muscle and what is brain?: Comment on McMenamin et al.", *NeuroImage* 54 (1), 1–3 (2011).

[10] S. Vorobyov and A. Cichocki, "Blind noise reduction for multisensory signals using ICA and subspace filtering, with application to eeg analysis", *Biological Cybernetics* 86 (4), 293–303 (2002).

[11] A. Kachenoura, L. Albera, and L. Senhadji, "Séparation aveugle de sources en ingénierie biomédicale", *IRBM, Elsevier* 28 (1), 20–34 (2007).

[12] A. Kachenoura, L. Albera, L. Senhadji, and P. Comon, "ICA: a potential tool for BCI systems", *IEEE Signal Processing Magazine, Special Issue on Brain-Computer Interfaces* 25 (1), 57–68 (2008).

[13] F. Poree, A. Kachenoura, H. Gauvrit, C. Morvan, G. Carrault, and L. Senhadji, "Blind source separation for ambulatory sleep recording", *Trans. on Information Technology in Biomedicine* 10 (2), 293–301 (2006).

[14] A. Belouchrani, K. Abed-Meraim, J.F. Cardoso, and E. Moulines, "A blind source separation technique using second-order statistics", *IEEE Trans. on Signal Processing* 45 (2), 434–444 (1997).

[15] A. Ziehe and K.R. Muller, "TDSEP – an efficient algorithm for blind separation using time structure", *ICANN'98, Proc. 8th Int. Conf. on Artificial Neural Networks* 1, 675–680 (1998).

[16] T.W. Lee, M. Girolami, and T.J. Sejnowski, "Independent component analysis using an extended infomax algorithm for mixed sub-gaussian and super-gaussian sources", *Neural Computation* 11 (2), 417–441 (1999).

[17] S. Makeig, "EEGLAB: ICA toolbox for psychophysiological research", *WWW Site, Swartz Center for Computational Neuroscience, Institute of Neural Computation, University of San Diego California*, www.sccn.ucsd.edu/eeglab/ (2000).

[18] P. Comon and C. Jutten, *Handbook of Blind Source Separation*, Academic Press, New York, 2010.

[19] J. Karvanen and V. Koivunen, "Blind separation methods based on pearson system and its extensions", *Signal Processing, Elsevier* 82, 663–673 (2002).

[20] A. Belouchrani and A. Cichocji, "Robust whitening procedure in blind source separation context", *Electronics Letters* 23 (24), 2050–2051 (2000).

[21] C. Fevotte and C. Doncarli, "Two contributions to blind sources separation using time-frequency distributions", *IEEE Signal processing Letters* 11 (3), 386–389 (2004).

[22] J.F. Cardoso and A. Souloumiac, "Blind beamforming for non-gaussian signals", *IEE Proceesings-F* 140 (6), 362–370 (1993).

[23] P. Comon "Independent component analysis, a new concept?", *Signal Processing, Elsevier* 36 (3), 287–314 (1994).

[24] S. Cruces, L. Castedo, and A. Cichocki, "Novel blind source separation algorithms using cumulants", *Proc. on Int. Conf. on Acoustic, Speech and Signal Processing (ICASSP'2000)* 1, 3152–3155 (2000).

[25] S.A. Cruces-Alverez, A. Cichocki, and S. Amari, "On a new blind signal extraction algorithm: different criteria and stability analysis", *IEEE Signal Processing Letters* 9 (8), 233–236 (2002).

[26] A. Ferreol, L. Albera, and P. Chevalier, "Fourth order blind identification of underdetermined mixtures of sources (FOBIUM)", *ICASSP 03, 2003 IEEE Int. Conf. on Acoustics Speech and Signal Processing* 1, 41–44 (2003).

[27] A. Ferreol, L. Albera, and P. Chevalier, "Fourth order blind identification of underdetermined mixtures of sources (FOBIUM)", *IEEE Trans. on Signal Processing* 53, 1254–1271 (2005).

[28] L. Albera, A. Ferreol, P. Chevalier, and P. Comon, "ICAR: Independent Component Analysis using Redundancies", *ISCAS*

04, 2004 IEEE Int. Symposium on Circuits and Systems 1, CD-ROM (2004).

[29] L. Albera, A. Ferreol, P. Chevalier, and P. Comon, "ICAR, a tool for blind source separation using fourth order statistics only", *IEEE Trans. on Signal Processing* 53, 3633–3643 (2005).

[30] L.D. Lathauwer, J. Castaing, and J.F. Cardoso, "Fourth-order cumulant-based blind identification of underdetermined mixtures", *IEEE Trans. on Signal Processing* 55 (6), 2965–2973 (2007).

[31] A. Karfoul, L. Albera, and L. De Lathauwer, "Canonical decomposition of even higher order cumulant arrays for blind underdetermined mixture identification", *SAM 08, Fifth IEEE Workshop on Sensor Array and Multi-Channel Signal Processing* 1, 501–505 (2008).

[32] A. Karfoul, L. Albera, and L. De Lathauwer, "Iterative methods for the canonical decomposition of multi-way arrays: Application to blind underdetermined mixture identification", *Signal Processing, Elsevier* 91 (8), 1789–1802 (2011).

[33] D. Cosandier-Rimele, J.M. Badier, P. Chauvel, and F. Wendling, "A physiologically plausible spatio-temporal model for depth-EEG signals recorded with intracerebral electrodes in human partial epilepsy", *IEEE Trans. on Biomedical Engineering* 3 (54), 380–388 (2007).

[34] D. Cosandier-Rimele, I. Merlet, J.M. Badier, P. Chauvel, and F. Wendling, "The neuronal sources of EEG: modeling of simultaneous scalp and intracerebral recordings in epilepsy", *NeuroImage* 42 (1), 135–146 (2008).

[35] D. Cosandier-Rimele, I. Merlet, F. Bartolomei, J.M. Badier, and F. Wendling, "Computational modeling of epileptic activity: from cortical sources to eeg signals", *J. Clinical Neurophysiology* 27 (6), 465–470 (2010).

[36] J. Sarvas, "Basic mathematical and electromagnetic concepts of the biomagnetic inverse problems", *Physics in Medicine and Biology* 32, 11–22 (1987).

[37] T.Y. Young and T.W. Calvert, *Classification, Estimation and Pattern Recognition*, American Elsevier Publishing Company, New York, 1974.

[38] P. Mccullagh, *Tensor Methods in Statistics*, Chapman and Hall, London, 1987.

[39] V.P. Leonov and A.M. Shiryaev, "On a method of calculation of semi-invariants", *Theory of Probability and its Applications* 4, 319–29 (1959).

[40] S. Amari, "Natural gradient works efficienttly in learning", *Neural Computation* 10 (2), 251–276 (1998).

[41] P. Comon, "Separation de melanges de signaux", *GRETSI 89, DouziŕMe colloque sur le Traitement du Signal et des Images* 1, 137–140 (1989).

[42] E. Moreau, "Criteria for complex sources separation", in *EUSIPCO 96, XIV Eur. Signal Proc. Conf.* 1, 931–934 (1996).

[43] J.F. Cardoso, "Blind signal separation: statistical principles", *Proc. IEEE* 9 (10), 2009–2025 (1998).

[44] A. Hyvarinen, "Fast and robust fixed-point algorithms for independent component analysis", *IEEE Trans. on Neural Networks* 10 (3), 626–634 (1999).

[45] A. Hyvarinen, "Jacobi angles for simultaneous diagonalization", *SIAM J. Matrix Analysis and Applications* 17 (1), 161–164 (1996).

[46] X. Luciani and L. Albera, "Joint eigenvalue decomposition using polar matrix factorization", in *Latent Variable Analysis and Signal Separation LVA-ICA 2010*, vol. 6365, pp. 612–619, Springer, Saint Malo, 2010.

[47] P. Comon, X. Luciani, and A.L.F.D. Almeida, "Tensor decompositions, alternating least squares and other thales", *J. Chemometrics* 23, CD-ROM (2009).

[48] G.H. Golub and C.F.V. Loan, *Matrix Computations*, second edition, The Johns Hopkins University Press, Baltimore, 1989.

[49] J.J. Rieta, F. Castells, C. Sanchez, V. Zarzoso, and J. Millet, "Atrial activity extraction for atrial fibrillation analysis using blind source separation", *IEEE Trans. on Biomedical Engineering* 51 (7), 1176–1186 (2004).

[50] V. Zarzoso and A. Hyvarinen, "Iterative algorithms", in *Handbook of Blind Source Separation*, eds. P. Comon and C. Jutten, pp. 179–225, Academic Press, London, 2010..

[51] G.H. Golub and C. Reinsch, "Singular value decomposition and least squares solutions", *Handbook for Automatic Computation II, Linear Algebra*, ed. J.H. Wilkinson, Springer, New York, 1970.

[52] T.F. Chan, "An improved algorithm for computing the singular value decomposition", *ACM Transaction on Mathematical Software* 8 (1), 72–83 (1982).

[53] L.D. Lathauwer and J. Castaing, "Blind identification of underdetermined mixtures by simultaneous matrix diagonalization", *IEEE Trans. on Signal Processing* 56, 3 (2008).

[54] F. Wendling, J. Bellanger, F. Bartholomei, and P. Chauvel, "Relevance of nonlinear lumped-parameter models in the analysis of depth-eeg epileptic signals", *Biol. Cybern.* 83, 367–378 (2000).

[55] S.I. Goncalves, J.C.D. Munck, J.P.A. Verbunt, F. Bijma, R.M. Heethaar, and F.L.D. Silva, "In vivo measurement of the brain and skull resistivities using an EIT-based method and realistic models for the head", *IEEE Trans. on Biomedical Engineering* 50 (6), 754–767 (2003).

[56] G. Birot, L. Albera, F. Wendling, and I. Merlet, "Localisation of extended brain sources from eeg/meg: the exso-music approach", *Elsevier Neuroimage* 56 (1), 102–113 (2011).

[57] Z. Koldosky, P. Tichavsky, and E. Oja, "Efficient variant of algorithm FastICA for independent component analysis attaining the Cramér-Rao lower bound", *IEEE Trans. Neural Netw.* 17 (5), 1265–1277 (2006).

[58] A. Yeredor, "Blind separation of Gaussian sources via second-order statistics with asymptotically optimal weighting", *IEEE Signal Processing Letters* 7, 197–200 (2000).